國立交通大學

光電工程研究所

博 士 論 文

新型高對比、高亮度、無轉態之 Pi-cell 液晶顯示元件

Novel High Contrast, High Brightness and Transition-Free

Pi-cell Liquid Crystal Display Device

研 究 生：陳司芬

指導教授：謝漢萍教授

中 華 民 國 九十九 年 一 月

新型高對比、高亮度、無轉態之 Pi-cell 液晶顯示元件

Novel High Contrast, High Brightness and Transition-Free Pi-cell Liquid Crystal Display Device

研 究 生： 陳司芬　　　　　Student：Szu-Fen F. Chen

指導教授： 謝漢萍 博士　　　Advisor：Dr. Han-Ping D. Shieh

國 立 交 通 大 學

光 電 工 程 研 究 所

博 士 論 文

中華民國 九十九 年 一 月

新型高對比、高亮度、無轉態之 Pi-cell 液晶顯示元件

博士研究生：陳司芬　　　指導教授：謝漢萍 教授

國立交通大學　　　光電工程研究所

摘　　要

　　薄膜電晶体液晶顯示器(TFT-LCD)技術已取代傳統 CRT 電視應用的主流。為了使 TFT-LCD 顯示技術能夠穩佔龐大的 TV 應用市場商機，TFT-LCD 開發、製造…等相關業者無不致力於持續改善 TFT-LCD 的影像品質。由於 TFT-LCD 先天上驅動原理的限制，因此 TFT-LCD 動畫顯示模糊效應(Motion blur effect)的問題一再地被廣泛討論並尋求解決的方法。在目前所有被應用的 LCD 技術中，光學補償彎曲模態(Optically Compensated Bend, OCB；另稱為 Pi-cell)是目前反應速度最快的向列型液晶模態，由於液晶盒(LC-cell)特殊的結構設計使它不僅具有快速響應，同時也是具備廣視角顯示品質的液晶模態，因此在解決 TFT-LCD TV 動畫模糊效應上也是最強而有力的顯示模態。

　　由於 Pi-cell 快速響應的優點，使得高解析度色序法驅動的液晶顯示技術(Field Sequential Color Liquid Crystal Display)得以有實現的可能性。然而，Pi-cell 有不同液晶形變態之間的轉換與回復(State transition and Recovery)問題，造成在實際應用上的困難，甚至有在顯示品質最佳化上的可能性存在。本論文中，針對此問題提出了二種新的解決方式：

一、以奈米結構將液晶配向層之表面進行改質，以便形成"成核點"(nucleus)，使

得 Pi-cell 在由分散(Splay)模態轉換成彎曲(Bend)模態前必經的成核現象
(Nucleation)及完成轉態所需時間由現在的 2 分鐘(cell gap~5μm,0→6V驅動)
縮減至少於 1 秒。使得 Pi-cell 即便是需要經過轉態過程，亦能在幾乎無法
察覺的時間內均勻地轉態完畢，且無需於瞬間外加約 18 V 高脈衝電壓。

二、在前一項研究中，並不能消除 Pi-cell 的轉態特性，在顯示器的電壓操作區
間仍必須維持一個約 2V 的臨界電壓以保持彎曲(Bend)模態的穩定存在。基
於液晶光學特性具有不同入射光波長的分散特性 (dispersion)，紅 (R)、綠
(G)、藍(B) 三波長的電壓-透過率特性曲線(V-T curve)並不一致，因此 RGB
的臨界電壓並不相同 ($V_R < V_G < V_B$)。為確保顯示器運作能維持在彎曲模態，
必須將臨界電壓維持在 V_B，使得 Pi-cell 的透過率和對比相當程度被犧牲。
因此，我們另外提出新穎的反應型單体(reactive monomer)應用及 cell 結構設
計，使得 Pi-cell 中的液晶分子穩定在彎曲模態──驅動模態下，如此一來便
克服了 Pi-cell 的轉態問題；同時，由於新結構的 cell 邊界殘留位相差值較小，
亦使得新型 RMM-Pi-cell 在不加補償膜的情況下，其靜態對比度從傳統
Pi-cell 的 26 提昇到 288 (實驗室測試樣品), 提昇度達 11 倍。

本論文在顯示應用技術領域上的貢獻在於提出以奈米結構對 Pi-cell 的液晶
配向層進行改質，以改善其轉態時間及利用反應型單體層來消除現有 Pi-cell 本
質的轉態特性，使得其所造成之光學品質缺點得以被解決或改善。而其實現方式
僅需在現有的 TFT-LCD 的 Cell 製程架構中，增加 1~2 道簡單的製程，即可以完
全相容於現有的製造方式，倘若將現有的顯示器技術結合本論文研究成果將可以
創造出一種具有高影像品質的新型 Pi-cell 液晶顯示元件，使得此液晶模態的優
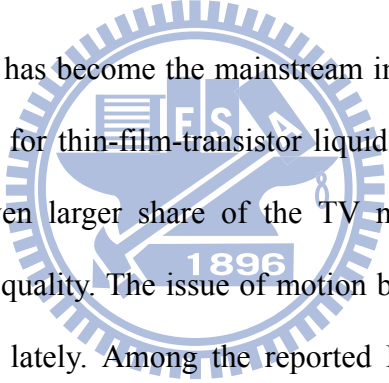勢不只有應用在一般 TFT-LCD，更能實現色序法驅動的液晶顯示技術。

Novel High Contrast, High Brightness and Transition-Free Pi-cell Liquid Crystal Display Device

Doctoral Student: Szu-Fen F. Chen   **Advisor: Dr. Han-Ping D. Shieh**

Institute of Electro-Optical Engineering
National Chiao Tung University

Abstract

TFT-LCD Technology has become the mainstream in replacing CRTs in TV and other applications. In order for thin-film-transistor liquid-crystal display (TFT-LCD) technology to claim an even larger share of the TV market, manufacturers must continue to improve image quality. The issue of motion blur effect in TFT-LCD TVs has been widely discussed lately. Among the reported LC modes the Pi-cell, also known as Optically Compensated Bend (OCB) mode, has been found to be a strong candidate to reduce the motion blur effect. Due to the LC-cell structure and the driving scheme, Pi-cell is not only a wide viewing angle display technology, but also the fastest-response LCD mode among the commercialized LCD modes.

Because of the fast response of the Pi-cell, the field sequential color LCD (FSC-LCD) which displays R, G and B colors in sequence in a pixel is promising for the high-resolution display. However, Pi-cell possesses intrinsic transition and recovery issues which lead to compromised optical properties, thus, limited in its applications. In this dissertation, we proposed two modified Pi-cells to resolve these issues.

1. Proposed *Nanostructure Enhanced Pi-cell* (*NE-Pi-cell*) modified the surface of alignment layer (PI) to create nuclei for speeding up the transition rate. The transition time of a *NE-Pi-cell* was reduced from 2 minutes to less than 1 sec compared with the conventional one. Moreover, the transition process was uniformly completed without applying high voltage pulse (~18V).

2. Even if the previous topic could speed up the transition rate to almost zero, the critical voltage also needed to be kept over 2V for maintaining the bend state of a Pi-cell. Based on the light dispersion property of liquid crystals, the critical voltage of R, G and B were different; i.e. $V_R < V_G < V_B$. In order to confirm that the Pi-cell could operate in bend state, a critical voltage larger than V_B needed to be chosen, which led to compromised optical qualities. Therefore, we suggested *reactive monomer modified Pi-cell* (*RMM-Pi-cell*) to eliminate the splay-to bend state transition. Besides, because of smaller residual retardation at the dark state, the static contrast ratio of a RMM-Pi-cell, compared with conventional Pi-cell, was improved from 26 to 288 (the test samples fabricated in laboratory), up to a factor of 11 without using compensation films.

We have demonstrated a novel alignment layer modified method of a Pi-cell for uniform and fast transition without high voltage pulses. Moreover, a transition-free and high optical performance Pi-cell has also proposed in this dissertation. The proposed novel Pi-cells only need one or two simple extra processes in conventional manufacturing of TFT-LCD. Combining the research results with current high image quality LCD technology, the novel high image quality Pi-cell will be realized. The results can not only improve the image qualities for general TFT-LCD applications, but also realize the FSC-LCDs.

Acknowledgement

經過漫長的五年半，終於在這歲末年初之際完成了博士學位，對我來說至今仍舊覺得像一場夢！當初決定回學校念博士僅僅是由於一個輕風拂面的午後，溫暖的陽光灑在我身上，走在校園中的輕鬆感使我暫時忘卻了工作的壓力與繁忙。然而，我沒想到的是「一個轉換心情的決定」卻讓我在人生與事業的低潮期有了一個新的目標和重心。回想碩士畢業時那一份急於離開校門，想要快點長大的心情，相對於在40歲後得到博士學位而言，這次畢業不捨的感覺份外難以形容。

求學期間數度想放棄的我，因著種種因緣際會及許多人的協助與鼓勵走完了這段看似永遠走不完的歷程。在這五年半中我首先要感謝我的指導教授—謝漢萍院長，老師細心的指導與嚴格的要求，令我這個已經在職場許久的學生特別的感動，畢竟在職場上不會有人再以這樣的真心來指導與糾正我的錯誤並教導我正確做學問的態度！其次，我特別要感謝的是陳皇銘老師，雖然名義上他不是我的指導教授，實際上在我心中他實實在在是我的指導教授，協助我完成論文當中的研究課題，指導我論文寫作…等。

身為在職生的我，由於要身兼繁重的工作，特別感謝實驗室的學弟妹們，感謝同為博士生的安琪、均合、柏儒、裕國和芳正為我扮演學校與我之間的橋樑，幫我解決了不少身為在職生不能常常到校的難題。同時，我還要感謝陳皇銘老師實驗室的學弟妹們，尤其是蓮馨、毓筠和淇文，謝謝他們對我研究課題的協助，我能順利拿到博士學位全賴大家平時的照顧和幫忙！還有遠在美國的鄭惟中老師，也願老師在美國一切都能順心！

最後，我想要將這份榮耀獻給我的老公、爸爸、媽媽、弟弟和妹妹們，在這段時間內沒有他們的包容和支持我絕對走不下去。在此要特別感謝親愛的老公Daniel 忍受我的壞脾氣，包容我不做家事，給予我實質上與精神上的雙重支持，讓我這個身兼數職的歐巴桑能夠完成這個不可能的任務！要感謝的人實在太多了，想要講得話怎麼樣也講不完，但是，最後我想要感謝自己、嘉許自己，多虧自己的那份堅持，終於給了自己再開啟人生另一個可能性的機會！

Table of Contents

Figure Captions

Table List

Chapter 1

Introduction

TFT-LCD Technology has become the mainstream in replacing CRTs in all size displays and creates various hand-held display applications, as shown in Fig.1-1[1]. In order for thin-film-transistor liquid-crystal display (TFT-LCD) technology to claim an even larger share of the large display market, manufacturers must continue to improve image quality. The motion-blur artifact seen on TFT-LCDs has recently received a great deal of attention. Among the recent applications, the Pi-cell, also known as Optical Compensation Bend (OCB) mode has been found to be effective in reducing this artifact. Due to the LC-cell structure and the driving scheme, the Pi-cell so far is the fastest-response LCD mode among the commercialized LCD modes.

Since the Pi-cell has a fast response property, the field sequential color LCD (FSC-LCD) which displays R, G and B colors in sequence in a pixel is very promising for the high-resolution display as the information displays [2]. Further, FSC-LCD can be realized a high brightness display without the need of color filters which reduces the transmittance of the LCD panel by 70% (not including LC). In this dissertation, the high image quality Pi-cells will not only be designed and improved for general LCD applications but also for FSC-LCD type.

Fig. 1-1 The various kinds of LCDs [1].

1.1 Liquid crystal displays (LCDs)

A cross-section of an LCD, as shown as Fig. 1-2, reveals its elements. The LC cell is at the center of the display where the liquid crystal is located. Transparent electrodes patterned on each pane of glass encompass the liquid crystal. Light passes through a bottom polarizer that orients the light to a single state of polarization by absorbing over 50% of the incoming unpolarized light. The orientation of the liquid crystals can be changed by applying a voltage to the electrodes in order to change the level of illumination displayed in each sub-pixel. However, if a voltage is applied, the liquid crystals align to the electric field and do not rotate the light, allowing the top polarizer to block it completely. By applying an intermediate voltage, the liquid crystal can be partially oriented to control the transmittance of the incoming light, creating shades of gray as shown in Fig. 1-3. Adding a color filter to the LCD panel creates color displays. In a color LCD, each red, green and blue sub-pixel is individually controlled, allowing varying amounts of red, green, and blue light through to the viewer for each pixel.
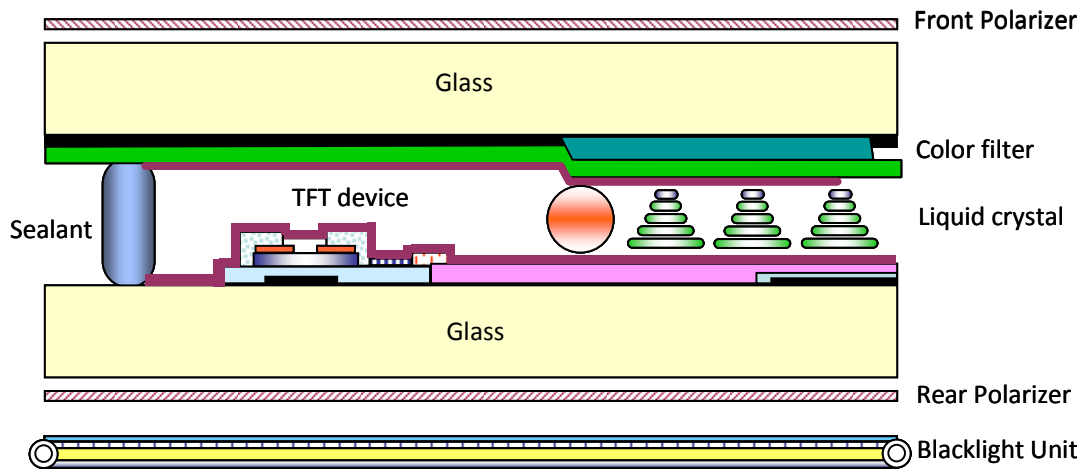
Fig. 1-2 The cross-section view of a LCD.
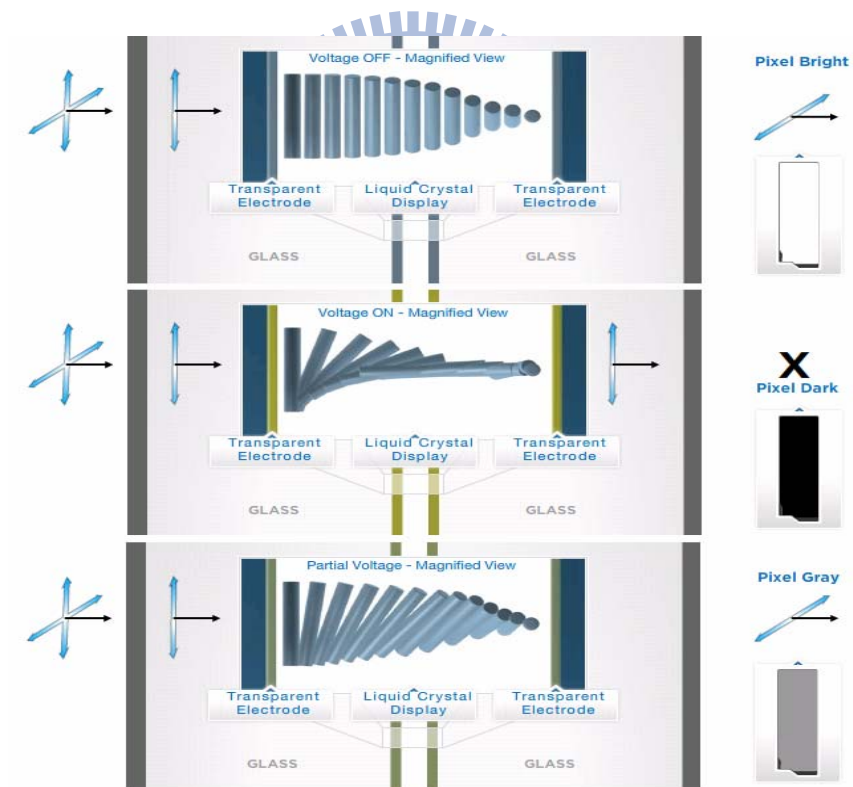
Source: *Dr. Chun-Ho Chen's dissertation for Ph. D in NCTU, 2009.*

Fig. 1-3 The ON-state, OFF-state, and gray-state of one pixel on a general TFT-LCD.

1.2 Motion Blur of the LCD Panel

Due to the TFT-LCD driving scheme, the sub-pixels of a LCD panel are driven by hold-type square function. When the object displayed on the TFT-LCD moves fast as in sports, the edge of the object image will become blurred with multiple images, shown in Fig. 1-4. The motion quality of LCD TVs is evaluated by using the well-known figure of merit — VESA's Moving Picture Response Time (MPRT).
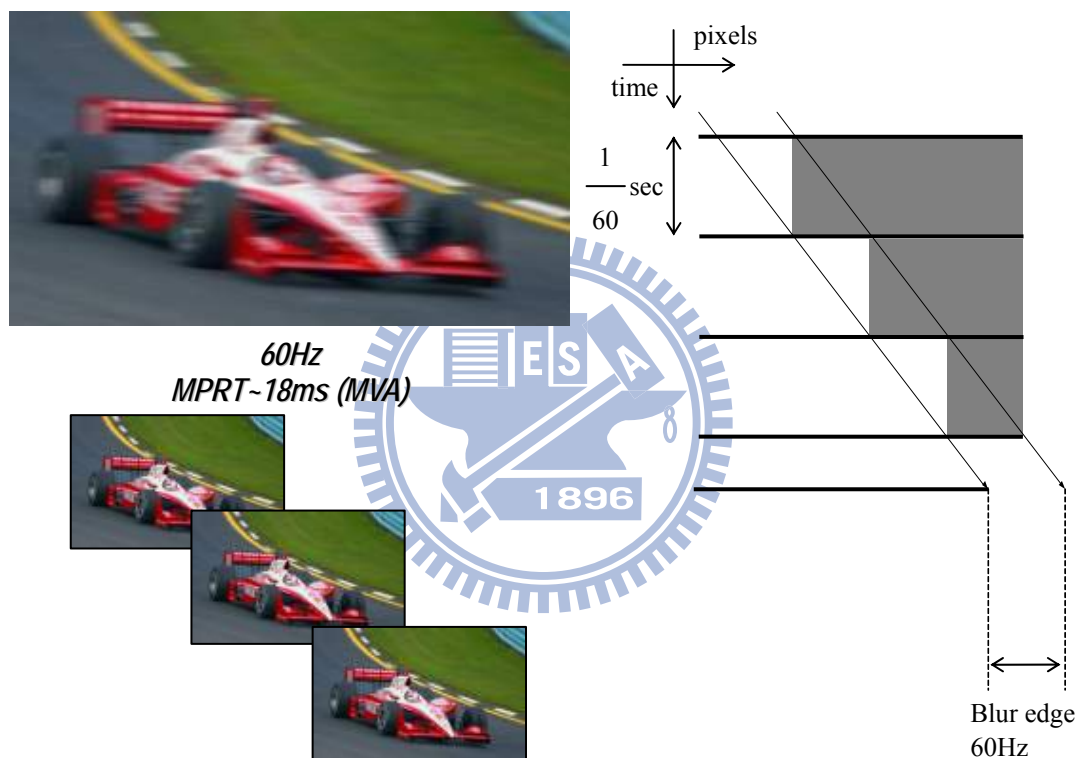
Fig.1-4 The motion blur effect of the TFT-LCD driven at 60Hz frame rate.

In order to improve the motion quality of a TFT-LCD, the impulse driving scheme on TFT-pixels, simulates the CRT's impulse type light emission, has been adopted. There are many approaches in recently proposed technologies; the simplest one is *Black Insertion* (*BI*) whose driving scheme is shown in Fig.1-5. By using *BI* technology, which can alternate between a black data frame and a display data frame,

the MPRT of a general TFT-LCD TV can approach 12ms; yet, the MPRT of a CRT is 4ms. However, the result can not be satisfied with image quality, because the MPRT is still larger than CRT's and the brightness of a LCD needs to be compromised. According to the various proposed technologies such as black data insertion, black frame insertion, scanning backlight and 120 Hz Motion Estimation Motion Compensation (MEMC) applications, a double frame rate to drive the LC panel is needed for these improving methods. Therefore, the fast response LC mode is a key requirement for motion blur improvement. Among all of LC modes, the Pi-cell is a strong candidate in commercialized LCD modes [3] for resolving the motion blur issue.
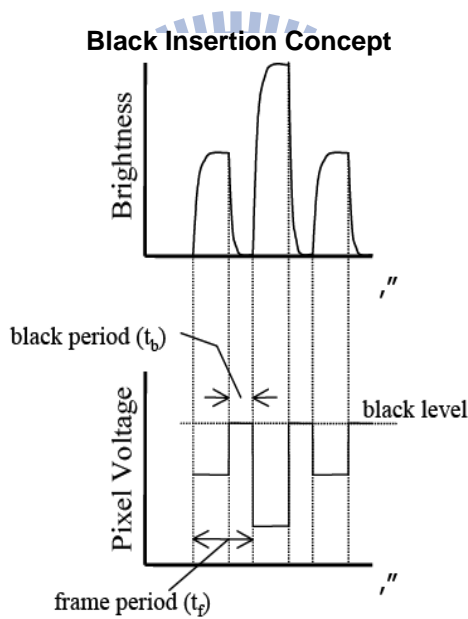
Fig. 1-5 The concept of the black insertion technology.

1.3 FSC-LCD Application

A TFT-LCD system is commonly illuminated by a constant full-on conventional CCFL backlight. The generated light propagates through two sets of polarizers, color filters, diffusers and redirection foils, and in each of these components, substantial

proportions of light are scattered and absorbed. Overall, the efficiency of the above optical stack amounts to approximately 5-10%.

Normal LCD--Spatial Colored

White Backlight

Colored Sub-pixels

1 frame = 1 field
Frame rate = 60 Hz

FSC-LCD--Temporal Colored

Colored Backlight

Time

Monochrome Pixel
=3 x Sub-pixel

1 frame = 3 field
Field rate = 180 Hz
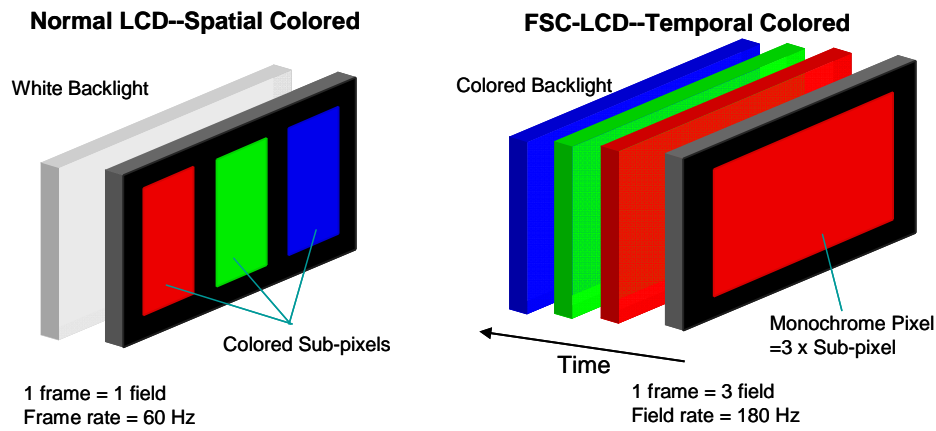
Fig. 1-6 The normal LCD with color filters and the FSC concept.

Time

full color image

| Data Load | LC Set | LED Flash | Data Load | LC Set | LED Flash | Data Load | LC Set | LED Flash |

Red   Green   Blue

5.56 ms

1 Frame: 1/60 Sec ~16.7 ms
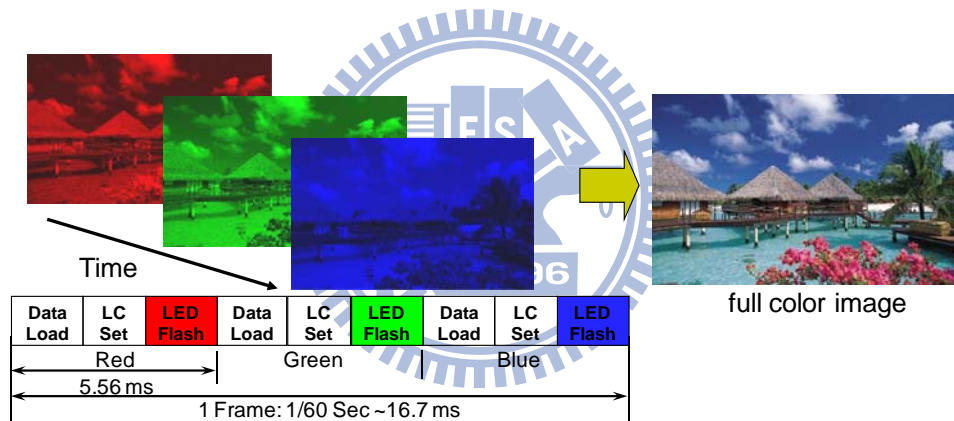
Fig. 1-7 The display mechanism of an FSC-LCD.

Most LCDs rely on spatial color synthesis to produce vivid saturated color images by juxtaposing strip color-filter (typically RGB) sub-pixels. However, color filters absorb roughly 70% of light and are therefore highly inefficient. To significantly improve LCD power efficiency, it is therefore appealing to remove the color filters and rely on temporal color synthesis to create full-color images. The display concepts of a conventional TFT-LCD and a FSC-LCD are shown in Fig. 1-6. Such FSC-LCDs rapidly flash the three primary colors time-sequentially, as illustrated in Fig. 1-7, such that the colors are mixed by means of temporal integration in the

6

eyes and all three colors seem present simultaneously [1][4-8]. Colored LEDs are an ideal light source for this mode of illumination. To prevent luminance flicker, a three-primary system requires a minimum refresh rate of 180 Hz. In other words, FSC-LCD technology also needs a sufficiently fast response LC mode.

1.4 Fast Response LC Mode

Three kinds of LCD modes are currently in the mainstream of the LCD industry. They are multi-domain vertically aligned (MVA) [9], in-plane switching (IPS) [10], and optically compensated bend (OCB) [11] mode LCDs, whose cell structures and driving concepts are shown in Fig. 1-8. Their distinguished feature of "wide viewing angle" is an important requirement for LCD-TV applications. Therefore, these three wide-viewing LC modes are selected to develop the further fast-switching requirement.

Though IPS and MVA modes have very outstanding wide-viewing characteristic, their response times are not fast enough for high-frame-rate display applications, such as field sequential color LCD or temporally multiplexing 3D display. Therefore, a novel technique, Pi-cell also known as OCB mode, was proposed to fulfill these requirements. The comparisons of different LC modes are listed in Tab. 1-1. Though OCB-LCD is regarded as the fastest switching LCD mode among the LCDs, some issues still need to be resolved. Among them, the most critical issue is the recovery from the bend state back to the splay or twist states.

As shown in Fig. 1-8 (c), the Pi-cell is normally operated in the bend state; however, because of the topological difference between the ground splay state and the bend state, a nucleation transition has to be completed before operation. The transition

can be initiated by applying a critical voltage (Vcr), and then this voltage is held to sustain the device in the bend state. However, the Pi-cell still has the tendency of relaxing into the splay state. Therefore, we will propose two novel Pi-cell structures to resolve transition issue: one is to form a nanostructure by coating nano-particles before PI treatment to enhance the transition rate from splay to bend state; the other one is to use reactive monomers to modify the pretilt angle of alignment layer whose anchoring energy may be changed for the contrast ratio improvement.

Tab. 1-1 The characteristics comparisons of different LC modes.

(Data source: Chung Hwa Picture Tube, LTD)

Items	TN	IPS	MVA	Pi-cell
Driving	◎	◎	◎	○ (state transition)
Intrinsic Response (ms)	○ (~12)	△ (~20)	△ (~20)	◎ (<3)
Intrinsic Contrast Ratio	△ (600:1)	○ (800:1)	◎ (1200:1)	△ (600:1)
Viewing angle	△	◎	○	◎
Fabrication	◎	○	○	◎

◎: Excellent ○: Good △: Acceptable X: Poor

(a)   (b)

Splay state
Bend state (Driving Mode)

(c)
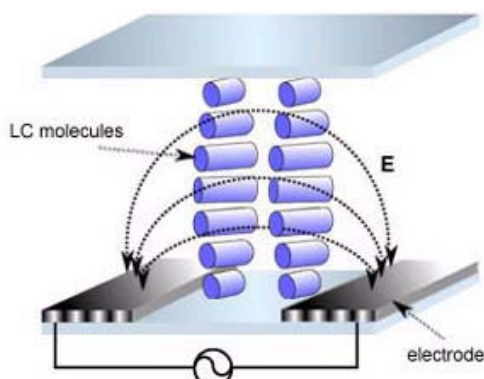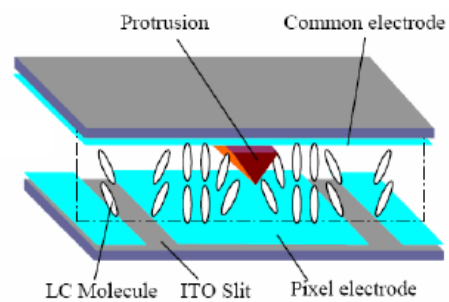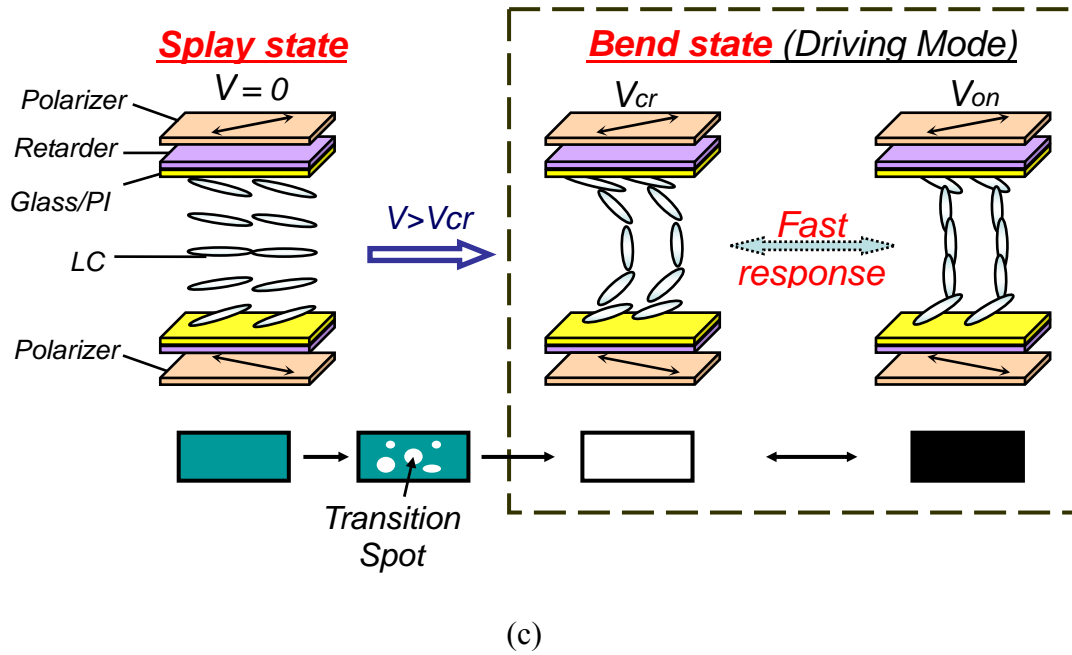
Fig. 1-8 The cell structures and driving schemes of (a) IPS, (b) MVA, and (c) Pi-cell.

1.5 Motivation and objective of this dissertation

With the growth of the information industry, the display technique requirements have become increasingly demanding. The desirable features are high contrast ratio, high power efficiency, high resolution and good visual quality. To fulfill these features, we designed and demonstrated the new technologies to achieve high contrast ratio and clear motion image quality. We did this by using conventional Pi-cell, also named OCB mode, in the OCB-LCD TV. To evaluate the motion quality of LCD TVs, we used the Moving Picture Response Time (MPRT). By applying the *Dynamic Scanning Backlight with Black Insertion* (*DSBBI*) technology previous proposed by our research team, the MPRT of a 32-inch OCB-LCD TV can achieve 5.9 ms in average gray-to-gray levels, which is comparable to CRT TV (MPRT~4ms) but better than other LCD modes [12]. By changing the structure of the LC cell, the contrast ratio of OCB-LCD TVs can be improved by 60% by adjusting the gamma curves with respect to R, G and B individually. With dynamic controlled backlight luminance, the contrast

ratio of OCB-LCD TVs can even achieve greater than 1000:1 at 50% dimming setting [3].

To further realize the features of high power efficiency, adopting the FSC-LCD structure is a good candidate. The requisite components of FSC-LCD are the fast switching modes of liquid crystal and the backlight module. Among these requirements, the most urgent one is the fast response LC mode because the current research in the field is still short of realizing the FSC-LCD without the color break-up (CBU) phenomenon. The OCB-LCD modes possess the possibility to achieve the FSC-LCD.

In the demonstration of a 32-inch OCB-LCD TV, using conventional Pi-cell, we found two key issues that need to be resolved. First, applying the critical voltage bias for the LC state transition from splay state to bend state and keeping it in stable bend state are strict. To hold the Pi-cell in stable bend state, the applied voltage should be larger than the critical voltage of blue light. As the result, the transmittance and contrast ratio of the Pi-cell must be degraded. Therefore, it is necessary to develop a novel Pi-cell that is stable in bend state without bias voltage [13]. Second, in order to obtain good dark state and wide viewing angles in all viewing directions, we used commercial OCB-WV films to compensate for the viewing angle dependence of bend alignment LC cell [14]. However, the retardation mismatch occurs when the OCB-LCD shows the low gray-level images or patterns at large viewing angles and results in the red and blue light leakages corresponding to the right and left sides of rubbing direction respectively. Therefore, to design a high contrast ratio and transmittance of Pi-cells without using OCB-WV films is a challenge. In order to realize high image quality displays which fulfill the aforementioned features, it is very important to find the solutions to the two key issues mentioned above.

In this dissertation, I will describe the tasks completed on the aspects of the Pi-cell and the future works for performance improvements.

1.6 Organization of this dissertation

This dissertation is organized as follows: the principle of deformation mechanism of LC cells, the mechanical properties and transition scheme of a Pi-cell are presented in **Chapter 2**. The continuum theory, anchoring effect, homogeneous and heterogeneous nucleation theory are described. Additionally, this chapter also presents the operation principle and special characteristics of a Pi-cell. In **Chapter 3**, the standard TFT-LCD fabrication processes are introduced. And the instruments used in experiment for optical property measurements are described. The basic measuring concept and set-up of the measurement systems are also described in details. In **Chapter 4**, the novel *nanostructure enhanced Pi-cell* (*NE-Pi-cell*) is proposed. The fabrication methods of nanostructures are investigated and optimized; the limitation of nano-particle density is also analyzed. In addition, the dynamic observations and transition rate of a conventional Pi-cell and proposed *NE-Pi-cell* are presented and evaluated. In **Chapter 5**, the transition-free *RMM-Pi-cell* is proposed. The novel structure and the fabrications of a *RMM-Pi-cell* are presented. The performance comparisons between a conventional Pi-cell and a *RMM-Pi-cell* are investigated. The potential issue of the *RMM-Pi-cell* is also discussed here. Finally, the summary of the dissertation and future works are given in **Chapter 6**.

Chapter 2

Theory and Principle

The deformation mechanism of a LC cell and the principle of state transitions in a Pi-cell are introduced. The continuum theory is used to calculate the Gibbs's energy of a certain state, and Rapini-Papoular approach is used to calculate the alignment effect on the orientation of LC director. In the principle of state transitions in a Pi-cell, the well-known nucleation theory method is illustrated. In order to study the rate of state transitions, we propose hetero-nucleation theory to explain why the heterogeneous surface energy status can shorten the transition time in a Pi-cell.
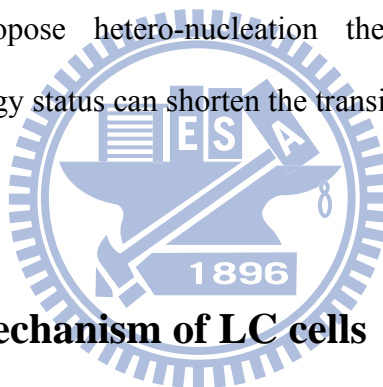
2.1 Deformation Mechanism of LC cells

In LCDs, an electric field is often applied to cause reorientation of the LC molecules. The switching performance of an LC device relies on its cell structure design. The Ossen-Frank continuum theory [15-18] is well-used by the LCD researchers. A basic continuum theory considers that the elastic constants of LC molecules determine the restoring torques arise when the system is perturbed from its equilibrium configuration. It is the balance between the electric torque and the elastic restoring torque that determines the LC's static deformation pattern. Taking more factors into consideration, such as the electric field, the magnetic field, and the anchoring effect makes the equation more appropriate to the actual LCD cases. The detailed description of continuum theory is explained as follows.

2.1.1 Continuum Theory

The Ossen-Frank continuum theory is well-known for the calculation of the equilibrium configuration of LC directors in a cell. LCs exhibit curvature elasticity. When an electric filed is applied to an LCD device, the LC molecules will be reoriented. The electric torque needs to be balanced by elastic restoring torque determines the LC's deformation pattern. Any static deformation of LCs can be divided into a combination of three basic deformations: splay, twist, and bend, as illustrated in Fig. 2-1.

(a) $\nabla \cdot \mathbf{n} \neq 0$ (b) $\mathbf{n} \cdot \nabla \times \mathbf{n} \neq 0$ (c) $\mathbf{n} \times \nabla \times \mathbf{n} \neq 0$
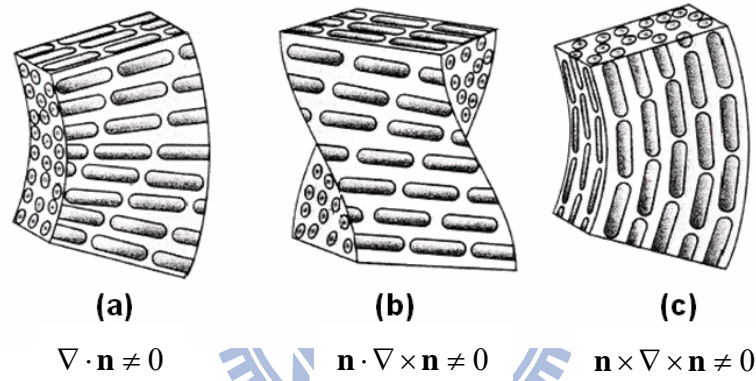
Fig. 2-1 Schematic drawing of (a)splay, (b)twist, (c)bend in LC cell [19].

We consider a nematic LC cell in the *xy* plane. The *z* axis is chosen to be perpendicular to the cell, so that the cell is located between *z* = 0 and *z* = *d*. Initially, the LC molecules are aligned parallel to the *xy* plane. An electric field is applied in the LC cell. Following the notation of Ossen-Frank continuum theory, the energy densities of a deformed LC and the electromagnetic field can be written as Eq. (2-1) [20].

$$F = \frac{1}{2}\left[k_{11}(\nabla \cdot \mathbf{n})^2 + k_{22}(\mathbf{n} \cdot \nabla \times \mathbf{n})^2 + k_{33}(\mathbf{n} \times \nabla \times \mathbf{n})^2\right] - \frac{1}{2}(\mathbf{E} \cdot \mathbf{D}) \qquad (2\text{-}1)$$

where k_{11}, k_{22}, and k_{33} are the splay, twist and bend elastic constants, respectively and

n is the unit vector representing the director distribution in the cell. The elastic

constants are strongly temperature dependent. **E** is the applied electric field and **D** is

the displacement field vector.

Consider twist and tilt mode. The director **n** is uniformity twisted as a function of

z, so the initial director distribution can be expressed,

$$\mathbf{n} = (\cos\phi, \sin\phi, 0) \tag{2-2}$$

A uniform electric field is applied along the *z* axis. As a result, the directors are tilted

toward the direction of the electric field. This leads to redistribution of the director **n**

as a function of *z*. Therefore, the director can be written,

$$\mathbf{n} = (\cos\theta\cos\phi, \cos\theta\sin\phi, \sin\theta) \tag{2-3}$$

where (θ, ϕ) are the positioned angles of the LC director, denote the polar coordinates

rotated about *y* axis by θ and about *z* axis by ϕ. Substituting Eq. (2-3) to Eq. (2-1), the

elastic energy density is obtained as:

$$U_{EL} = \frac{1}{2}\left[k_{11}\cos^2\theta + k_{33}\sin^2\theta\right]\left(\frac{d\theta}{dz}\right)^2 + \frac{1}{2}\left[k_{22}\cos^2\theta + k_{33}\sin^2\theta\right] \times \cos^2\theta\left(\frac{d\phi}{dz}\right)^2 \tag{2-4}$$

The electromagnetic energy density term is

$$U_{EM} = \frac{1}{2}\mathbf{E}\cdot\mathbf{D} \tag{2-5}$$

Actually, we are care about the change of the electromagnetic energy density due to

the change of the dielectric constant ε as the LC director distribution changes.

Considering the first case: a constant voltage, the electric field *E* is a constant

(*E=V/d*), regardless the magnitude of the dielectric constant. The net change of the

electromagnetic energy density due to a change of the dielectric constant can be written as:

$$\Delta U_{EM} = \frac{1}{2}\varepsilon E^2 - \frac{V\Delta Q}{Ad} - \frac{1}{2}\varepsilon_0 E^2 \qquad (2\text{-}6)$$

where A is the area of electrodes, d is the separation between the electrodes, and ΔQ is additional charges supplied by power supply. It can be denoted by

$$\Delta Q = A(\varepsilon - \varepsilon_0)\frac{V}{d}, \quad E = \frac{V}{d} \qquad (2\text{-}7)$$

Substituting Eq. (2-7) into Eq. (2-6), we obtain

$$\Delta U_{EM} = \frac{1}{2}\varepsilon_0 E^2 - \frac{1}{2}\varepsilon E^2 \qquad (2\text{-}8)$$

where ε_0 is the initial dielectric constant. A larger final dielectric ε leads to a lower energy density.

Considering another general case, the surface charge density is constant. Therefore, the displacement field D is a constant. The change of electromagnetic energy density due to a change of dielectric constant can be written

$$\Delta U_{EM} = \frac{1}{2}\frac{D^2}{\varepsilon} - \frac{1}{2}\frac{D^2}{\varepsilon_0} \qquad (2\text{-}9)$$

We postulate the LC cell is uniform in xy plane, and the electric field E is applied along z axis. An application of Maxwell's equation and the boundary condition on the surface lead to:

$$E_x = E_y = 0 \qquad (2\text{-}10)$$

Eq. (2-9) can be written

$$\Delta U_{EM} = \frac{1}{2} \frac{D_Z^2}{\left(\varepsilon_\parallel \sin^2\theta + \varepsilon_\perp \cos^2\theta\right)} - \frac{1}{2} \frac{D_Z^2}{\varepsilon_\perp} \tag{2-11}$$

where $\varepsilon_\perp$ is the initial dielectric constant, D_Z (=constant) is the z component of the displacement field vector. The second term is a constant independent of the director orientation $\theta(z)$. And the component D_Z can be written

$$D_Z = (\varepsilon_\perp \cos^2\theta + \varepsilon_\parallel \sin^2\theta)E \tag{2-12}$$

The total free energy in the cell is given by

$$U = \int_0^d \left(U_{EL} + \Delta U_{EM}\right)dz$$
$$= \frac{1}{2}\int_0^d \left[F_1\left(\frac{d\theta}{dz}\right)^2 + F_2\left(\frac{d\phi}{dz}\right)^2 + \frac{D_Z^2}{\left(\varepsilon_\parallel \sin^2\theta + \varepsilon_\perp \cos^2\theta\right)} - \frac{D_Z^2}{\varepsilon_\perp}\right]dz$$

where $\tag{2-13}$
$$F_1 = k_{11}\cos^2\theta + k_{33}\sin^2\theta$$
$$F_2 = \left[k_{22}\cos^2\theta + k_{33}\sin^2\theta\right]\cos^2\theta$$

The preferred LC director distribution functions $\theta(z)$ and $\phi(z)$ can be acquired by minimizing the total free energy using variation method. i.e. Let $\delta U=0$ and give suitable boundary conditions, then the $U_{min.}$ can be obtained at the same time.

2.1.2 Anchoring Effect

The LC alignment affects the equilibrium state, switching property, and director configuration of an LC cell. This alignment is generally achieved by the anchoring effect with a pretreated layer. Most preferably, polyimide is used owing to its low cost, high stability, and easy process. Two major methods are used to pre-treat the alignment material: mechanical rubbing and photo-alignment. The mechanical rubbing method is executed by a roller covered with woolen texture. By brushing in the same direction, the alignment layer is strained, and this strain aligns the LC

director in a certain direction. The other method of pre-treating the alignment material is to use polarized UV light to orient the molecules of alignment layer in a certain direction. This method can be used along with a photo-mask to make multi-directional alignments in one substrate, but the uniformity is still an issue.

This stabilization mechanism can be expressed by Rapini-Papoular approach [21-23] as follows:

$$F_s = F_\theta + F_\phi \tag{2-14}$$

$$F_\theta = \frac{1}{2} W_\theta \sin^2(\theta - \theta_0) \tag{2-15}$$

$$F_\phi = \frac{1}{2} W_\phi \sin^2(\phi - \phi_0) \tag{2-16}$$

where θ and ϕ denote the polar and azimuthal angles, F_s denotes the total free energy resulting from the anchoring effect, F_θ denotes the free energy component in terms of the polar angle, F_ϕ denotes the free energy component in terms of the azimuthal angle. W_θ and W_ϕ are the constants denote the interactions between the substrates and the LC directors. θ_0 and ϕ_0 are the equilibrium angles with respect to the polar and azimuthal dimensions.

Considering the anchoring effect, the continuum equation mentioned in 2.1.1 needs to be modified as follows. The orientation distribution of stabilized LC directors of a LC cell can be illustrated by the equation.

$$F = \frac{1}{2}\left[k_{11}(\nabla \cdot \mathbf{n})^2 + k_{22}(\mathbf{n} \cdot \nabla \times \mathbf{n})^2 + k_{33}(\mathbf{n} \times \nabla \times \mathbf{n})^2\right] - \frac{1}{2}(\mathbf{E} \cdot \mathbf{D}) + F_s \tag{2-17}$$

2.1.3 The Mechanical Properties of Pi-cells

In a Pi-cell, the LC directors have a bend distribution with a total bend of 180°

(π) from surface to surface when the Pi-cell is in operation. The alignment arrangements of upper and lower substrates in a Pi-cell are parallel. Generally, the initial state of a Pi-cell prefers to be aligned in splay state. By calculating the Gibbs's free energy in Eq. (2-17), the stable state corresponding to the applied voltage can be obtained. As shown in Fig. 2-2, the cell is more stable in splay state than in bend state without applying a voltage. While applying a voltage larger than critical voltage, the bend state becomes more stable than the splay state [24-26].
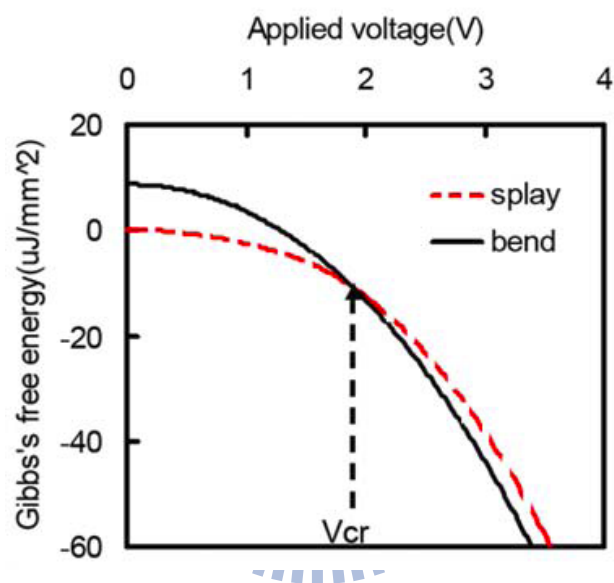
Source: T. Uchida et al., SID'00 Digest 31, 26 (2000).

Fig. 2-2 Gibbs's free energy of bend and splay states as a function of applied voltage [24].

Take the pretilt angle into account; the Gibbs's free energy diagram can be used to determine the pretilt angle of a Pi-cell which is in the bend state initially. As shown in Fig. 2-3 (a), if the pretilt angle is much lower than critical pretilt angle, the Gibbs's free energy of the bend state is too large to be stabilized. In other words, if the pretilt angle is higher than critical pretilt angle, the bend state can be stabilized without applying a voltage. In heterogeneous case, the bend state can be initiated with nucleation by applying a voltage, as shown in Fig. 2-3 (b) [11][24][27-30].
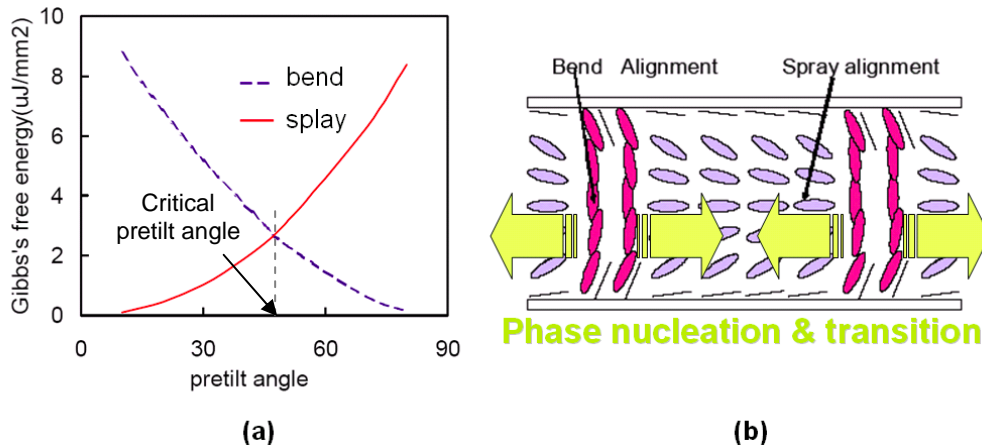
Source: T. Uchida et al., SID'00 Digest 31, 26 (2000).

Fig. 2-3 Transition in Pi-cell, (a) is pretilt angle effect and (b) is the nucleation in a transition process [24][27].

Furthermore, the Pi-cell has the rapid response time because the cell is operated between the bend state at the critical voltage (V_{cr}) and the near homeotropic state at high voltage. The symmetric director configurations in the lower and upper parts of the LC layer, regarded as two halves of a Fréedericksz cell, imply the equivalent cell gap is one half of the real LC layer. Because the response time of a LC cell is proportional to the square of cell gap, the response time of a Pi-cell has improved by a factor of four.. The schematic diagram is shown in Fig. 2-4. Besides, the flow effect of a Pi-cell leads to the response time improvement is more than four times. The LC flow in Pi-cell is toward the same direction; therefore, the backflow effect can be ignored. The comparison of the flow effect in a Pi-cell and the anti-parallel backflow, which slows down the response of LCs, in a TN-cell is shown in Fig.2-5.

In addition to fast response, the optically self-compensated property is also a key design factor in a Pi-cell. Due to the symmetric director configurations of a Pi-cell, the optical retardations are almost the same, no matter people see from left or right sides, as shown in Fig. 2-6. Therefore, Pi-cell is a kind of wide viewing angle technologies.
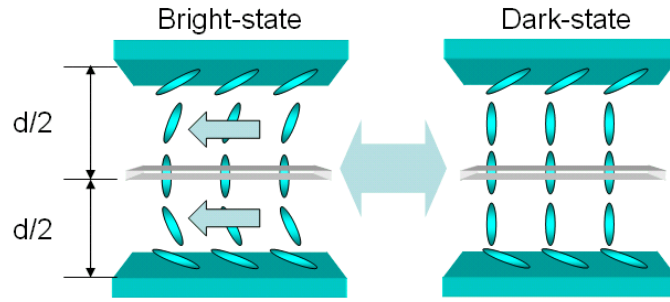
Fig. 2-4 Schematic diagram of two equivalent halves of a Fréedericksz cell.
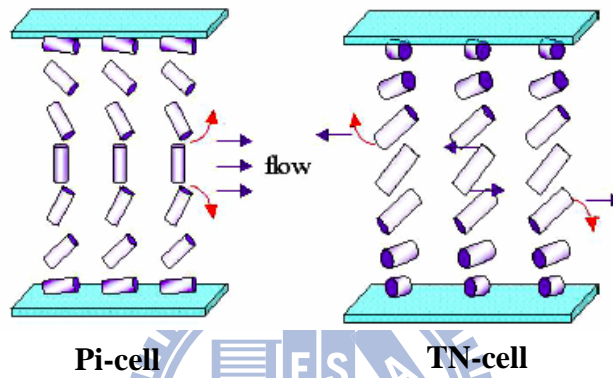
Fig. 2-5 Flow effect in Pi-cell and TN-cell.
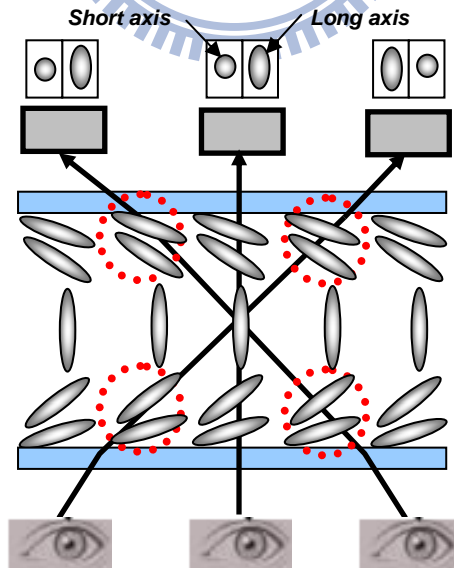
Fig. 2-6 The illustration of optically self-compensated property in a Pi-cell.

2.2 State Transition Scheme of a Pi-cell

Pi-cell [31] possesses fast response time, due to lacking of backflow during molecular relaxation [32-36] in its bend state, for liquid crystal display (LCD) application. Generally, the Pi-cell is operated in the bend state; a nucleation transition has to be completed to operate the Pi-cell in the bend state. The Pi-cell, however, has five distinct states in its transitions, illustrated in Fig.2-7. There are (1) the splay ground state, (2) the symmetric splay state (Hs), (3) the asymmetric splay state (Ha), (4) the bend state, and (5) the 180° twist state [37-39]. The lowest free energy state is splay state without an applied voltage. When applied a voltage higher than the first critical voltage V_{C1}, Hs state would be formed under the same surface condition on both sides of a Pi-cell. The Hs state, then, quickly turned into asymmetric Ha state. As the applied voltage was further increased beyond the second critical voltage V_{C2}, also called the critical voltage, denoted Vcr, of a Pi-cell, the bend state became the stable state. The voltage had to be kept larger than the critical voltage to sustain the cell in the bend state; otherwise, the LC molecules would be relaxed into twist or splay states in a Pi-cell. In TFT-LCD applications, due to the limitation of the maximum driving voltage (~ 6V) and the requirement of sustained voltage to prevent recovery of the splay state, the Pi-cell is generally driven in the range between 2 ~ 6V [40]. In the transition scheme, there are two nucleation processes included; one is Hs (or Ha)-to-bend state, the other one is bend state relaxed into twist state.
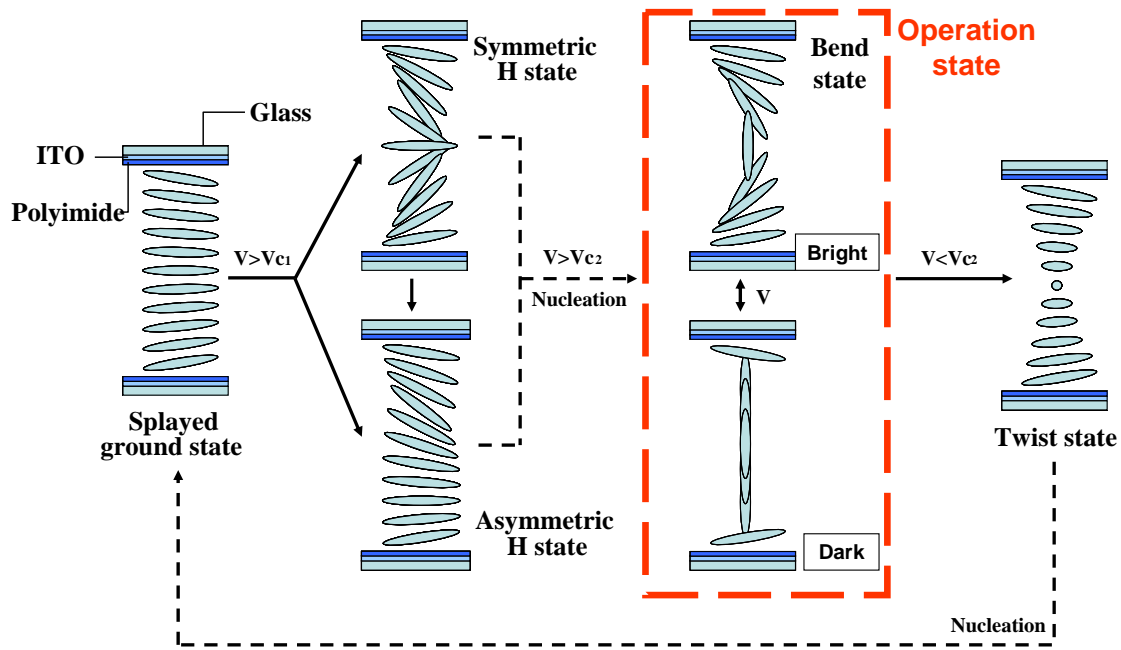
Fig.2-7 The commonly known states form in Pi-cell devices [41].

2.2.1 Nucleation Theory

Classical nucleation is the extremely localized budding of a distinct thermodynamic phase. Some examples of phases that may form via nucleation in liquids are gaseous bubbles, crystals, or glassy regions. Nucleation generally occurs with much more difficulty in the interior of a uniform substance, by a process called *homogeneous nucleation*. The creation of a nucleus implies the formation of an interface at the boundaries of a new phase. As mentioned above, the splay-to-bend transition in a Pi-cell has to be completed via so-called nucleation process. In the process, an interface forms to be the boundary between splay and bend states. When the extra voltage, higher than the critical voltage, is applied to the Pi-cell, the extra driving power will force for nucleation and bring about a change in free energy per unit volume, G_v, between splay and bend states. This change in free energy is balanced by the energy gain of creating a new volume, and the energy cost due to

creation of a new interface. When the overall change in free energy, ΔG is negative, nucleation is favored.

Some energy is consumed to form an interface, based on the surface energy of each phase. If a hypothetical nucleus is too small (known as an unstable nucleus or "embryo"), the energy that would be released by forming its volume is not enough to create its surface, and nucleation does not proceed. The critical nucleus size can be denoted by its radius, and it is when $r = r*$ (or r critical) that the nucleation proceeds.

In the classic case [42] of a spherical cluster that liberates $-G_v$ J/cm^3 during formation (here G_v is a negative quantity), but which must pay the positive cost of σ J/cm^2 of surface interfacing with the world around, the free energy needed to form a cluster of radius r is

$$\Delta G = \frac{4}{3}\pi r^3 G_v + 4\pi r^2 \sigma \qquad (2\text{-}18)$$

where the first term shows the energy gain of creating a new volume and the second term shows the energy loss due to surface tension of the new interface. It costs free energy to add molecules to this cluster (because $\frac{dG}{dr} > 0$) until the radius reaches to the critical value, $r* = -\frac{2\sigma}{G_v}$. And we can find the free energy needed to form the critical radius by $\Delta G* = \frac{16\pi\sigma^3}{3G_v^2}$, which is the maximum ΔG (where $\frac{dG}{dr} = 0$). The illustration is shown in Fig. 2-8 [43-44].
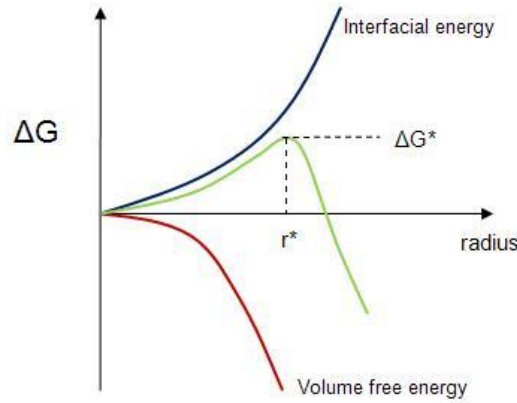
Fig. 2-8 Illustration of free energy change in nucleation process [44].

As mentioned above, *homogeneous nucleation* occurs with much difficulty. Actually, another nucleation type, called *heterogeneous nucleation*, occurs much more often than *homogeneous nucleation*. It forms at preferential sites such as phase boundaries, defects or impurities like dust and requires less energy to than homogeneous nucleation. At the preferential sites, the effective surface energy is lower, thus diminished the free energy barrier and facilitating nucleation. Surfaces promote nucleation because contact angles greater than zero between phases encourage particles to nucleation. In splay-to bend-transition case we studied, at the specially created preferential sites, the free energy needed for *heterogeneous nucleation* is equal to the product of *homogeneous nucleation* and a function of contact angle, which results the barrier energy needed for *heterogeneous nucleation* reduced.

$$\Delta G_{heterogeneous} = \Delta G_{homogeneous} * f(\theta) \tag{2-19}$$

Where $f(\theta) = \frac{1}{2} - \frac{3}{4}\cos\theta + \frac{1}{4}\cos^3\theta$, θ is limited in the range between 0 and π.

The illustration of difference between *homogeneous* and *heterogeneous nucleations* in energy barriers is shown in Fig. 2-9.

24
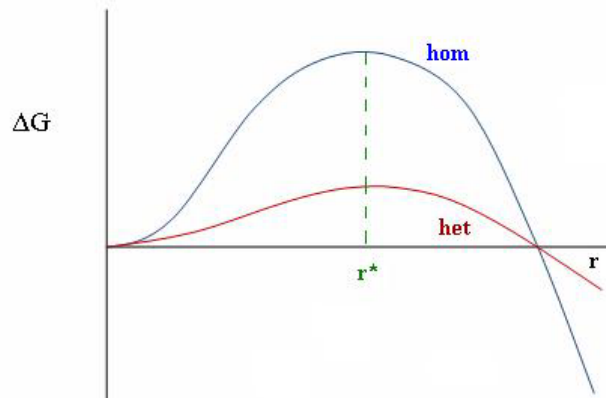
Fig. 2-9 Comparison of the free energy barrier for heterogeneous and homogeneous nucleations [44].

The barrier energy needed for *heterogeneous nucleation* is reduced, but the critical radius remains unchanged. In other words, the heterogeneous surfaces increase the change of the strain energy density included in Gibbs free energy density (i.e. negative quantity becomes larger.) [44-45]. The transition process of a Pi-cell, the uniform distribution of nano-particles will affect the rate, uniformity, and strength of the transition.

2.2.2 Transition Rate

The transition rate in Pi-cell is positively correlated with nucleation rate per unit volume. The relationship is shown as following equation [44].

$$I \propto N\nu \exp(\frac{-\Delta G^*}{k_B T}) \propto \frac{1}{\Delta t} \qquad (2\text{-}19)$$

Where ΔG^* is free energy barrier ($\Delta G^* > 0$). ν is the attempt frequency; N is the number of potential nucleation sites per unit volume; k_B is the Boltzmann constant and Δt is transition time. The transition rate depends on the attempt frequency, the number density of nucleation sites and probability of successful attempts. The smaller ΔG^*

and the larger *N* are, the larger transition rate is.

The number of nucleuses of a certain size formed is a function of the total number of atoms in the system, the free energy to create a nucleus of that size, and the temperature. The number of nucleuses increases with increasing temperature. As temperature (significantly below melting temperature or Tni, which is nematic-isotropic transition temperature.) increases, molecules are able to get to the site of nucleation at a fast enough rate to promote the growth of the nucleus. Therefore, nucleation rate is dominated by the diffusion. However, as temperature increases, the fluctuations of molecules increase and molecules tend to escape from the nucleus, resulting in a decrease of nucleation rate [45-46].

Source: http://en.wikipedia.org/wiki/Nucleation
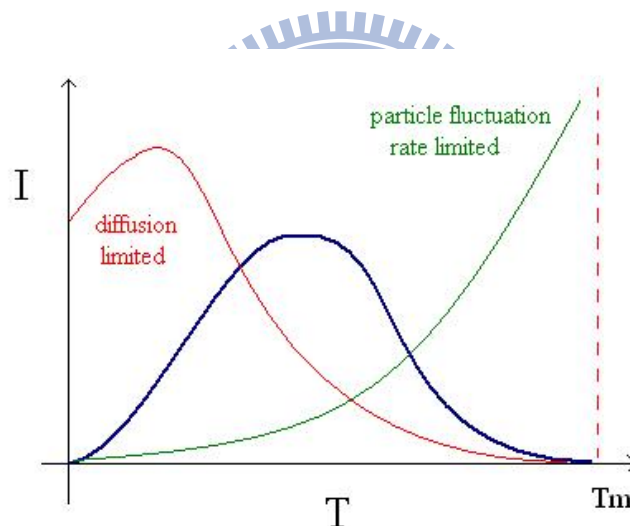
Fig. 2-10 Nucleation rate versus temperature, which is illustrated by diffusion limited and fluctuation rate limited [44].

In the transition process of a Pi-cell, the transition time measurement is often kept at room temperature. Therefore, the thermal dynamic behavior was not discussed in the study. The study was focused on the nucleation rate (or transition rate) increased by the heterogeneous surfaces.

2.3 Summary

In chapter 2, the continuum theory was used to calculate the Gibb's energy of the LC profiles, and the nucleation theory was used to explain the transition processes in a Pi-cell, were illustrated. From the chapter, we could realize the driving behaviors of a Pi-cell and know how to resolve the transition processes in a Pi-cell. If we wanted to resolve the transition issue, we needed a higher pretilt angle at the cell boundary to change the equilibrium LC profiles in a Pi-cell or a heterogeneous nucleation to enhance the transition rate. According to these studies, we then proceeded two research objectives to resolve the transition issue in the dissertation.

Chapter 3

Device Fabrication and Measurement

The standard fabrication technologies of LCD are described. These fabrications will be used to make our designed devices. After the devices and special treatment substrates being fabricated, the cell characterizations of the optical performance, iso-contrast diagram and cell gap are measured with the Laser optical system assembled by our laboratory, Conoscope system and UV/Vis spectrometer LAMBDA 950 made by PerkinElmer, respectively. Then, the morphologies of the nano-particle coated substrates and RM films' thicknesses are investigated by Atomic Force Microscope (AFM).

3.1 Standard LCD Fabrication Technology

A LCD device is fabricated by stacking two substrates with intermediate liquid crystal. The standard fabrication technology of a LC cell is shown in Fig. 3-1. Two substrates need to be prepared in advance; one substrate is formed well-known thin film transistors (TFT) to be a pixel array, and another one substrate is fabricated by color filter (CF) processes for color separation. In general, the standard a-Si TFT fabrication needs five sequential masks for photolithography processes include film depositing, UV exposure, developing, etching, and photoresist striping; CF fabrication needs at least four sequences of masks to form BM, R, G and B. Two prepared substrates have to be treated individually by polyimide (PI) with textile buffed for LC alignment before assembling them. After that, the spacers are sprayed on TFT

substrate to sustain the cell gap and sealant is dispensed on CF for cell assembling. Then, the assembled empty cell is filled in LCs and attached polarizers. Finally, the external ICs and Flexible Printed Circuit (FPC) are bonded to complete an LCD device [47].
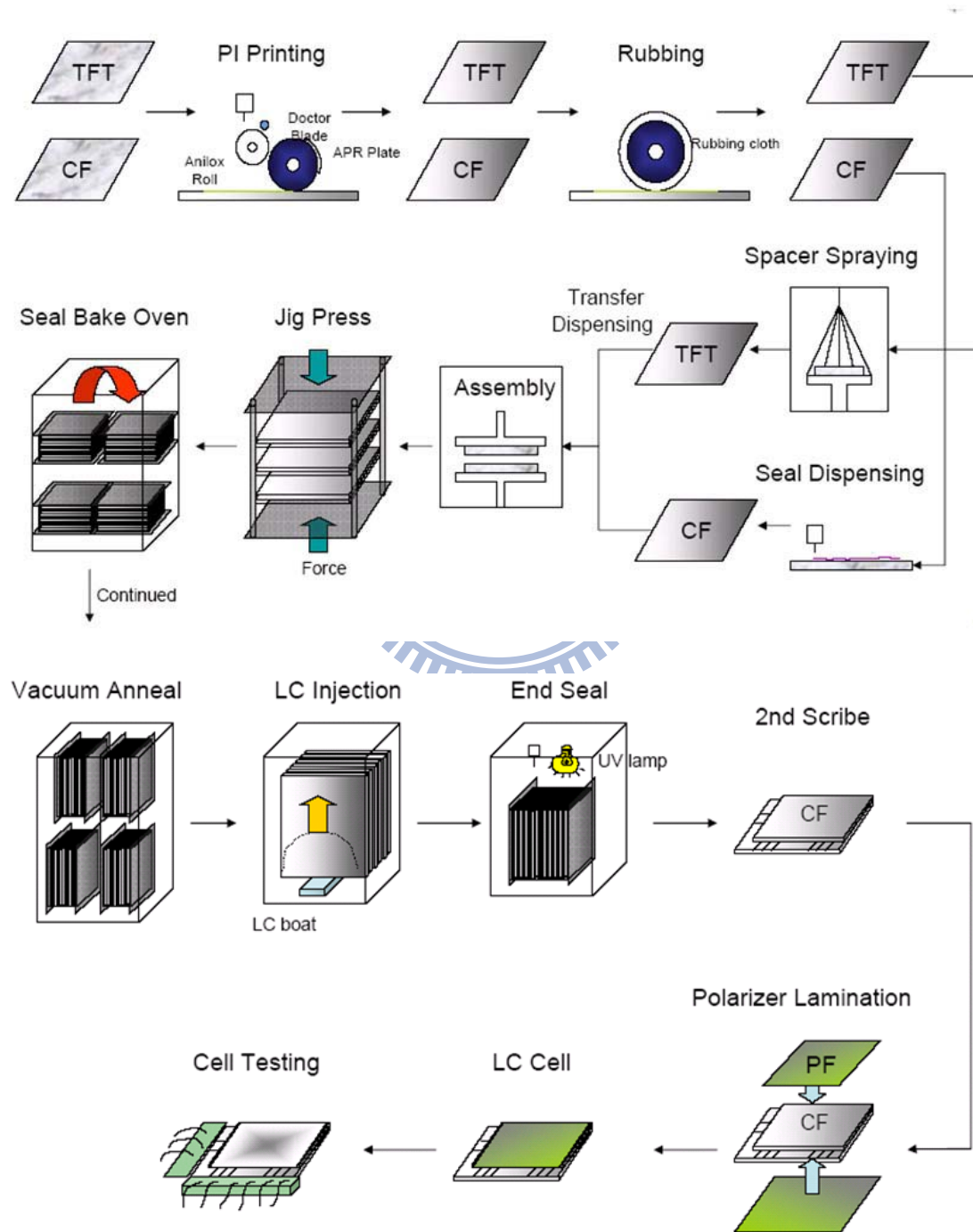
Fig.3-1 Standard LCD Fabrication [47].

3.2 Measurement Instruments

3.2.1 Laser Optical System

The laser optical system shown in Fig.3-2 was used to measure the electro-optic characteristics of the LC cells. The major measurements include Voltage versus Transmittance, retardations, and response time.

We set three lasers for R, G and B whose wavelengths are 632.8, 532 and 473nm, respectively as the measuring light sources. After putting the LC cell between polarizer and analyzer, the laser light passes through 10% ND filter first to degrade the intensity into an acceptable range for photo-detector; then the laser travels through the polarizer, cell, analyzer, and finally to the photo-detector. When the laser light passes through the LC cell, the light is modulated with the phase change of $2\pi\Delta nd/\lambda$ which changes the light intensity received by the photo-detector.

The LC cell is driven by WFG500 (company: FLC Electronics AB), which is a multi-channel high voltage waveform generator whose maximum output voltage range is ±100V and the minimum designable pulse width is 200ns, connected with PC through GPIB interface. The driving waveform applied to the cell is 1k Hz square wave for the voltage versus transmittance measurement. The photo-detector PIN20 (company: FLC Electronics AB) detects and transforms the output light intensity from analyzer with response more than 40ns into voltage. Then, the oscilloscope (company: Tektronix) and the multi-muter (company: Keithley) exhibit and transfer the output signals to the PC.

When measuring the retardations of the cell, a compensator (Soleil-Babinet, From Special Optics, Model: 8-400-UNCOATED) is positioned in between polarizer

and analyzer, illustrated as Fig.3-2. First, to rotate the compensator and record the two minimum signals detected by photo-detector, denote the two signals as min.1 and min.2 without inserting the LC cell.
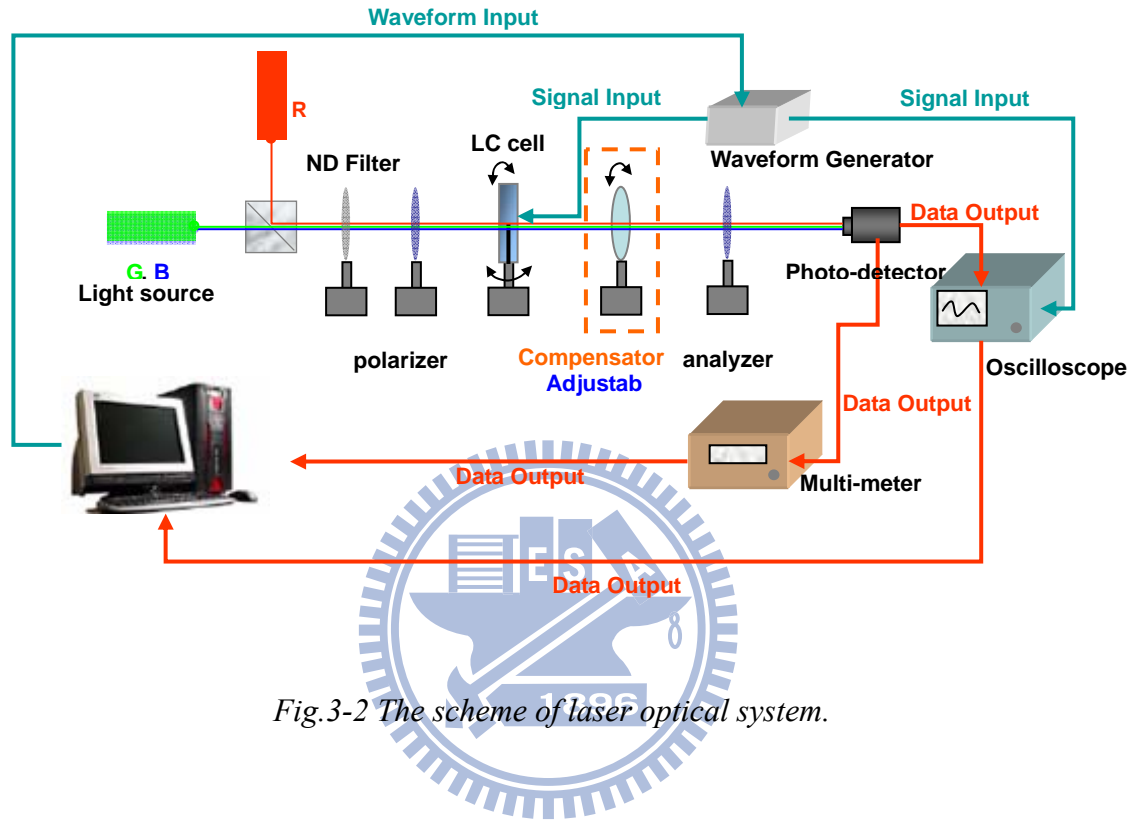
Fig.3-2 The scheme of laser optical system.

After the cell positioning between polarizer and compensator, we have to rotate the compensator and record the minimum signal denoted as x. The retardation angle is calculated by Eq. (3-1).

$$Retardation\ Angle = \Gamma = \left(\frac{x - min.2}{min.1 - min.2} \right) * 360 \qquad (3\text{-}1)$$

Following the result calculated by Eq. (3-1), the retardation value is derived as Eq. (3-2).

$$Retardation\ Value = \Delta nd = \Gamma * \frac{\lambda}{360} \qquad (3\text{-}2)$$

3.2.2 Conoscope System

The conoscopic instrument (Autronics-Melchers GmbH) is used for measuring the optical properties of brightness and contrast ratio at different angles [48-51]. The conoscopic system has diffusive and collimated illuminations. Also, a plane detector consisting of various directional charge-coupled-device (CCD) sensors is used to detect the transmissive and reflective lights. This CCD is able to measure the luminance, contrast, and color of the imaging devices simultaneously. The schematic diagram of the measurement setup is shown in Fig. 3-3. Each light beam emitted from the test area with an incident angle θ will be focused on the focal plane at the same azimuth (i.e. the same position on the captured image). The angular characteristics of the sample are thus measured simply and quickly without any mechanical movement.

Experimentally, the measurement of conoscopy is executed as follows: First, the illuminant or LCD backlight is transmitted by the sample. Second, the light with the same inclination propagates in parallel to enter the lens system. Third, the parallel rays are converged to a detector. Finally an iso-contrast contour is formed and stored by a data processor.

Source: http://www.autronic-melchers.com/.
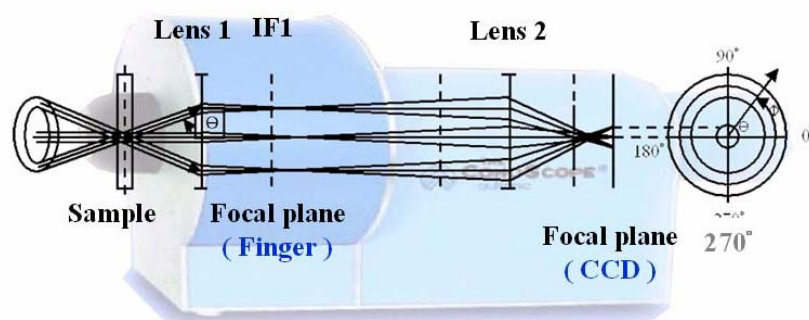
Fig. 3-3 The schematic diagram of the measurement setup of conoscope system [48-51].

3.2.3 Cell Gap Measurement -UV/Vis spectrometer LAMBDA 950

Because many optical properties of LC cells were related with cell gaps, the cell gaps had to be confirmed for analysis. Before filling liquid crystal in empty test cells, it was necessary to use UV/Vis spectrometer LAMBDA 950 (Perkin Elmer) whose spectrum resolution is $\leqq$ 0.17 nm from 175nm to 900nm, shown in Fig. 3-4, to confirm the cell gaps by interference method [52].

Based on interference method, there are two reflective surfaces included; the illustration is shown in Fig. 3-5. To define the coefficients of reflection R1 and R2 as the ratios of the incident light reflected by the surface 1 and surface 2 respectively. To assume the total incident light is $I=cos\,(\omega t)$ without absorption on the surface 1 and 2. The total reflected light intensity R is,

$$R = R1\cos\varpi t + \sum_{k=1}^{\infty} R1^{k-1} R2^{k}(1-R1)^{k+1}\cos\varpi(t-kt_0),$$

$$\text{where } \varpi = 2\pi c n_{Gap}^{1/2}/\lambda \text{ and } t_0 = 2d_{Gap}n_{Gap}^{1/2}/c \tag{3-3}$$

where c denotes light speed in vacuum; l means wavelength of incident light; n_{Gap} and d_{Gap} denote the index of refraction and thickness of the layer, respectively. The factor k>1 means internal reflections which can be neglected, because the reflections are too small. Therefore, the total reflection is as following.

$$R = R1\cos\varpi t + R2(1-R1)^2\cos\left(\varpi t - \frac{4\pi n_{Gap}d_{Gap}}{\lambda}\right) \tag{3-4}$$

Thus the reflected spectrum is,

$$|R(\lambda)|^2 = R1^2 + \left[R2(1-R1)^2\right]^2 + 2R1R2(1-R1)^2\cos\left(\frac{4\pi n_{Gap}d_{Gap}}{\lambda}\right), \text{when } t = 0. \tag{3-5}$$

The reflected interference spectrum determines the optical thickness of the cell, i.e.

$n_{Gap} \cdot d_{Gap}$. For instance, the λ_1 and λ_2 are two wavelengths yielding the extreme values in Eq. (3-5). Thus,

$$\cos\left(\frac{4\pi n_{Gap} d_{Gap}}{\lambda}\right) = \pm 1, \text{ with respect to } \lambda_1 \text{ and } \lambda_2,$$
$$2n_{Gap}d_{Gap} = m_1 \lambda_1 / 2 \qquad\qquad (3\text{-}6)$$
$$2n_{Gap}d_{Gap} = m_2 \lambda_2 / 2$$

where m_1 and m_2 are natural numbers. Suppose $\lambda_1 > \lambda_2$, the $m_2 = m_1 + x$, where x is also a natural number. From Eq. (3-6), the $n_{Gap} \cdot d_{Gap}$ can be derived as Eq. (3-7).

$$n_{Gap}d_{Gap} = \frac{x\lambda_1\lambda_2}{4(\lambda_1 - \lambda_2)} \qquad\qquad (3\text{-}7)$$

The value of x-1 indicates the number of extreme values in $|R(\lambda)|^2$ between the wavelengths λ_1 and λ_2. It is better to choose the x between the two extreme values as large as possible to improve the accuracy of the calculation of $n_{Gap} \cdot d_{Gap}$. A measuring result of a test cell is shown in Fig. 3-6. From the figure, the chosen wavelengths are $\lambda_1 = 786$nm and $\lambda_2 = 494$nm, the $x = 12$, and the cell gap of the test cell can be calculated as following.

$$n_{Gap}d_{Gap} = \frac{x\lambda_1\lambda_2}{4(\lambda_1 - \lambda_2)} = \frac{12 \times 786 \times 494}{4(786 - 494)} = 3.98\mu m, \text{ where } n_{Gap} = 1.$$

Fig. 3-4 UV/Vis spectrometer LAMBDA 950 produced by Perkin Elmer.
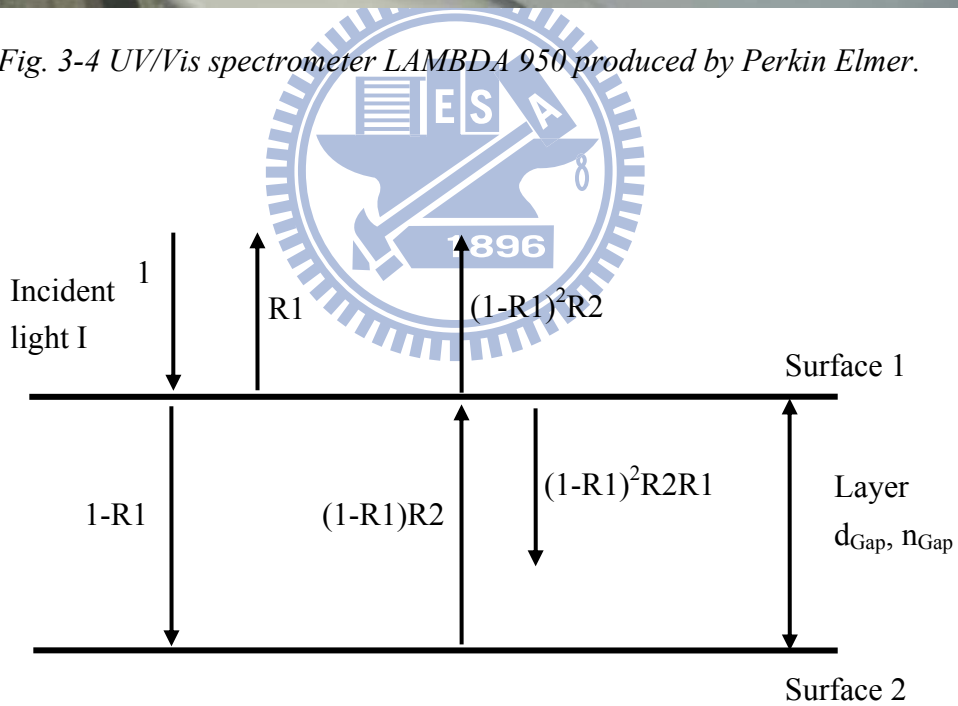
Fig. 3-5 The light pass through surface 1 and 2 whose reflective coefficients denoted as R1 and R2 causes interference.
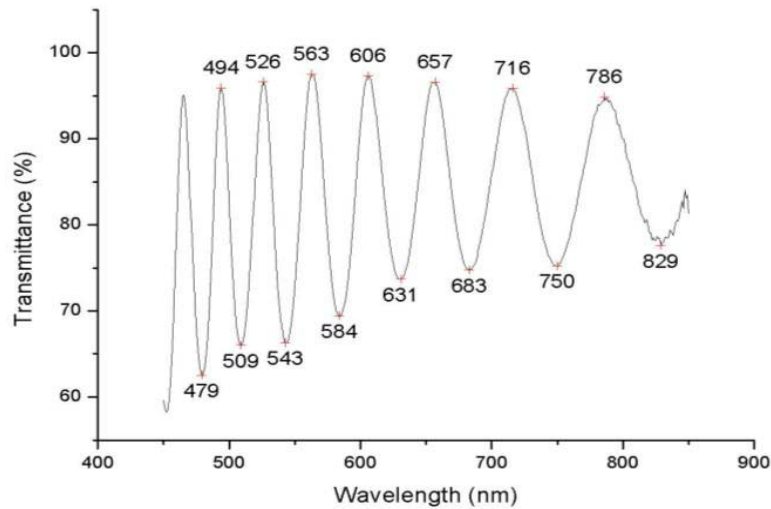
Fig. 3-6 The measured spectrum of a test cell.

3.2.4 AFM (Atomic Force Microscope)

The atomic force microscope (AFM) consists of a flexible micro-scale cantilever with a scanning sharp tip at its end that is used to scan the specimen surface, and use feedback mechanisms that enable the piezoelectric scanners to maintain the tip at a constant force. The cantilever is typically made of silicon or silicon nitride to form a curvature with a tip whose end radius is 2 nm to 20 nm, depending on tip type. When the tip approaches a sample surface, the atomic forces, include van der waals forces, electrostatic forces and magnetic forces…etc., between the tip and the sample lead to a deflection of the cantilever based on Hooke's law. Typically, the deflection is measured by using a laser spot reflected from the top of the cantilever into an array of photodiodes.

The scanning motion is conducted by a piezoelectric tube scanner which scans the tip in a raster pattern with respect to the sample (or scans the sample with respect to the tip). The interaction between tip and sample is monitored by reflecting the laser light from the cantilever into a split photodiode detector. By detecting the difference

of the photodetector output voltages, the changes of the cantilever deflection and the oscillation amplitude are determined. The schematic diagram of this mechanism is depicted in Fig. 3-7.
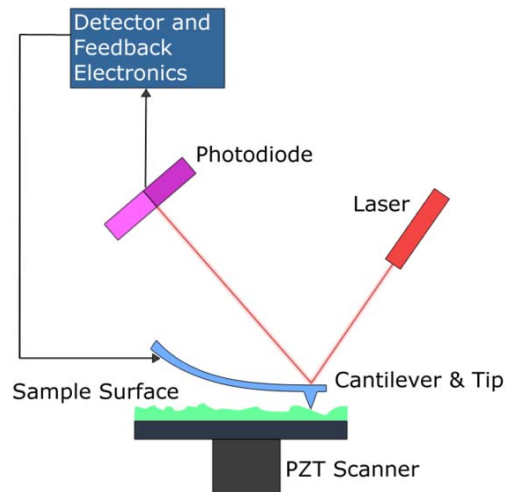
Fig. 3-7 Block Diagram of Atomic Force Microscope.

There are three operation modes: contact mode, non-contact mode, and tapping mode, in AFM system. In the studies, we use contact mode for the thickness measurement of a RM film and tapping mode for scanning the surface morphology of the nanostructure on a substrate.

Chapter 4

Investigation of Transition Effect in a Nanostructure Enhanced Pi-cell

It is well-known that a Pi-cell must be operated in bend state transited from splay state. Before starting state transition, the nucleation must occur uniformly to the whole active area in a Pi-cell. In this study, *Nanostructure Enhanced Pi-cell* (*NE-Pi-cell*) was proposed. Not only the random distribution of silicon oxide nano-particles was investigated for decreasing the transition time but also the limitation of increasing nano-particle density. The reduction rates of splay-to-bend and twist-to-splay transition time were over **99.9%** with nanostructure surfaces. However, the response time and V-T curve remained the same as un-treated Pi-cell.

4.1 Introduction

The Pi-cell [31], also coined as *Optically Compensated Bend* (*OCB*) mode liquid crystal cell [53], possesses the advantage of the fast response time of less than 3 ms. This is due to the lack of backflow during molecular relaxation [32-36] in its bend state. The Pi-cell, however, has five distinct states in its transitions, illustrated in Fig. 4-1. There are (1) the splay ground state (H), (2) the symmetric splay state (Hs), (3) the asymmetric splay state (Ha), (4) the bend state, and (5) the 180° twist state [37-39]. The lowest free energy state is splay state without applying voltage. When we applied

a voltage higher than the first critical voltage V_{C1} (around 1 Vrms), Hs state would be formed under the same surface condition on both sides of a Pi-cell. The Hs state, then, quickly turned into asymmetric Ha state. As the applied voltage was further increased beyond the second critical voltage V_{C2} (around 2 Vrms), also called the critical voltage, denoted Vcr, of a Pi-cell, the bend state became the stable state. Nucleation was required to achieve the uniform bend state from splay state. The splay-to-bend transition process usually took from few seconds to minutes to complete, depending on different applied voltage. When the voltage was dropped below V_{C2}, the LCs would first relax to the twist state and further nucleate into the splay ground state.
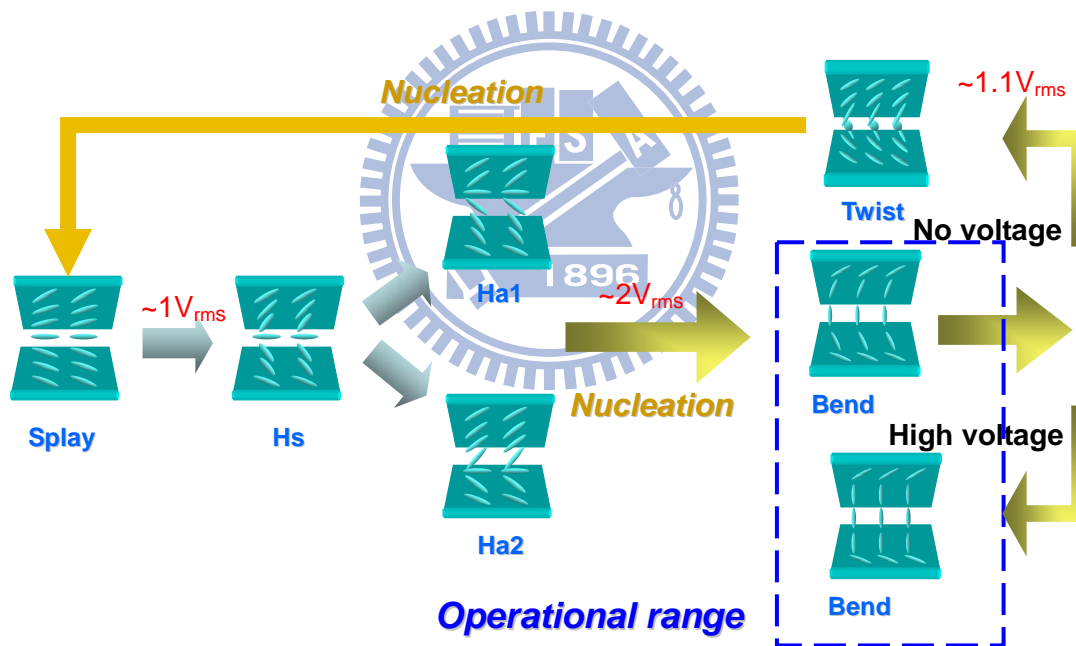
Fig. 4-1 Schematic of five distinct transitions in Pi-cell.

Many nucleation enhancement techniques had been proposed to induce splay to bend transition and reduce the transition time. The simplest method was to apply a high voltage pulse (~20V) to induce the bend state formation [54-55]. However, the

method is not suitable for all TFT-driving devices. Other methods can be categorized into chiral and non-chiral doped LC systems. For the chiral doping LC system, chiral molecules were utilized to stabilize a 180° twist configuration to eliminate the required bend nucleation [56-57]. Further enhancement of technique with slits and protrusions on the substrates can be seen in *Dual-Domain Bend* Mode (DDB Mode) LC devices [58]. On the other hand, the non-chiral doping system laid stress on creating bend transition cores to reduce transition time in a Pi-cell [59-60]. Bend transition cores can be generated by defects and structures such as spacers [61], high surface pre-tilt angles [13], polymer-stabilized bend configuration [26][62], and multi-domain alignment [24][63-64] for example.

These techniques successfully emphasized the inducing bend transition cores but degraded the contrast ratio of devices. In this study, we proposed the *Nanostructure Enhanced Pi-cell* (*NE-Pi-cell*) to reduce the splay-to-bend transition time from 2 minutes to almost none under 6V. Moreover, we focused on the study of the relationship between transition time and nano-particle protrusion density in hetero-nucleation. The limitation of increasing nano-particle density will also be investigated. Also, the fabrication process was compatible to the conventional TN- or Pi-cell process.

4.2 The proposed Novel Nanostructure Enhanced Pi-cell

4.2.1 The cell structure of a *NE-Pi-cell*

In order to enhance the transition rate, we proposed a novel Pi-cell, named by *Nanostructure Enhanced Pi-cell* (*NE-Pi-cell*), which possesses nanostructure layers

on both side of the cell boundaries. The cross section diagram of a *NE-Pi-cell* is illustrated in Fig. 4-2.
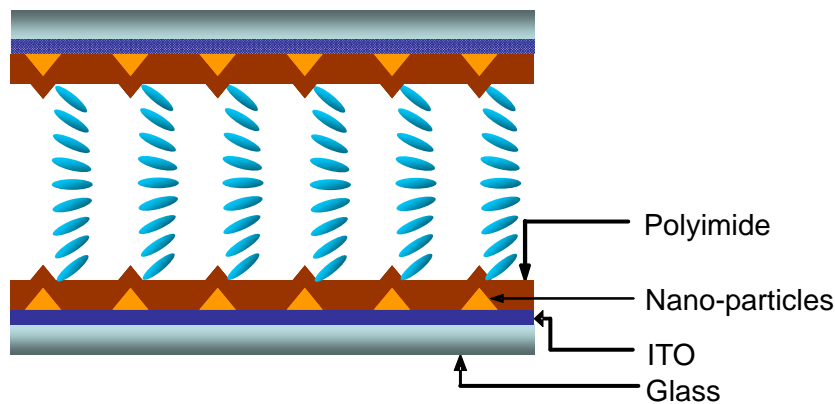
Fig. 4-2 The cell structure of a NE-Pi-cell.

In the novel *NE-Pi-cell*, the nanostructures are coated on the ITO glass substrates before PI coating, which differs from prior art by mixing the nano-particles with PI solution. Therefore, the nano-particles can be covered with a PI layer completely, and the anchoring energy between PI and LC molecules will not be changed. Based on this concept, the critical voltage will remain unchanged. The mechanism of nanostructure-enhanced transition rate can be confined in heterogeneous nucleation. Since the cell structure is purified, the discussion will focus on the effects and limitations caused by densities, distribution and dimensions of nano-particles [41][65].

4.2.2 The Fabrication of the *NE-Pi-cells*

The general empty liquid crystal cells were fabricated by two polyimide treated 2.0cm × 2.5cm indium-tin-oxide (ITO) glass substrates. The polyimide (Chisso, PIA-X201-G01) was baked at 220 °C before rubbing. The cell gaps were controlled

by 3 and 5 μm spacers individually. Nematic liquid crystal (Chisso ZCE-5096) was filled by capillary attraction. In the *NE-Pi-cell* fabrication, the nano-particles (Everlight Chemical Industrial Co., 90&50nm) had to be coated on the ITO substrates before polyimide (PI) treatment. After finishing the PI process, the nano-particle modified substrates were assembled for LC cell as the general procedure. The *NE-Pi-cell* fabrication processes are illustrated in Fig. 4-3.
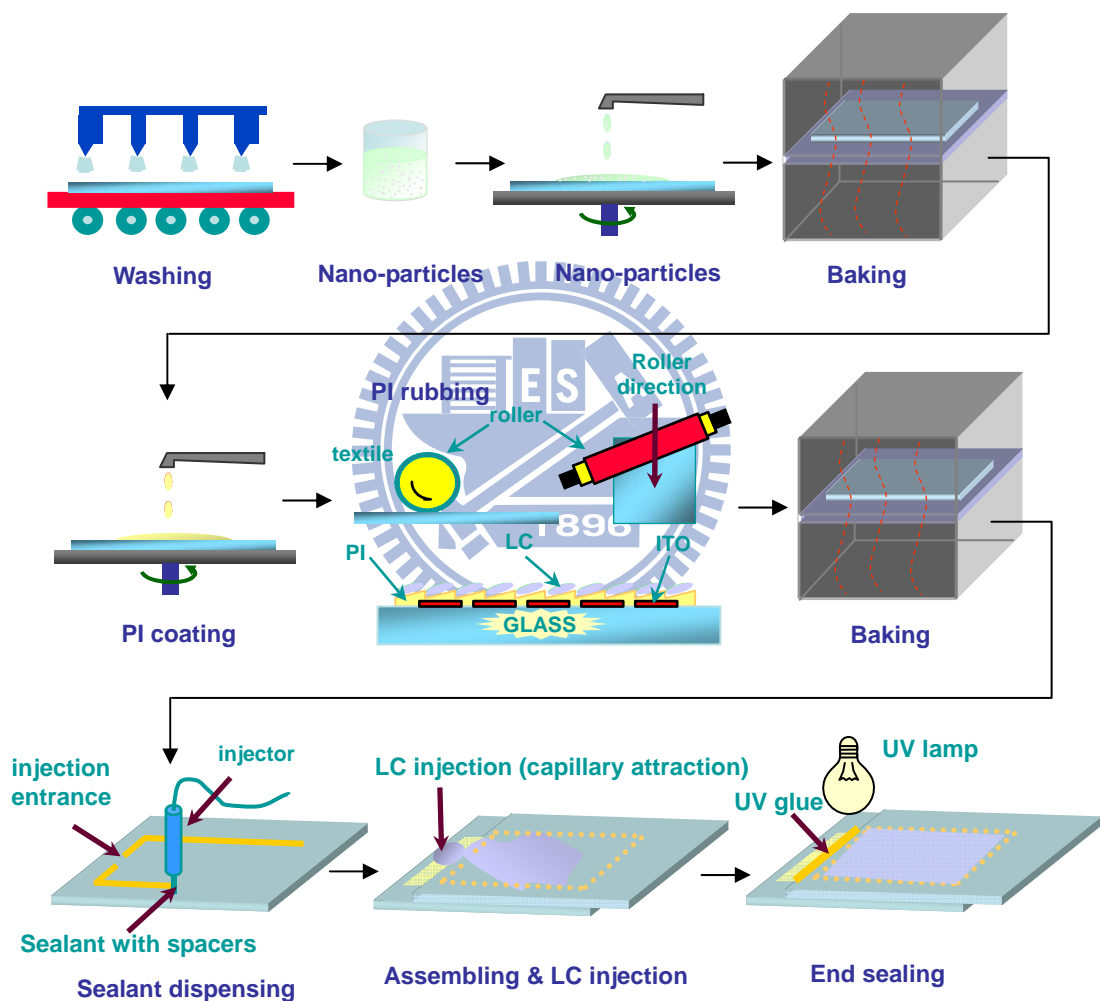
Fig. 4-3 NE-Pi-cell fabrication processes in laboratory.

The nano-particle modified surface was prepared before polyimide layer. In order to investigate the nanostructure enhanced effects, the high density, uniform

distribution nanostructure substrates have to be fabricated well. However, the aggregation of nano-particles is always an issue in fabrication when the nano-particle density increases. Therefore, two main methods have been accepted here to solve the issue. Method 1: Silicon oxide (SiO_2) nano-particle aqueous solution was diluted with de-ionic (DI) water and coated directly on the substrates. The density was limited and saturated by the fabrication in Method 1; even the nano-particle solution was coated twice. The aggregation issue became serious when the concentration of nano-particles was over 0.2 wt%. Since the aggregation issue needed to be improved in high nano-particle density, the method 2 was proposed. Method 2: Silicon oxide (SiO_2) nano-particle aqueous solution was also diluted with de-ionic (DI) water, but then mixed with a solvent, composed of 90 wt% EG and 10 wt% PGMEA, and coated on the substrate. The process conditions are shown in Tabs. 4-1 and 4-2 with respect to Method 1 and 2.

In processes, the first step is DI water coating (i.e. wetting process) for increasing nano-particle's adhesion with glass substrate. In Method 1, shown in Tab. 4-1, the 3rd spin of step 2 needed high spin speed, because the nano-particles, dispersed in DI water, are easy to aggregate during the coating process. Therefore, raising nano-particle density is difficult, even when coating twice. In Method 2, the nano-particles dispersed in EG/ PGMEA solvent instead of DI water which improved the aggregation issue and necessary high coating spin speed. However, the spin time in Method 2 needs to be shortend since the EG/ PGMEA solvent evaporates quickly and shrinks easily. Moreover, the hard baking temperature has to be higher than the boiling point of EG/ PGMEA to make sure of quick evaporation without leaving residue. Otherwise, the residual EG/PGMEA will contaminate the alignment function of PI and affect the cell properties.

Tab. 4-1 The process condition of SiO$_2$ nano-particle aqueous solution.

Method 1		
Step 1: DI water coating (wetting)		
	Spin (rpm)	Time(sec)
1st spin	500	10
2nd spin	5000	60
Step 2: nano-particle aqueous solution coating		
	Spin (rpm)	Time(sec)
1st spin	0	60
2nd spin	500	10
3rd spin	**5000**	60
Step 3: Baking 110°C x 30min		

Tab. 4-2 The process condition of SiO$_2$ nano-particles + EG/PGMEA solvent.

Method 2		
Step 1: DI water coating (wetting)		
	Spin (rpm)	Time(sec)
1st spin	500	10
2nd spin	5000	30
Step 2: nano-particles mixed with EG/PGMEA solvent		
	Spin (rpm)	Time(sec)
1st spin	0	**30**
2nd spin	500	10
3rd spin	1500	**30**
Step 3: Baking 250°C x 30min		

4.3 Nano-particle Density Investigation

In our experiments mentioned above, we used two different dimensions of nano-particles (mean diameter: 50 & 90 nm) to create protrusions in proposed *NE-Pi-cells*. The distribution of the nano-particles on the ITO glass was measured by AFM. The diameters of the protrusions were found in the region of 200-300 nm, with

the height of 150-270 nm after PI coating with respect to 0.2 wt% 50 nm and 90 nm nano-particles. The AFM photos of 0.2 wt% nano-particle (90nm) distributions, fabricated by Method 1 & 2 are shown in Figs. 4-4 and 4-5 respectively. As the results, the aggregations were improved greatly and the particle density was also increased from 6.78 to $11.6 \mu m^{-2}$ by using Method 2, shown in Fig. 4-6. Some aggregations of SiO_2 particles were still found when the concentration was higher than 0.2 wt%; not only 90 nm but also 50nm nano-particle distribution shown in Fig. 4-7. Thus, the concentration of nano-particles must be confined to no more than 0.2wt% in the process of *NE-Pi-cells*. The other AFM photos of 50 and 90 nm nano-particles fabricated in different concentrations are shown in Figs. A-1, A-2 ~ A-8 (Appendix A).
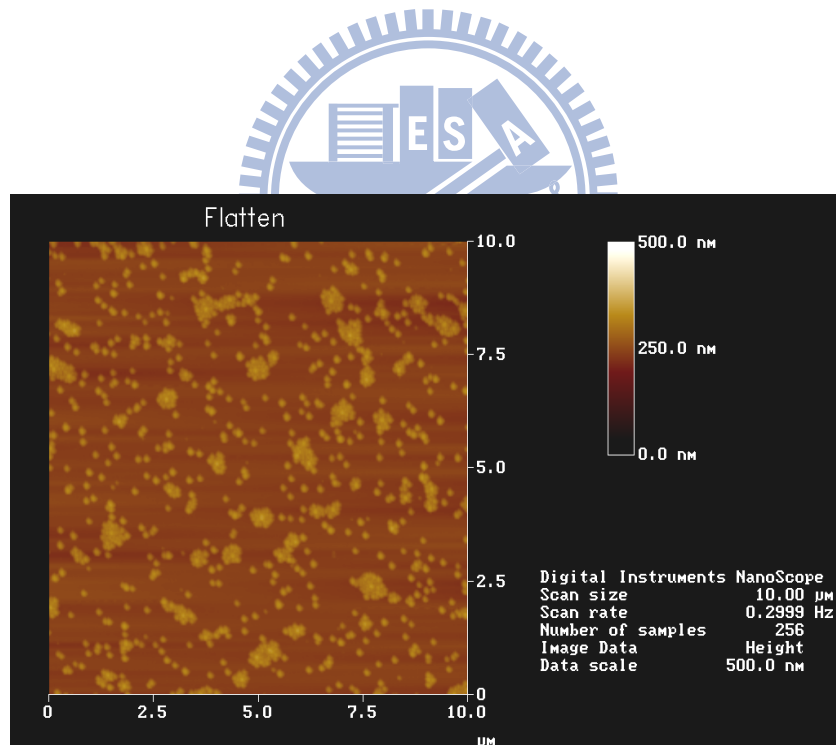
Fig. 4-4 0.2wt% 90nm nano-particles are coated twice by Method 1, the particle density is about $6.78 \mu m^{-2}$. The aggregations are serious.
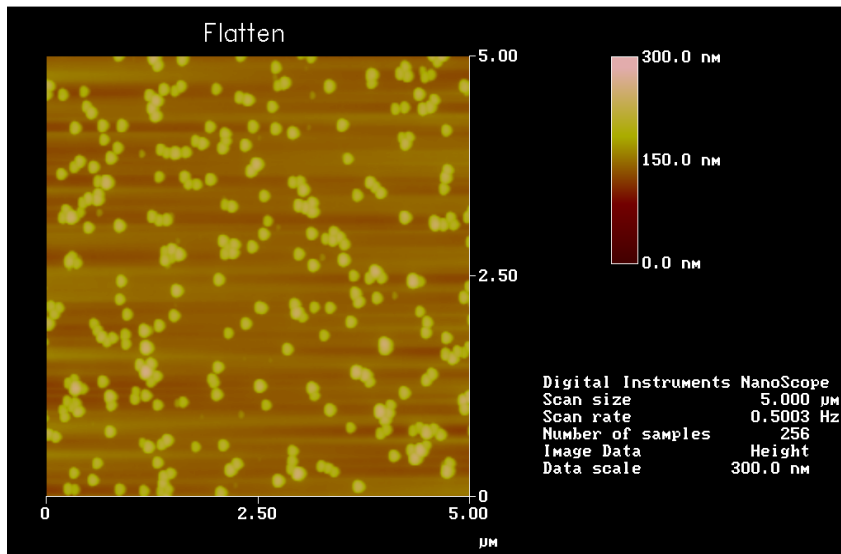
Fig. 4-5 0.2wt% 90nm nano-particles are coated by Method 2, the particle density is about 11.6μm^{-2}. The aggregation issue is improved greatly.
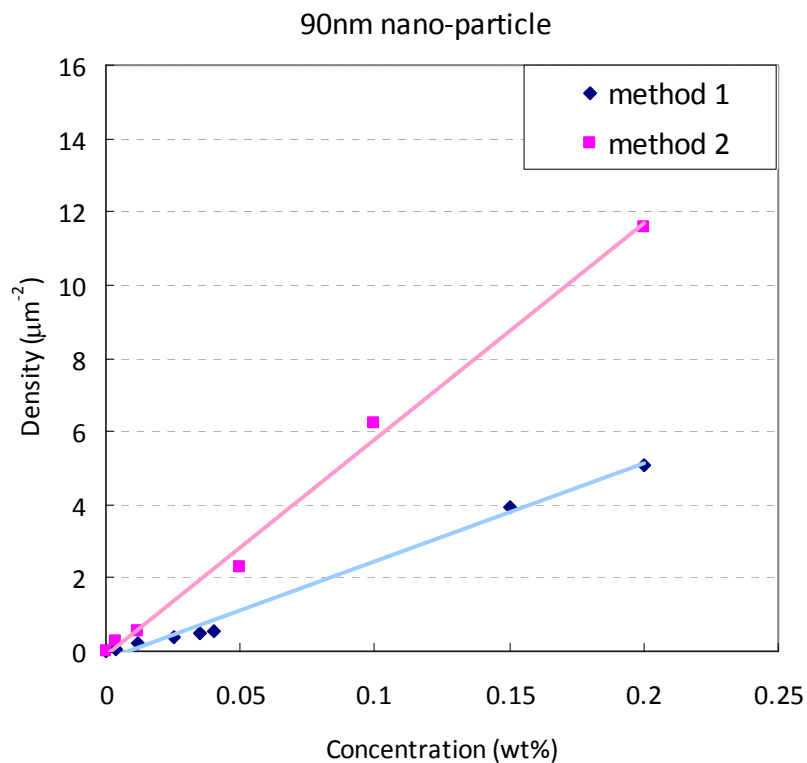
Fig.4-6 Concentration (wt%) v.s. Density(μm^{-2}) of 90nm nano-particles fabricated by Method 1 and 2, respectively. The density can be increased from 6.78 to 11.6 μm^{-2}.
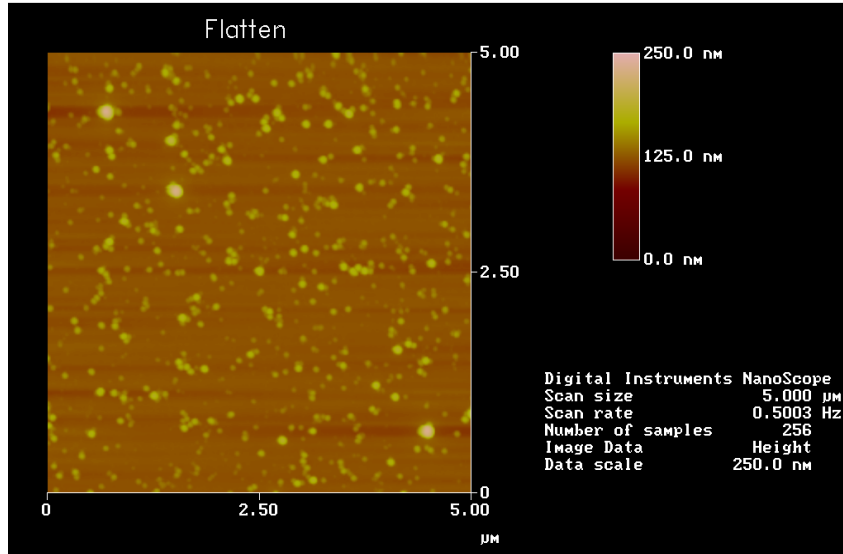
Fig. 4-7 0.2wt% 50nm nano-particles are coated by Method 2. Some aggregations were still found when the concentration is over 0.2wt%.

In order to investigate densities of different dimensions of nano-particles, we proposed a specific metric "*protrusion volume ratio*," which was the total volume of protrusions covered with PI layer in a maximum affected volume. The maximum affected volume was defined by maximum nano-particle size coated on the surface, to unify the densities of different nano-particle sizes (Maximum size of 90nm was used in the experiment). The *protrusion volume ratio* whose physical meaning was similar to protrusion density was defined as following Eq. (4-1). The illustration is shown in Fig. 4-8. In the experiments, the maximum nano-particle size and highest protrusion covered with PI are 90nm and 103.5nm, respectively.

Protrusion volume ratio (%)

$$= \frac{\text{total volume of protrusions covered with PI on the surface}}{\text{Max. affected volume (defined by max. nano - particle size using in the study)}}$$

$$= \frac{\frac{\pi}{6}\left[3r^3(1-\cos\theta)-2a^2(r-h)\right]}{5\mu m \times 5\mu m \times \text{Max. protrusion diameter}} \quad \text{, where} \quad r = \frac{a^2+h^2}{2h} \tag{4-1}$$
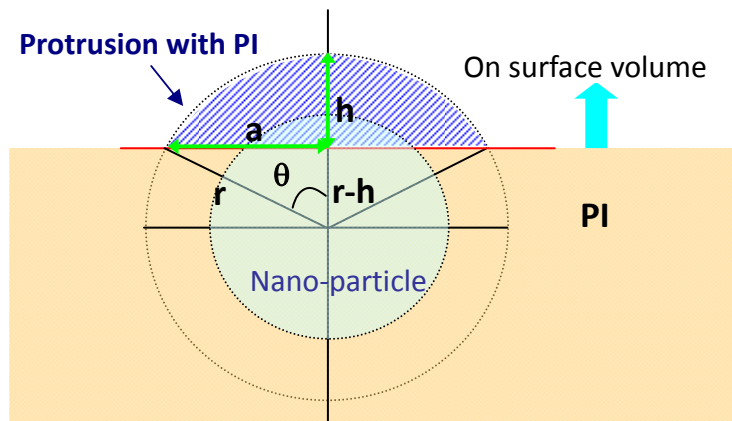
Fig. 4-8 The illustration of calculated volume of a nano-particle covered with PI on the surface.

By using the novel metric, the unified parameter for different nano-particle sizes can be achieved. It's useful for the investigation between transition rate and nano-particle enhanced effect. The relationship between concentration (wt%) and *protrusion volume ratio* of the nano-particle was investigated in Fig. 4-9. The average *protrusion volume ratios* of the nano-particles possess linear relationship with the concentration of SiO_2 solution.
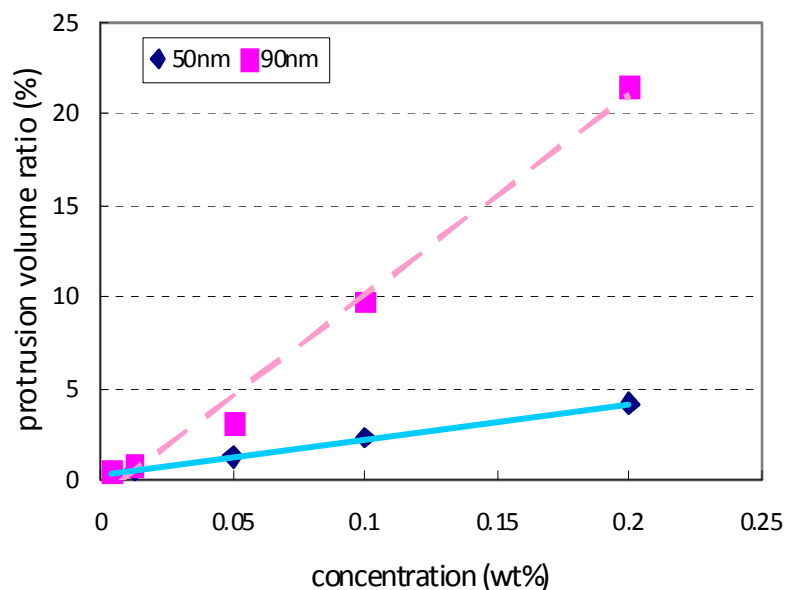
Fig. 4-9 Concentration (wt%) v.s. protrusion volume ratios of the nano-particles.

4.4 Transition Time v.s. Nano-particle Density

In order to observe the transition time by video camera, the 6V AC square wave was applied on test cells. As shown in Fig. 4-10, the nucleation process of 5μm *NE-Pi-cell* can be clearly identified. In Fig. 4-10 (b) and (d), there are two nucleation processes; one is elevated splay stay, also known as asymmetry splay state, transits to bend state (Vapp > Vcr) and another one is twist state relaxes to ground splay state (Vapp = 0), respectively.
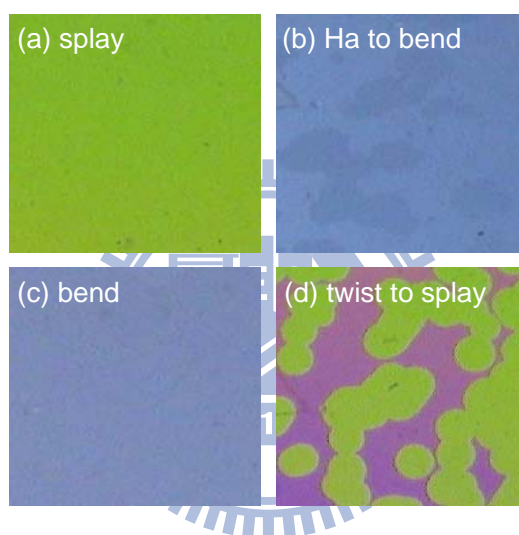
Fig. 4-10 Nucleation process of a 5 μm NE-Pi-cell. (a) Splay state, (b) Ha-to-Bend state, (c) Bend state, and (d) Twist-to-Splay state.

The transition times of splay-to-bend and twist-to-splay states can be calculated from captured video clips and the results of 3 and 5μm cells with different *protrusion volume ratios* were investigated in Fig. 4-11 (a) and (b) respectively. In ~5μm *NE-Pi-cell*, the both transition time of splay-to-bend and the twist-to-splay states were improved from 141 and 228sec to almost 0 and could not be measured, when the *protrusion volume ratio* was over 3%. The transition time was also related with the cell gap, so the ~3μm cell transited faster than the 5μm cell. As the results, the higher *protrusion volume ratios* of the nano-particles, the less transition times of the

splay-to-bend and twist-to-splay states. The fitting curves of transition time were calculated by exponential functions (correlation coefficients R^2 were about 90%), which were matched with the nucleation theory.

(a)

(b)
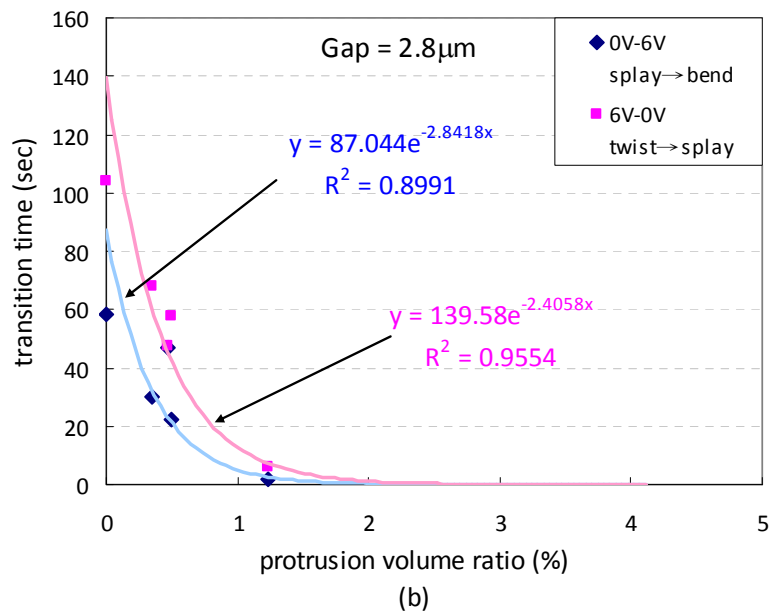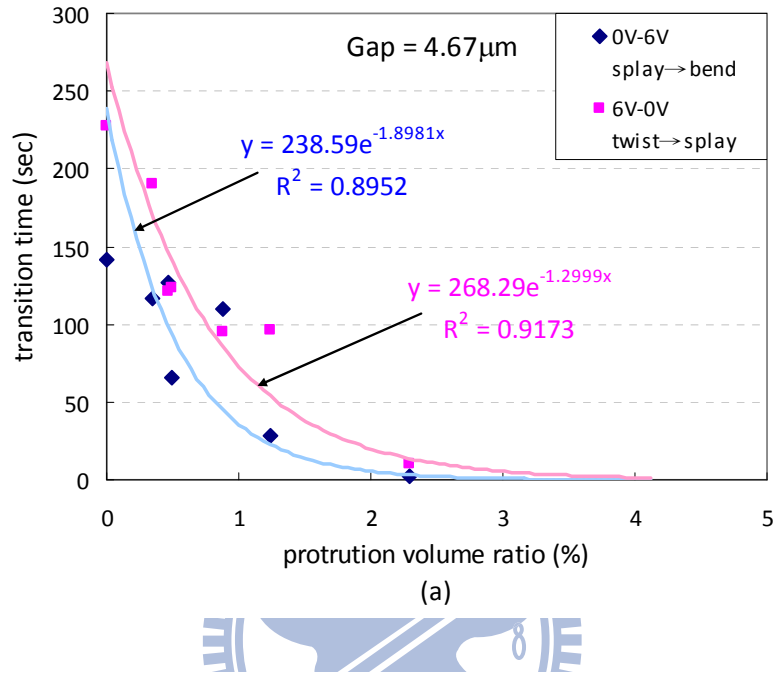
Fig. 4-11 The relationship between protrusion volume ratios and transition times of (a) 5μm cells (gap_ave. = 4.67μm), and (b) 3μm cells (gap_ave. = 2.8μm).

Furthermore, as the *protrusion volume ratio* was over ~3% and (concentration $\geqq$ 0.1wt %), the response time of the *NE-Pi-cells* were raised from ~3 to ~13ms and ~1.5 to ~6ms with respect to 5 and 3μm cells, no matter nano-particles of 50nm or 90nm. The concentration limitation implied the protrusion quantities affect the potential nucleation sites. According to the detail investigation, we found the protrusion density was also limited under 4.2μm^{-2}. The protrusion density raise meant the potential nucleation sites were increased. If the protrusion density was over the limitation, the morphology of alignment layers were affected, and the LC directors could not be arranged quickly toward the same direction when applied voltage was released. In other words, the raises of *protrusion volume ratio* and protrusion density were limited by the response time. Anyway, the levels of the response time of *NE-Pi-cells* were not related with nano-particle sizes but related with their cell gaps significantly. The detail data of response time and protrusion densities for 50 nm and 90nm nano-particle are summarized in Tabs. 4-3 (a), (b), Tabs. 4-4 (a) and (b) individually. Then, the response time of ~5μm NE-Pi-cells coated by nano-particles of 50 and 90nm with different nano-particle concentrations and protrusion densities are shown in Figs. 4-12 and 4-13 respectively.

Tab. 4-3(a) The response time of ~5μm cells coated by 50nm nano-particles.

Concentration (wt%) 50nm	Protrusion volume ratio (%)	Protrusion density (μm^{-2})	cell gap (μm)	rise time 8→2V (T-10%→T-90%)	fall time 2→8V (T-90%→T-10%)	RT(ms)
no nano-particle	0	0	4.89	3.22	0.2102	3.43
0.004	0.35	1.9	4.72	3.2	3.35E-04	3.20
0.0125	0.49	2.8	4.54	3.25	2.69E-04	3.25
0.05	1.24	4.2	4.68	2.98	3.03E-04	2.98
0.1	2.30	11.2	4.35	13.8	3.45E-04	13.80
0.2	4.11	17.7	4.41	14	2.57E-04	14.00

Tab. 4-3(b) The response time of ~3μm cells coated by 50nm nano-particles.

Concentration (wt%) 50nm	Protrusion volume ratio (%)	Protrusion density (μm^{-2})	cell gap (um)	rise time 8→2V (T-10%→T-90%)	fall time 2→8V (T-90%→T-10%)	RT(ms)
no nano-particle	0	0	3.21	1.677	0.09378	1.77
0.004	0.35	1.9	2.8	1.30E+00	2.34E-04	1.30
0.0125	0.49	2.8	3.03	1.5	1.64E-04	1.50
0.05	1.24	4.2	2.44	1.2	2.03E-04	1.20
0.1	2.30	11.2	2.76	5.3	2.31E-04	5.30
0.2	4.11	17.7	2.88	5.4	2.30E-04	5.40

Tab. 4-4(a) The response time of ~5μm cells coated by 90nm nano-particles.

Concentration (wt%) 90nm	Protrusion volume ratio (%)	Protrusion density (μm^{-2})	cell gap (um)	rise time 8→2V (T-10%→T-90%)	fall time 2→8V (T-90%→T-10%)	RT(ms)
no nano-particle	0	0	4.89	3.22	0.2102	3.43
0.004	0.47	0.3	4.71	3.17	0.2451	3.42
0.0125	0.88	0.6	4.81	3.54	0.1781	3.72
0.05	3.09	2.3	4.74	3.25	0.256	3.51
0.1	9.75	6.2	4.89	12.86	0.3643	13.22
0.2	21.5	11.6	4.62	12.32	0.2914	12.61

Tab. 4-4(b) The response time of ~3μm cells coated by 90nm nano-particles.

Concentration (wt%) 90nm	Protrusion volume ratio (%)	Protrusion density (μm^{-2})	cell gap (um)	rise time 8→2V (T-10%→T-90%)	fall time 2→8V (T-90%→T-10%)	RT(ms)
no nano-particle	0	0	3.21	1.677	0.09378	1.77
0.004	0.47	0.3	2.94	1.41	0.08812	1.50
0.0125	0.88	0.6	2.43	1.41	0.1194	1.53
0.05	3.09	2.3	2.83	1.085	0.1652	1.25
0.1	9.75	6.2	2.76	6.4	0.1291	6.53
0.2	21.5	11.6	2.77	6.56	0.07999	6.64
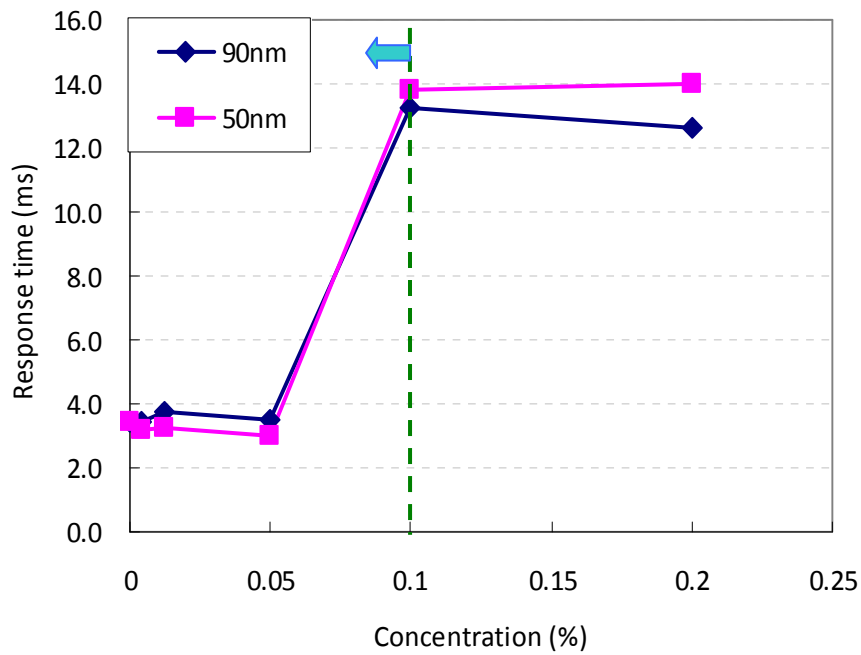
Fig. 4-12 The response time of ~5μm NE-Pi-cells coated by nano-particles of 50 and 90nm with different nano-particle concentrations.
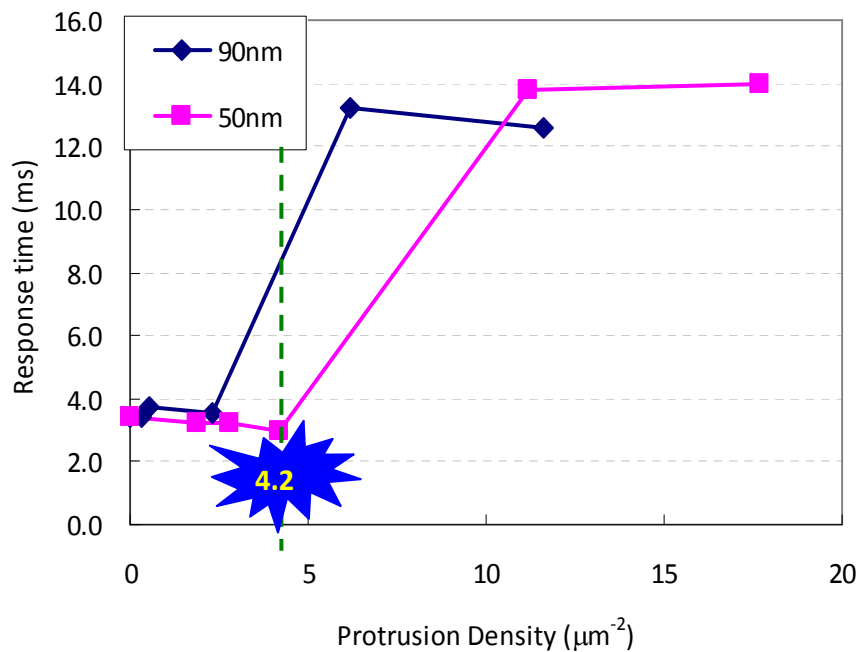
Fig. 4-13 The response time of ~5μm NE-Pi-cells coated by nano-particles of 50 and 90nm with different protrusion densities.

However, under the limitation of the protrusion density, the response time and voltage versus transmittance curves (V-T curve) of the *NE-Pi-cells* were almost the same as the conventional Pi-cell driven over the critical voltage (Vcr). And the critical voltages of *NE-Pi-cells* are only related with cell gaps and independent of nano-particle sizes. The V-T curves and critical voltages of the *NE-Pi-cells* with different nano-particle concentrations are shown in Fig. 4-14 and Fig. 4-15 with respect to 50nm and 90nm nano-particle treatments. Moreover, both transition times of splay-to-bend and twist-to-splay states had 99.9% reductions without high voltage pulse driving.

To further investigate splay-to-bend transition, there was strong negative correlation between the transition time and driving voltage. Due to the high reduction rate of transition time in a *NE-Pi-cell*, it's difficult to recognize the varieties of transition times with different *protrusion volume ratios*. In order to observe easily, the transition time needs to be measured under lower driving voltage which is just higher than the critical voltages to slow the transition rates. The results are shown in Figs. 4-16 (a) and (b) with respect to ~5μm and ~3μm cells. As the Fig. 4-16 (a), in ~5μm cells, the transition time is strong correlated with *protrusion volume ratios* by negative exponential function and the R^2 (the square of correlation coefficient), means coefficient of determination in linear regression, is over 90%. However, the R^2 is lower in ~3μm cells shown in Fig. 4-16 (b), because of larger measuring deviations of transition times and worse cell uniformities for the cells with low cell gaps.

50nm--gap=3μm

(a)

50nm--gap=5μm

(b)
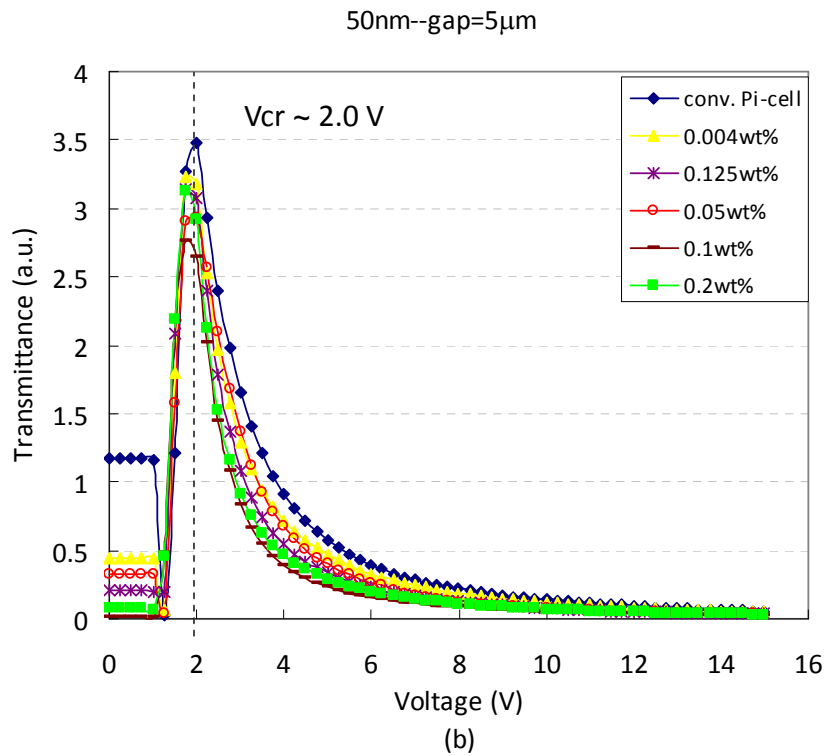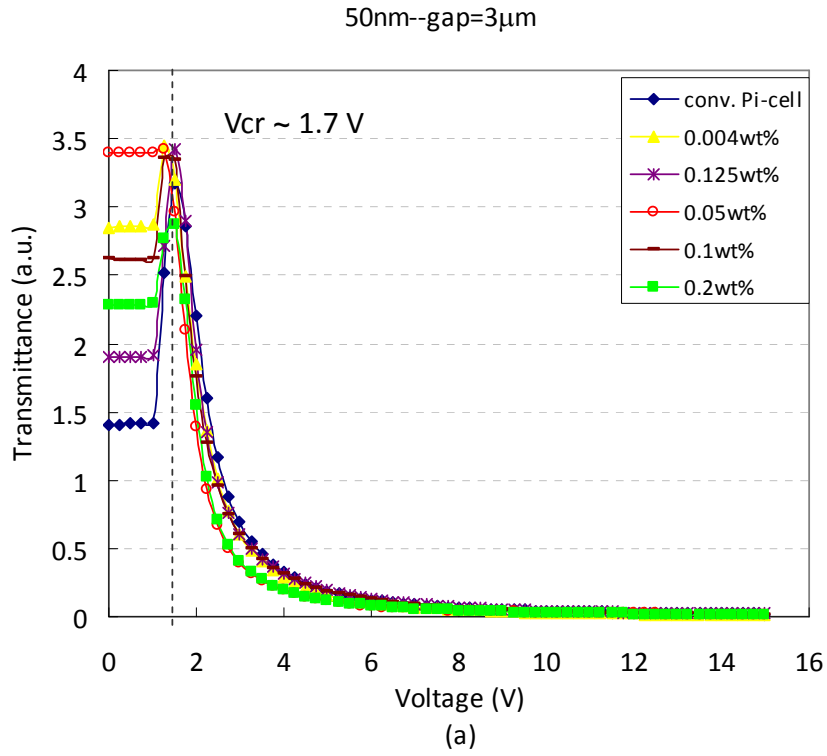
Fig. 4-14 The V-T curves of different nano-particle (50nm) concentrations with respect to (a) 3μm cell gap, and (b) 5μm cell gap.
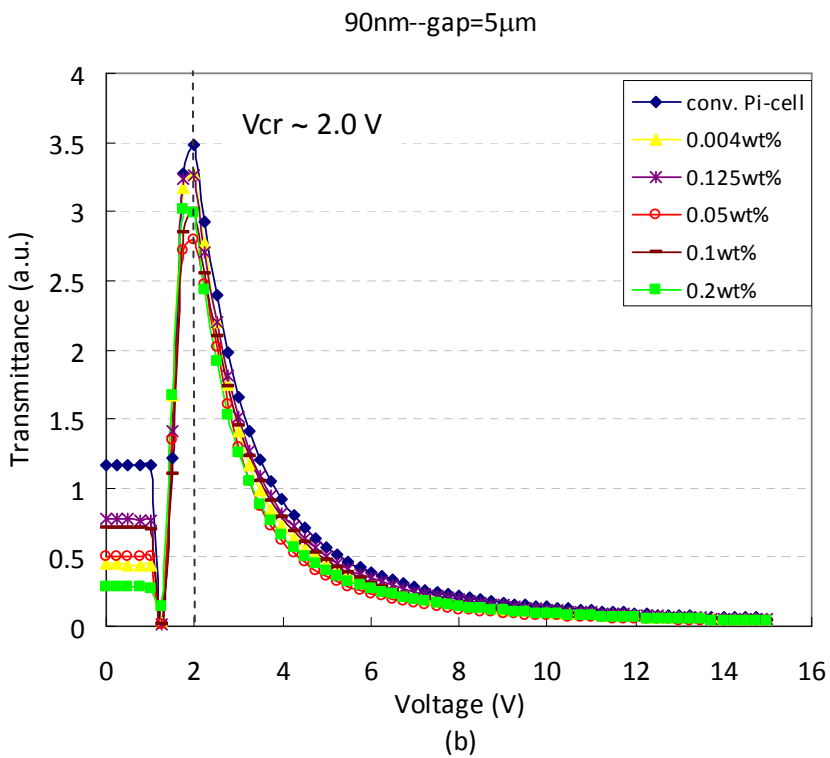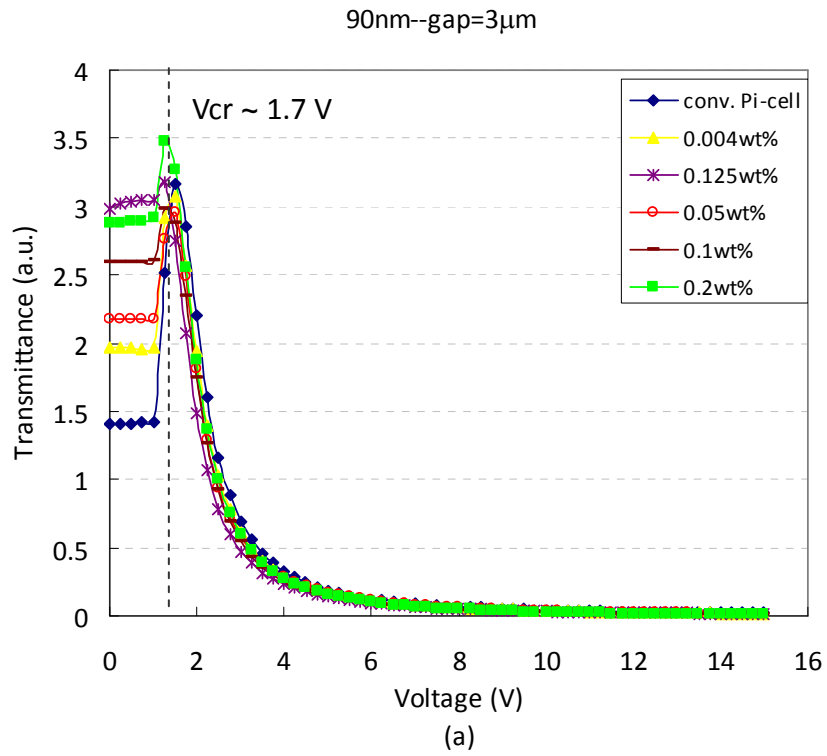
Fig. 4-15 The V-T curves of different nano-particle (90nm) concentrations with respect to (a) 3μm cell gap, and (b) 5μm cell gap.
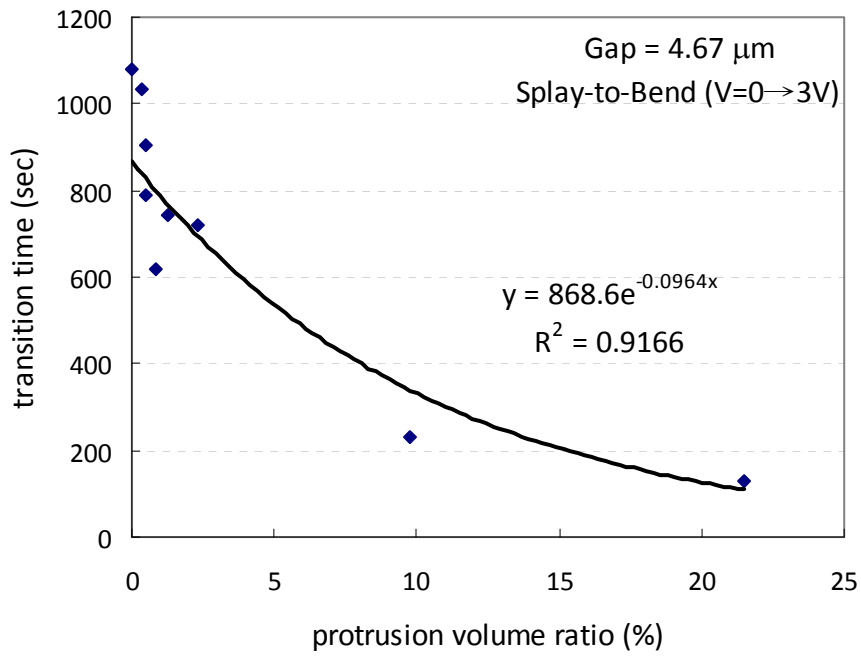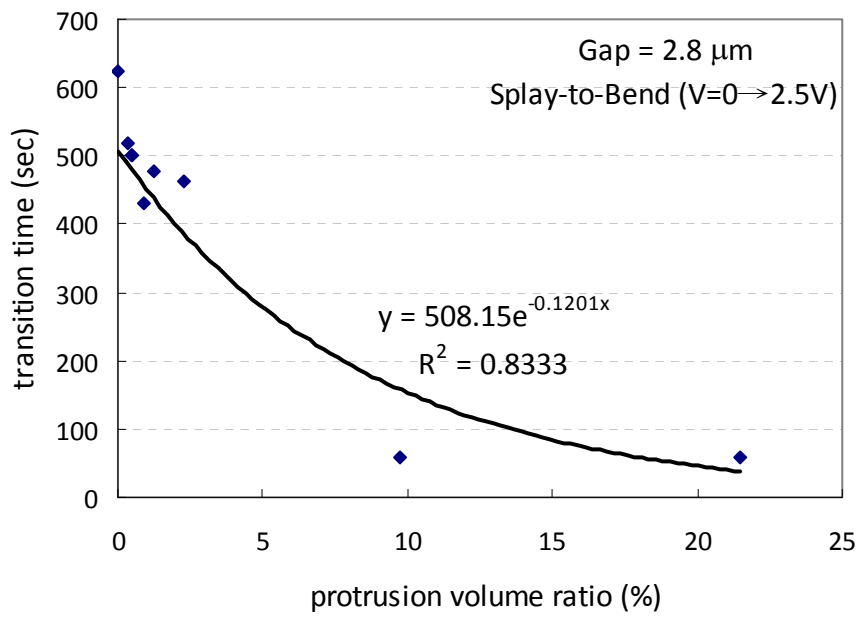
Fig. 4-16 The relationship between protrusion volume ratios and transition time of (a)
~5µm cells driven at 3V (Vcr ~ 2V), and (b) 3µm cells driven at 2.5V (Vcr ~
1.7V).

4.5 Discussions

In the novel *NE-Pi-cell*, the nanostructures are coated on the ITO glass substrates before PI coating, which differ from prior art by mixing the nano-particles with PI solution. In nanostructure fabrications, the nano-particles need to be uniformly distributed on the glass substrate without aggregation. Therefore, the nano-particles can be covered with PI layer completely, and the anchoring energy between the side chains of alignment layer (i.e. PI layer) and LC molecules will not be changed under the protrusion density limitation. Based on the concept, the critical voltage of a *NE-Pi-cell* was unchanged as a conventional Pi-cell. The mechanism of nanostructure enhanced transition rate can be confined in heterogeneous nucleation, but not anchoring effect related. Since the cell structure is purified, the discussion will be focus on the effects and limitations caused by densities, distribution and dimensions of nano-particles.

In the study, to find an appropriate solvent to disperse nano-particles uniformly is very important. In the beginning, the nano-particles were dispersed in DI water whose surface tension was very large with respect to nano-particles. Thus, the high spin speed had to be implemented to avoid the nano-particle aggregations that resulted in the limitation of the nano-particle density on the surface. However, to raise the nano-particle density is the key point in proposed *NE-Pi-cells*; the higher densities of the nano-particles, the faster transition rates under the response time limitations. Finally, the solvent composed of 10% PGMEA and 90% EG was found to resolve the fabrication issue of high nano-particle density treatment.

Since high *protrusion volume ratio* and protrusion density (μm^{-2}) would seriously affect the morphology of alignment layers, the LC directors could not be

arranged perfectly toward the same direction. As the results, the rise time of a *NE-Pi-cell* became longer when the LC molecules were relaxed, which investigated in Tab. 4-3 and 4-4. The phenomena explained that the imperfect alignment resulted in the disordered LC flow to increase the relaxation time. Although, the *protrusion volume ratio* was limited; the transition time was still reduced to about 99.9% (i.e. splay-to-bend transition is invisible under 6V driving.) when the *protrusion volume ratio* was around 3%. The response time of *NE-Pi-cells* could be remained as the same level of conventional Pi-cells.

The photographs of nucleation processes of a conventional Pi-cell and a *NE-Pi-cell* (2.5x2cm^2, cell gap~4.8μm) are shown in Fig. 4-17. The transition time was counted by the sequential video images captured by video camera under 6V driving. The frame rate was 25 fps (frames per second). It's convenient to observe the whole transition process and nucleation from spherical cluster appearing.
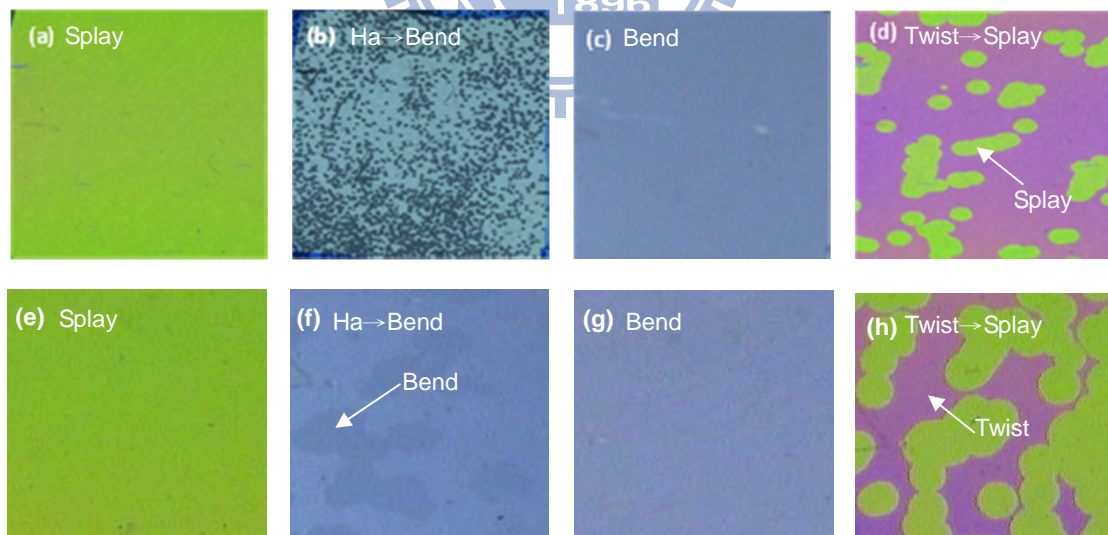
Fig. 4-17 (a)~(d) and (e)~(h) are the transition processes of a conventional Pi-cell and a NE-Pi-cell, respectively.

4.6 Summary

In this study, the transition time of splay-to-bend and twist-to-splay states have about 99.9% reduction with *protrusion volume ratio* over 3%. The nucleation process could be reduced to nearly invisible with the novel cell configuration and fabrication. Moreover, the limitation of the protrusion density was clarified by 4.2μm^{-2}. However, the electro-optical properties of the *NE-Pi-cell* were remained and almost independent of the nanostructures. In other words, the proposed *NE-Pi-cell* could not lead the critical voltage reduced or eliminated. It only enhanced the transition rate of the cells. Therefore, we suggested another method — *RMM-Pi-cell* to resolve the transition issue.

Chapter 5

Splay-to-Bend Transition-Free Reactive Monomer Modified Pi-cell

A *reactive monomer modified Pi-cell* (*RMM-Pi-cell*) comprising a layer of liquid crystal reactive monomer on one surface was prepared to control the surface pretilt angle. The simulation results suggested that a transition-free Pi-cell can be prepared by asymmetrical cell with one 8° pretilt angle and the other surface greater than 47° when the cell gap smaller than 4μm. The nematic reactive monomer (RM) layer has molecular average tilt angle over 80° which allowed the liquid crystal molecules arranged in favored bend state in the asymmetrical cell. The critical voltages cannot be found in all 3μm *RMM-Pi-cells*. The cell retardation data confirmed the initial bend orientation with zero voltage applied. Moreover, the light leakage of dark state was reduced. The *contrast ratio* (CR) of *RMM-Pi-cell* was improved by a factor of 11 compared with an original Pi-cell without using compensation film.

5.1 Introduction

Pi-Cell possesses the advantages of wide viewing angles and fast response time for liquid crystal display (LCD) application. To be useful, the conventional Pi-cells are challenged by two major issues: the splay-to-bend transition, for one, is inevitably present. Without applying a higher voltage, the active bend configuration relaxes into splay configuration [13][25][58]. The other drawback is the low *contrast ratio* (CR) caused by the light leakage in the dark state in which LC molecules can not be

vertically arranged under strong boundary condition. Furthermore, the optical axis of the LC molecules diverges by 45 degrees from the absorption axes of the polarizers. Therefore, a Pi-cell can cause a high degree of optical retardation, which in turn results in increased light leakage in dark state. Many research efforts have been intensively involved in solving the splay-to-bend transitional issue by using various methods: multi-domain alignment [24][63-64], an electrical twist field in Pi-cell [66], polymer-stabilized walls [26][67-68], and increasing surface pre-tilted angle [13] [24]…, etc.

(a)

(b)
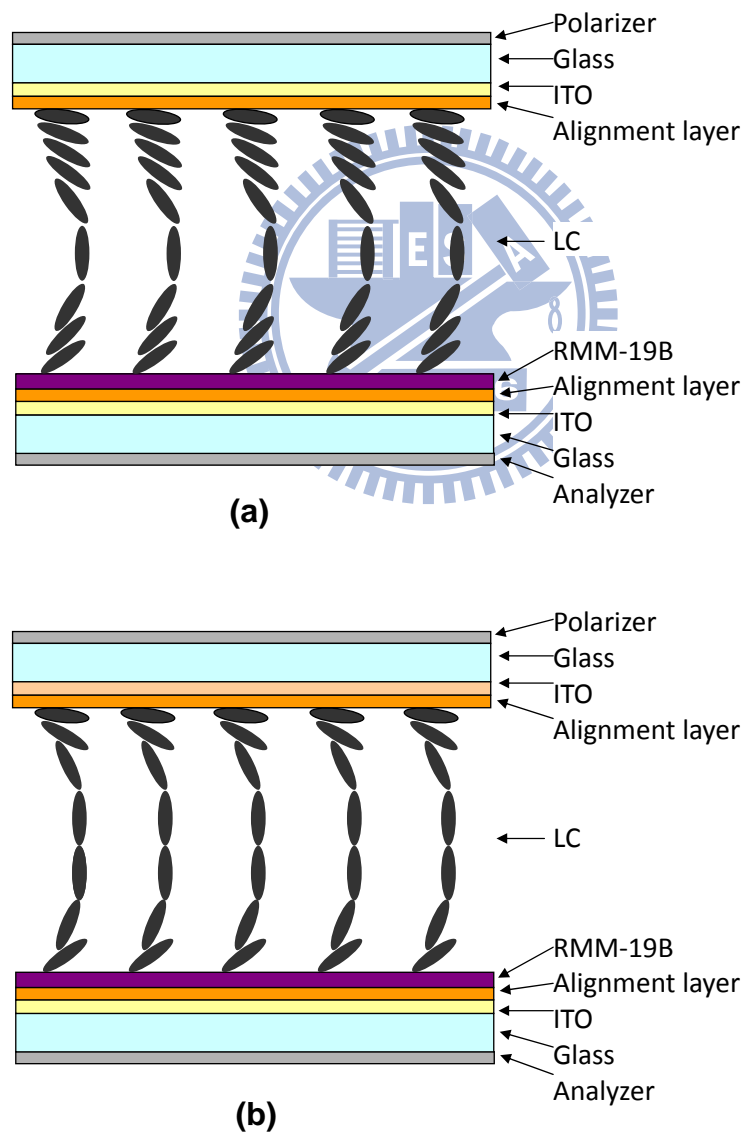
Fig. 5-1 The scheme of RMM-Pi-cell under (a) 0V and (b) 6V.

In this study, we report a transition-free *reactive monomer modified Pi-Cell* (*RMM-Pi-cell*), assembled with RM at one side and buffed PI surface at the other side, configured as Fig. 5-1, in which the splay-to-bend transition is suppressed and contrast ratio is enhanced by a factor of 11 than a conventional Pi-cell [69-70].

5.2 Experiments and Simulations

5.2.1 RMM-Pi-cell Fabrication

The polyimide alignment film (PI: PIA-5580-01, Chisso Co.), compounded into the solvent (PI: solvent = 3:1), was prepared by spin-coated on a 2 cm × 2.5 cm indium-tin-oxide (ITO) glass and hard baked at 220 ^{o}C for 1 hr. The 8°~12° pre-tilt angles were obtained after buffing the cured PI film. The propylene glycol mono-methyl ether acetate (PGMEA) solutions, comprising various concentrations of reactive monomer (RMM-19B, Merck Chemicals Ltd., see the Appendix C), were spin-coated on a PI buffed ITO glass. Then, the *reactive monomer* (RM) film sample was exposed by UV lamp and baked at ~45°C for 5 minutes at the same time. The thickness of RM film was controlled by solution's concentration and spin coater's speed. The process conditions of RM films are listed in Tab. 5-1. The film thickness was measured by the height of the cross section, using atomic force microscope (AFM). The relationships of film thicknesses and coater's rotation speeds with respect to different concentrations of the RM solution are shown in Fig. 5-2.

Tab. 5-1 The spin-coating conditions of RM films.

Step 1: RM film coating		
	Spin (rpm)	Time(sec)
1st spin	500	30
2nd spin (for different thickness)	6000	60
	4000	
	2000	
Step2: (Baking45 °C + UV Exposure)x 5min		
RM solution's concentration: 4wt%, 2wt% and 1wt%		
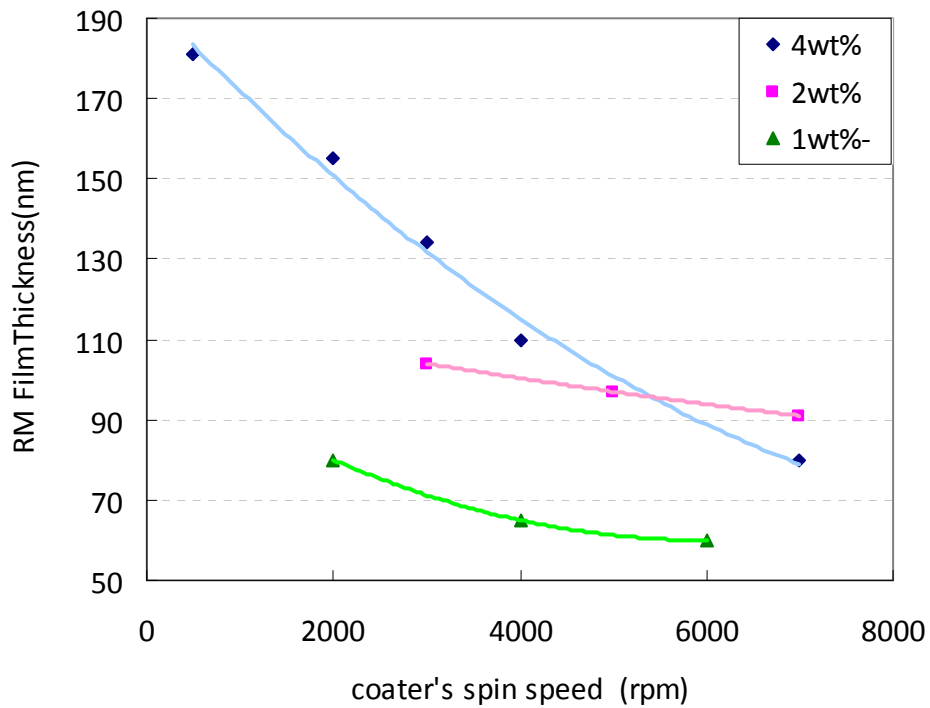
Fig. 5-2 The relationships of film thicknesses and spin speeds of coater with respect to different concentrations of the RM solution.

RMM-Pi-cell was assembled with RM on one side and buffed PI surface on the other side, as shown in Fig. 5-1. The cell gap was controlled at either ~3 or 5 μm. The liquid crystal (LC: ZCE-5096XX, Chisso Co., see the Appendix B.) was filled by

capillary force into the cell for electro-optical characterizations. The retardations of *RMM-Pi-cells* and RM thin films were measured by Soleil-Babinet Compensator. The fabrication processes are illustrated in Fig. 5-3.
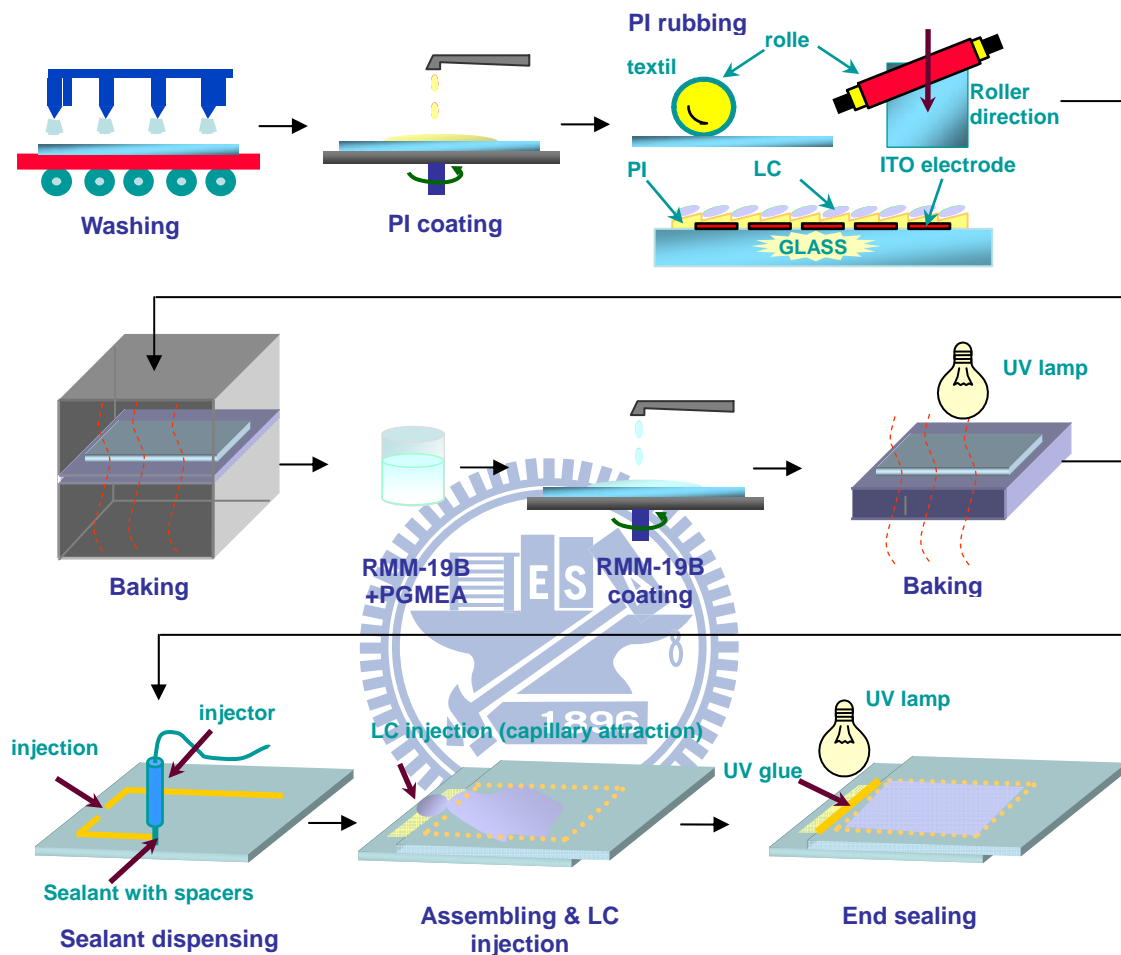
Fig. 5-3 RMM-Pi-cell fabrication processes in laboratory.

5.2.2 Critical Pretilt Angle Estimation

In order to verify the initial bend orientation without splay configuration in *RMM-Pi-cell*, we calculated the lowest pretilt angle requirements and probed the RM's surface pretilt angle, in addition to cell retardation's measurement. In the calculation, the symmetrical Pi-cell was considered first, the relationship between the driving voltage and electric field can be simplified as $E \sim U/d$. The Gibbs free energy

of spay and bend cells can be calculated by Eq. (5-1) [13][71]:

$$G = \frac{1}{2}\int_0^d \left[\left(K_{11}\cos^2\theta + K_{33}\sin^2\theta \right)\left(\frac{d\theta}{dz}\right)^2 - \varepsilon_0\Delta\varepsilon E^2\sin^2\theta \right]dz \qquad (5\text{-}1)$$

where K_{11} and K_{33} denote the splay and bend elastic constants; and ε_0 and $\Delta\varepsilon$ are the dielectric constant in vacuum and dielectric anisotropy, respectively. $\theta(z)$ is the LC tilt angle on z direction perpendicular to the glass substrate. The critical pretilt angle, α_c, for a transition-free Pi-cell can be derived from Eq. (5-2) [13][72]:

$$\left(K_{33} - K_{11} \right)\sin(2\alpha_c) + \left(K_{33} + K_{11} \right)\left(\pi - 4\alpha_c \right) = 0 \qquad (5\text{-}2)$$

Based on the calculation, the relationship between K_{33}/K_{11} and critical pretilt angle is shown in Fig. 5-4. The critical pretilt angle is around 46°, which calculated from the LC used in experiment (LC: ZCE-5096XX, K_{11}=9.8 pN, K_{33}=11.8 pN at 20°C), for a symmetrical Pi-cell to form bend state configuration.
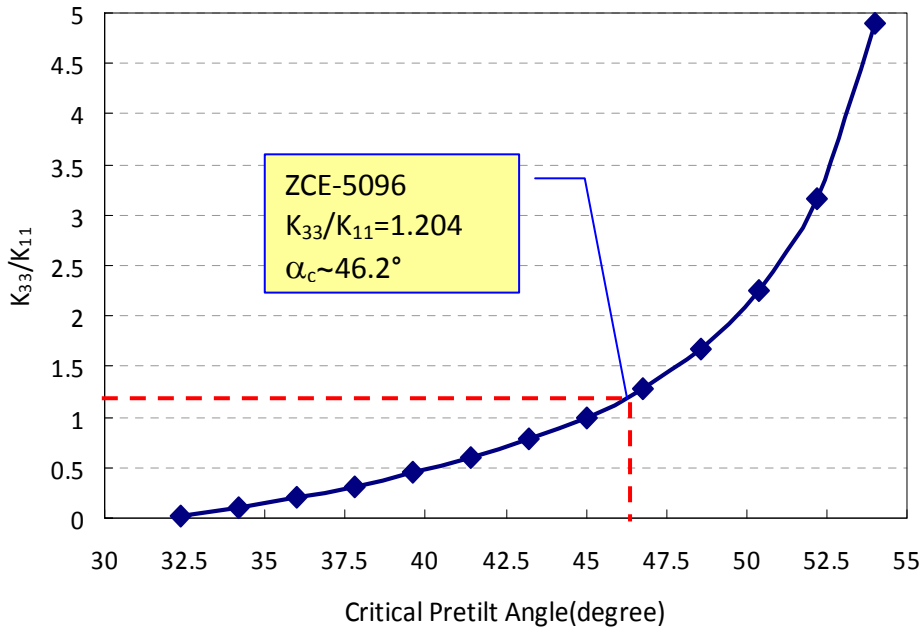
Fig. 5-4 The relationship between K_{33}/K_{11} and critical pretilt angle.

5.2.3 Asymmetry Pretilt Angle Combination Simulations

By varying surfaces pretilt angle on both top and bottom surfaces for asymmetrical cells, the Voltage vs. Transmittance (V-T) curves simulated by DIMOS program suggested that the bend state configuration can also be achieved by surface pretilt angle of top/bottom substrates at 8°/47° and 10°/45° in a 4 μm cell. The V-T curves of the two combinations due to the Gibbs energy of bend state configuration (6.6 μJ/m^2) lower than spray state are investigated in Fig. 5-5 and 5-6. As the results, the simulation result suggested that a transition-free Pi-cell can be prepared by asymmetrical cell with one regular 8° pretilt angle and the other surface greater than 47° when its cell gap smaller than 4 μm.
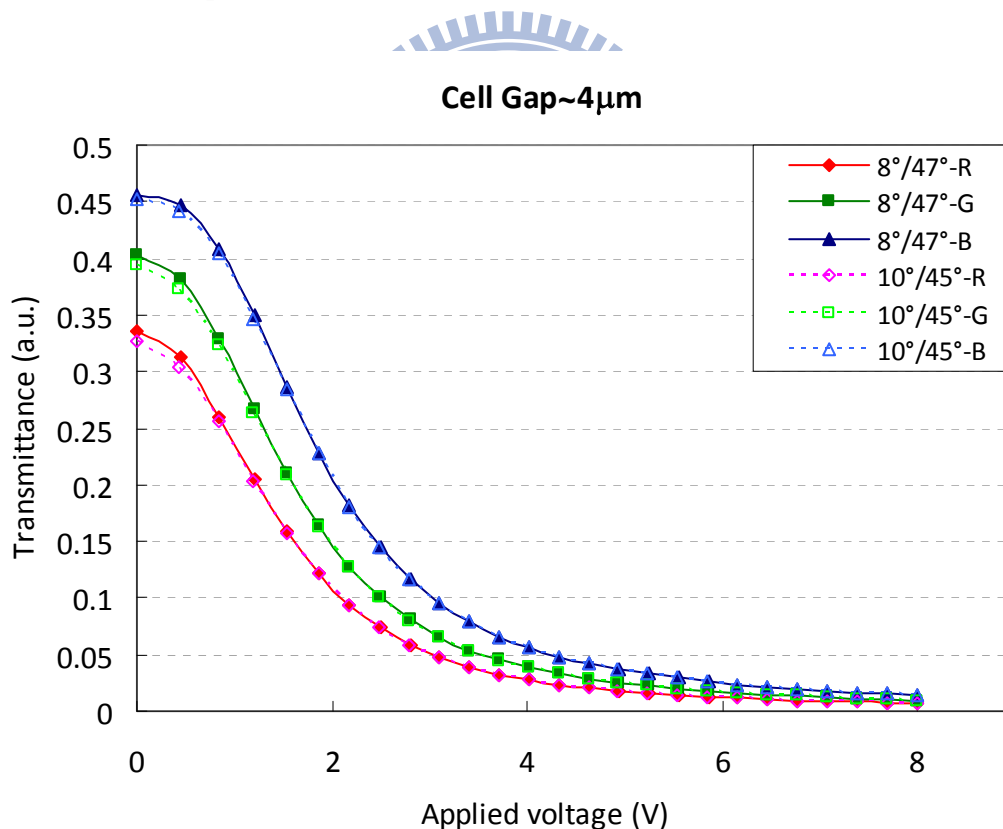
Fig. 5-5 The simulations of V-T curves of two pretilt angle combinations.
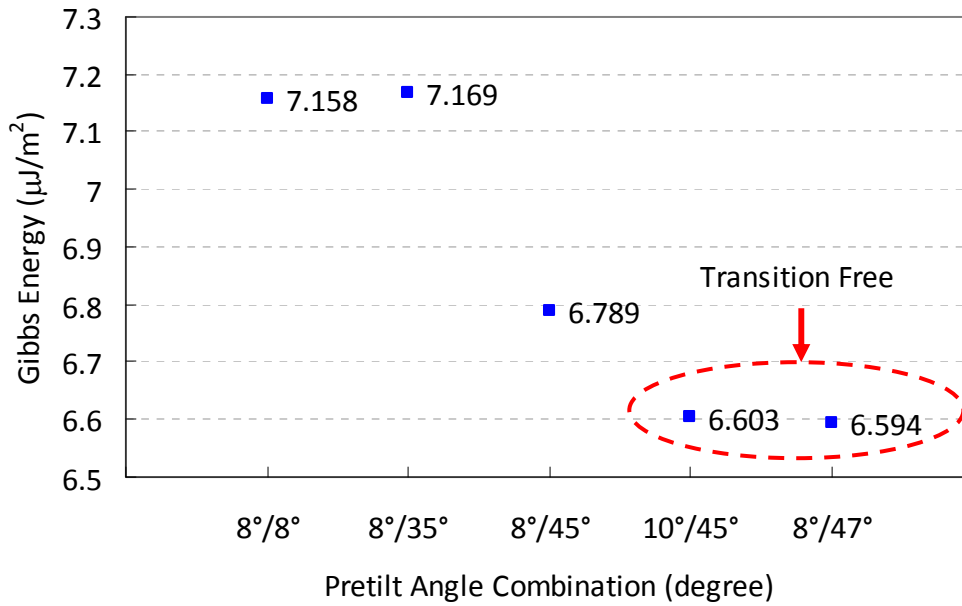
Fig. 5-6 The Gibbs energies of different pretilt angle combinations.

5.3 The Investigation of RM films' Retardations

The critical voltages to hold bend state measured at λ= 633nm were 0.6, 0.2 and

0 V for RM's thickness of 80, 110 and 134 nm in 5 μm *RMM-Pi-cells*, respectively.

On the contrary, the state transition was not found even in the thin RM layer for all 3

μm cells. Above mentioned results were shown in Tab. 5-2. The experimental results

confirmed the DIMOS simulation. Further investigation was carried out to determine

the RM's surface pretilt angle. RMM-19B's Δn_{RM} (at λ=452nm), 0.1449, was obtained

from a 1.58 μm homogenous planar cell. Based on the measured result (Δn_{RM}

=0.1449), the retardation of a 200 nm homogenous RM thin film should be in 28.98

nm. The thin RM film's retardations, however, were observed in 0.17 and 0.09 nm for

the thickness of 237 and 120 nm, respectively. The discrepancy suggested that the

liquid crystalline molecular orientation in RM film was highly tilted. In order to

simplify the liquid crystal's pretilt angle calculation, we assumed a uniform molecular tilt orientation for RM film. In the uniaxial RM case, the index ellipsoid of the RM, as illustrated in Fig. 5-7, is represented by the Eq. (5-3). In the Fig. 5-7, the cross section of the RM cut by a plane, which is perpendicular to the wave vector, shows an ellipse whose long axis gives the effective extraordinary index of refraction $n_{e\text{-}RM}(\theta)$ and short axis gives the effective ordinary index of refraction $n_{o\text{-}RM}(\theta)$, which is equal to the ordinary index of refraction $n_{o\text{-}RM}$, for corresponding wave vector. Substituting the $n_{e\text{-}RM}(\theta)$, which was calculated from the RM's retardation value, into Eq. (5-3) [20][32], the average tilt angles θ of RM layers were calculated at 85° to 86° with assuming $n_{o\text{-}RM} = 1.5$, according to various film thickness. The results were summarized in Tab. 5-3. The deviation of tilt angle was around ±0.02° when RM's $n_{o\text{-}RM}$ increased or decreased by 10 %.

$$\frac{1}{n_{e-RM}^{2}(\theta)} = \frac{\sin^2 \theta}{n_{o-RM}^{2}} + \frac{\cos^2 \theta}{n_{e-RM}^{2}}, \quad \text{where } n_{e-RM}(\theta) = \Delta n_{RM}(\theta) + n_{o-RM}, \qquad (5\text{-}3)$$
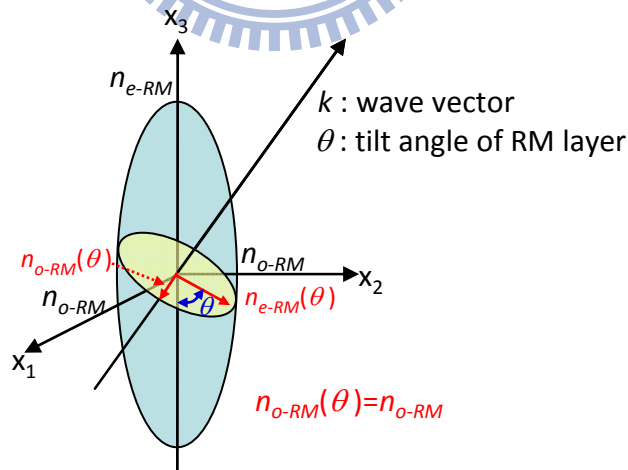
Fig. 5-7 The index ellipsoid of the RM in diagonal frame.

The calculated average RM tilt angle is much greater than theoretical critical pretilt angle required in an asymmetrical Pi-cell. As the results, the LC molecules in a

RMM-Pi-cell favored in bend orientation at its initial state without applying voltage [73]. To further confirm the bend state orientation, the retardation profiles of conventional Pi-cell and *RMM-Pi-cell* under different driven voltage from 0 to 6V with respect to different viewing angles were investigated in Fig. 5-8 (a) and (b). The conventional Pi-cells have larger retardation curves compared with the *RMM-Pi-cells*, when the applying voltage is higher than critical voltage. As the Fig. 5-8 (b), the retardation profiles of a *RMM-Pi-cell* driven from 0 to 6V were similar to the conventional ones' driven at the voltages larger than critical voltage (from 2 to 6V). The results confirmed that the LC molecules were arranged in the bend orientation at its initial state without applying any voltage in *RMM-Pi-cells*.

Tab. 5-2 The 4wt% RMM-Pi-cells and conventional Pi-cell.

Cell name	Pi-cell	RMM-1	RMM-2	RMM-3	RMM-4	RMM-5	RMM-6
Cell Gap (μm)	~4.0	4.7±0.05			3.3±0.05		
RM thickness	None	80nm	110nm	134nm	80nm	100nm	110nm
Critical voltage	1.6V	0.6V	0.2V	0V	0V	0V	0V
CR	26	123	224	273	138	211	288
Dark State (8V)	3.79	0.82	0.45	0.37	0.73	0.47	0.35

*Without using compensation films

Tab. 5-3 The pretilt angle calculations of the 4wt% RM films.

Coater Speed (rpm)	2000	4000	6000
Thickness (nm)	237	120	100
RMM Retardation (nm)	0.17	0.09	≦0.09
Effective pretilt angle θ (degree)	85.74	85.48	~85
Δn_{RM}-from a homogenous *RMM-Cell* (cell gap ~1.58um)			0.1449
RMM material -$n_{o\text{-}RM}$ (assumption)			1.5

70
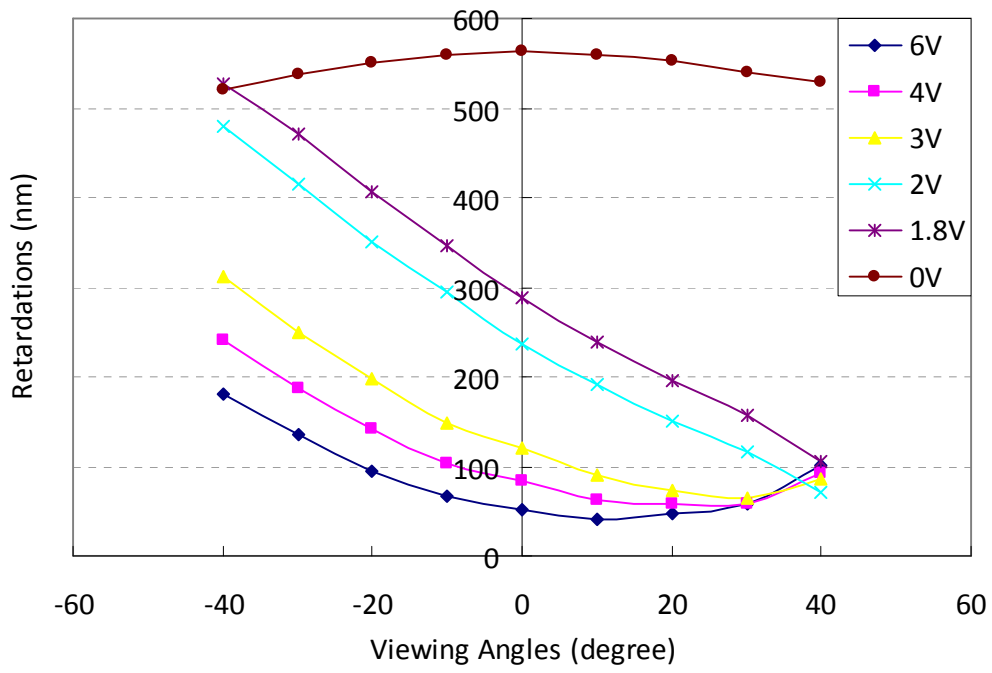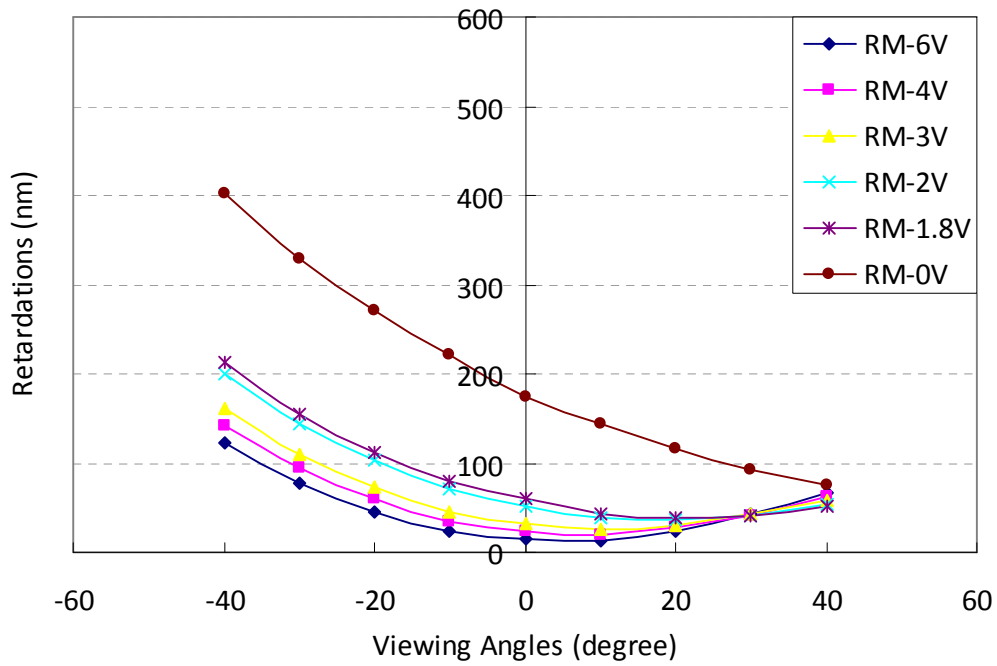
Fig. 5-8 Retardations of (a) the conventional Pi-cell, and (b) RMM-Pi-cell with different driving voltage from 0V to 6V in different viewing angles (Measuring wavelength=632.8nm).

5.4 The Optical Properties of Transition-Free RMM-Pi-cells

The normalized V-T curves of *RMM-Pi-cell* shifting to the left without critical voltage confirmed that it was a transition-free cell as illustrated in Fig. 5-9 (a). Furthermore, the un-normalized R, G and B V-T curves indicated the transmittance in bright state was not seriously compromised in a *RMM-Pi-cell* as shown in Fig. 5-9 (b). The residual retardation from RM's splay orientation may have contributed to non-compromised transmittance in *RMM-Pi-cell* comparing to the high tilted conventional Pi-cell. The light leakage after 4V was largely suppressed in the proposed cell structure. The retardations of the *RMM-Pi-cell* corresponding to different viewing angles were lower than the conventional Pi-cell, shown in Fig. 5-8 (b). The results suggested that the LC molecules of the *RMM-Pi-cells* can be arranged vertically, much closer to the cell boundaries at the dark state. The light leakage, therefore, was reduced in *RMM-Pi-cell*. Without utilizing compensation films, the contrast ratio of the RMM-Pi-cell can be improved by a factor of 11 than the conventional Pi-cell. The improved contrast ratios of *RMM-Pi-cell* cells in 4.7 and 3.3 μm were shown in Fig. 5-10. The proposed device possessed high contrast ratio, therefore, the viewing angle of *RMM-Pi-cell* was also wider than conventional one's. As shown in Fig. 5-11, the *Viewing-Angle* (V.A.) ranges, defined by CR>10, of a Pi-cell and a *RMM-Pi-cell,* whose cell gaps were ~around 4 μm, were 0°/40°/0°/50° and 40°/50°/60°/50° for the corresponding viewing orientations 0°/90°/180°/270° (right/ up/ left/ down orientations) measured by green LED, respectively. However, the central contrast ratio of conventional Pi-cell cell was smaller than 10 in 10° V.A. ranges. The *RMM-Pi-cell*'s driving voltage can be reduced to 0 ~ 7 V without applying high voltage pulse. The advantages of the transition-free *RMM-Pi-cell* are not only higher in contrast ratio, but also lower in power consumption than the

conventional Pi-cell.
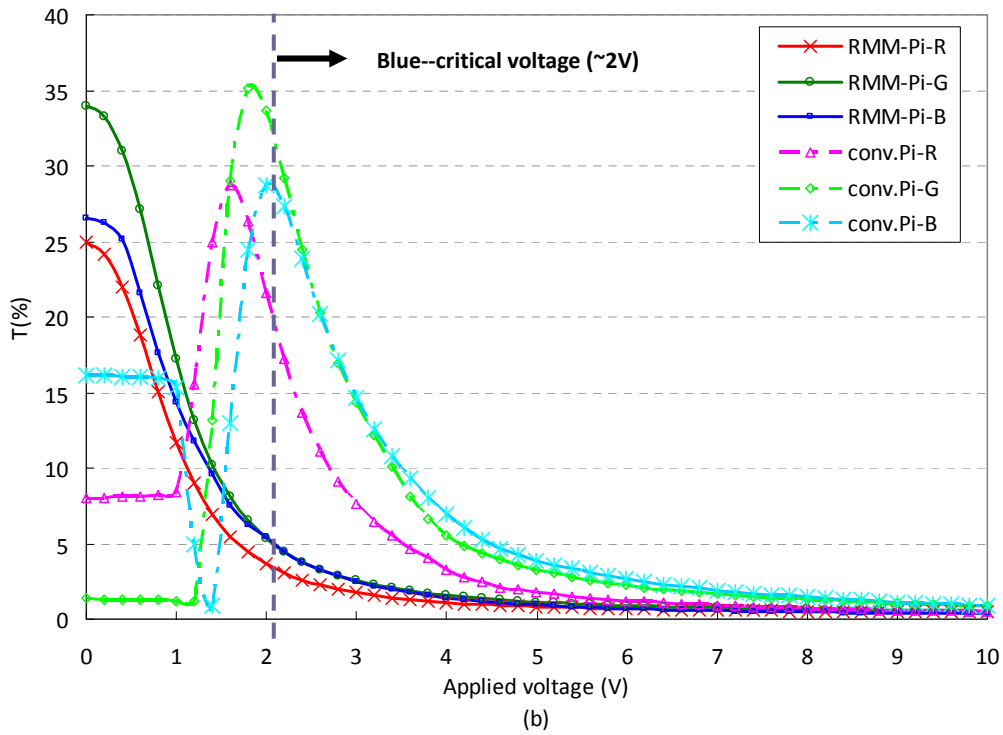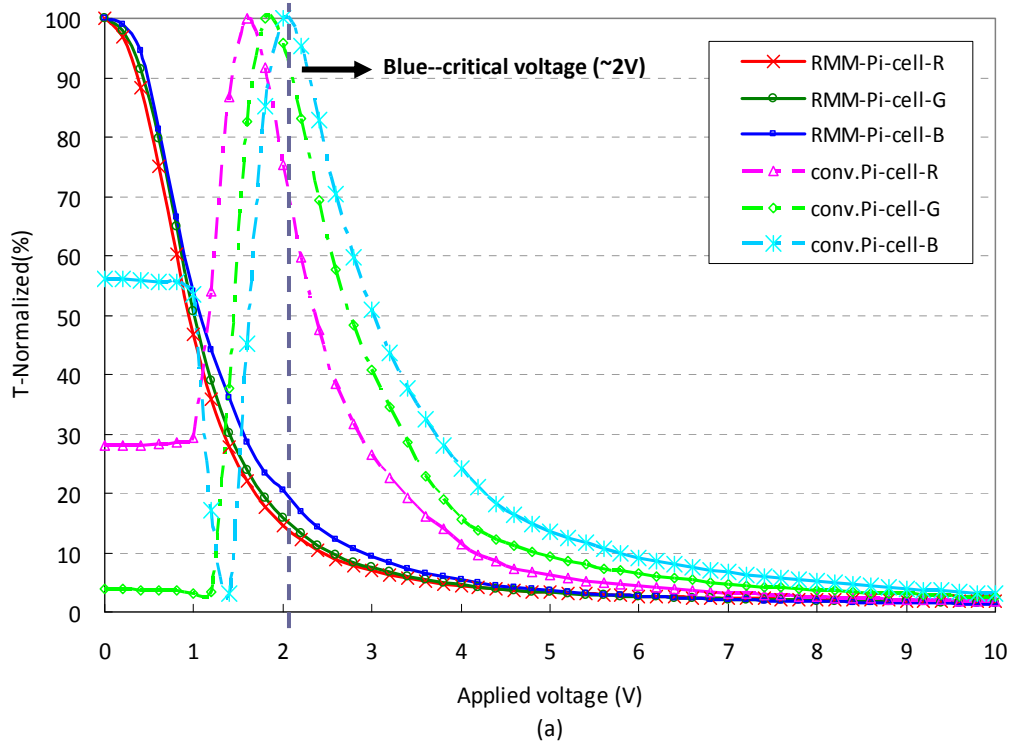
Fig. 5-9 (a) The normalized RGB's V-T curve, and (b) Un-normalized RGB's V-T curve of RMM-Pi-cell and conventional Pi-cell without compensation films.

RM Thickness	Conv. Pi-cell	80 nm	110 nm	134 nm
■ 4.7μm	26.4	123.0	224.0	272.6
▦ 3.3μm	26.4	137.5	211.4	287.9
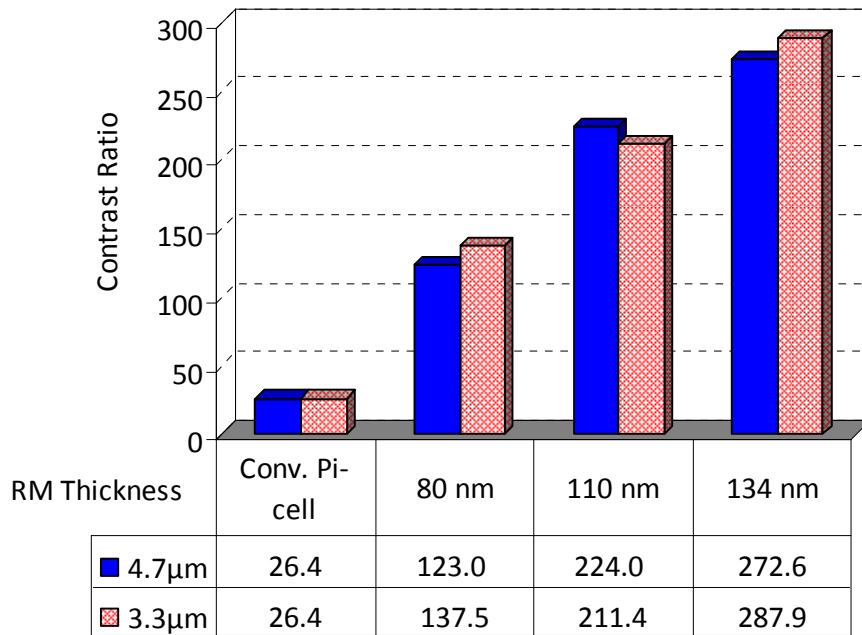
Fig. 5-10 The improved contrast ratios of RMM-Pi-cell cells in 4.7 and 3.3 μm (Max. improved factor is 11).

(a)   (b)
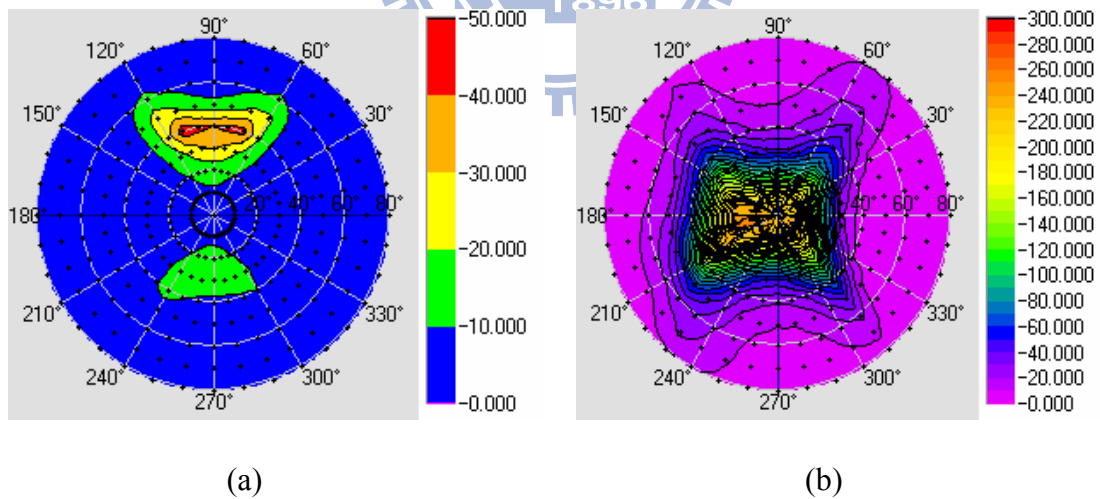
Fig. 5-11 The Iso-Contrast Contour Diagrams of (a) Pi-cell and (b) RMM-Pi-cell. The V.A. ranges are defined by CR>10 (Measuring light source is green LED.).

5.5 Discussions

The photos of the *RMM-Pi-cell* compared with conventional Pi-cell are shown in Fig. 5-12. The Figs. 5-12 (a), (b), (c) and (d) represent the different driving voltages were applied on a *RMM-Pi-cell*, respectively. The Figs. 5-12 (e), (f), (g) and (h) represent a conventional *Pi-cell* applied the different driving voltages, respectively. To compare Figs. 5-12 (a) and (e), the photo (a) showed the real bright state but photo (e) showed bluish color; in other words, the result meant the *RMM-Pi-cell* was in bend state without applying voltage and the conventional Pi-cell was in splay state until the driving voltage over 2V, shown in photo (f). As the results, the transition-free *RMM-Pi-cell* is achieved and the operation range is from 0 to 5V, smaller than the range of a conventional Pi-cell from 2 to 7V in real display applications.

RMM-Pi-cell (*CR~288*)

| (a) 0V-bend | (b) 2V | (c) 4V | (d) 7V |

Conv. Pi-cell (*CR~26*)

| (e) 0V-splay | (f) 2V-bend | (g) 4V | (h) 7V |
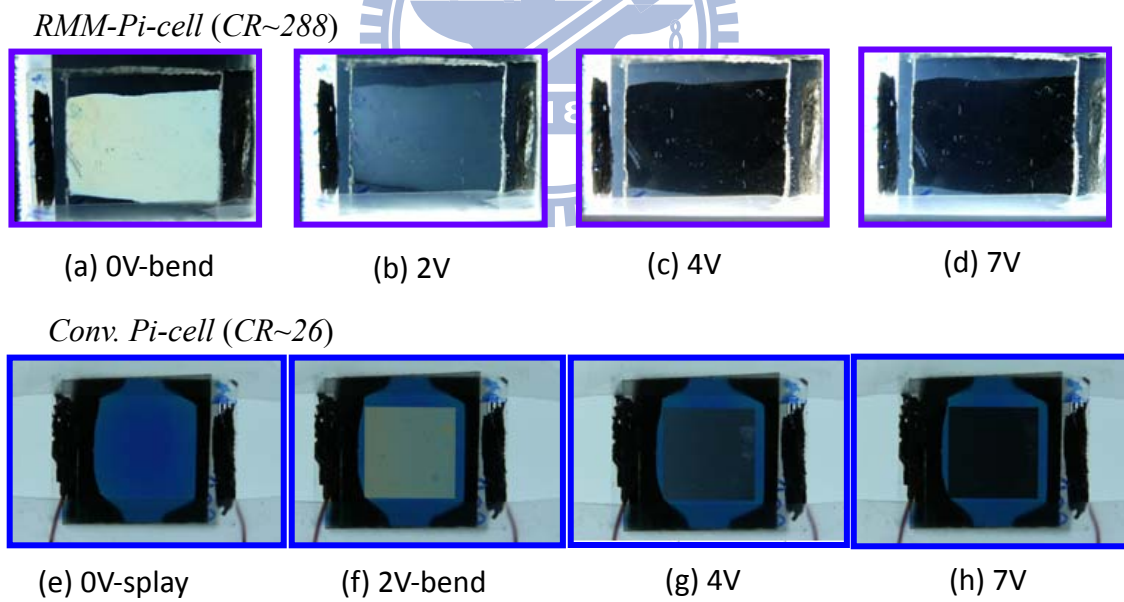
Fig. 5-12 (a) ~ (d) were the photos of a RMM-Pi-cell and (e) ~ (f) were the photos of a Pi-cell (cell gap ~ 4μm) under different driving voltages, respectively.

The proposed transition-free *RMM-Pi-cell* can be realized, nevertheless, there is

suspected response time degradation. In the experiments, the average response time was not always less than 3ms; sometimes the response time would be degraded to the level of a TN-cell. One possibility is the anchoring energy maybe becomes weaker between LC molecules and the RM film during the fabrications. We think the RM film's quality affects the anchoring force between the RM film and LC directors. Therefore, both the anchoring energy and the fabrication conditions of the RM films need to be investigated in the future. The other possibility is the intrinsic properties of the RM film which are not stable enough for thin film (200~300nm) fabrications. In other words, the material properties of the RM film also have to be considered and further investigated. How to improve the anchoring force and find the optimized fabrications are important for keeping stable fast response property in Pi-cell. Anyway, the issue needs to be confirmed in the future work.

5.6 Summary

In summary, the *RMM-Pi-cell* can be driven without a state transition. The tilt angle of the *RMM-Pi-cell* has been confirmed theoretically and experimentally. The residual retardation of splay type thin film with highly tilt surface angle maintained the bright state's transmittance and reduced the dark state's light leakage. The contrast ratio was improved up to a factor of 11. The proposed device possessed high contrast ratio, therefore, the viewing angle was also wider than conventional one's. The *Viewing-Angle* (V.A.) range, defined by CR>10, of *RMM-Pi-cell* was 40°/50°/60°/50° for the corresponding viewing orientations 0°/90°/180°/270° (right/ up/ left/ down orientations) without using compensation films, respectively. Therefore, the proposed *RMM-Pi-cell* is suitable for low power consumption, for a better image quality in large size TFT-LCD applications.

Chapter 6

Conclusion and the Future Work

The themes of advanced TFT-LCD technology, shown in Fig. 6-1, are motion blur improvement, high brightness and high contrast ratio. In order to enable the Pi-cell to be more appealing for high-end display applications, we explored the fundamental LC features of a Pi-cell. There are two approaches reported here to improve the transition rate and eliminate the splay-to-bend transition of a conventional Pi-cell by the proposed *NE-Pi-cell* and *RMM-Pi-cell*. Our studies were focused on fast response Pi-cell development for resolving the motion blur issue and realizing non-color break up (CBU) FSC-LCDs in the future.
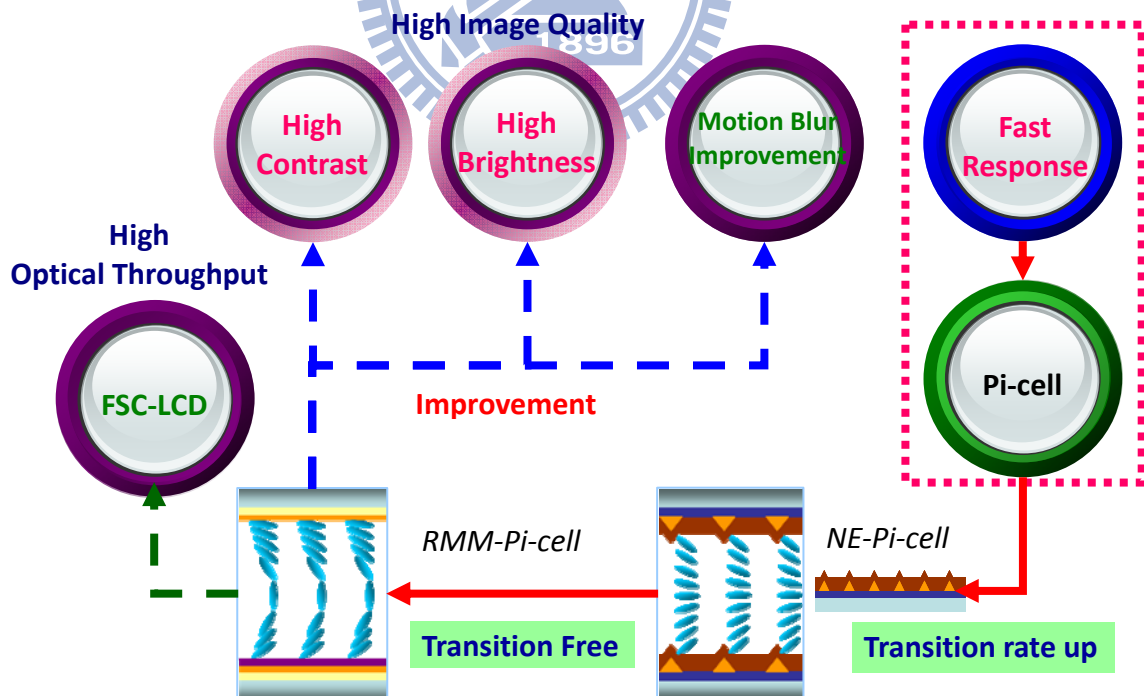
Fig. 6-1 The research topics explored and concluded in this dissertation.

6.1 Conclusion

6.1.1 Investigation of Transition Effect in a *NE-Pi-cell*

Pi-cell, one of the fast response solutions in LC-cells, has been reported to have five intrinsic liquid state transitions which have led to several issues in operation. In LCD applications, the most popular technology to resolve slow and non-uniform transition processes is the high pulse transverse driving method which promotes transition, but the method reduces the aperture ratio of a pixel and increases the loadings of the panel and driver IC. Therefore, we proposed *NE-Pi-cell* which demonstrated a uniformly fast transition cell structure. The novel cell structure and nanostructure fabrication results are summarized in Fig. 6-2.
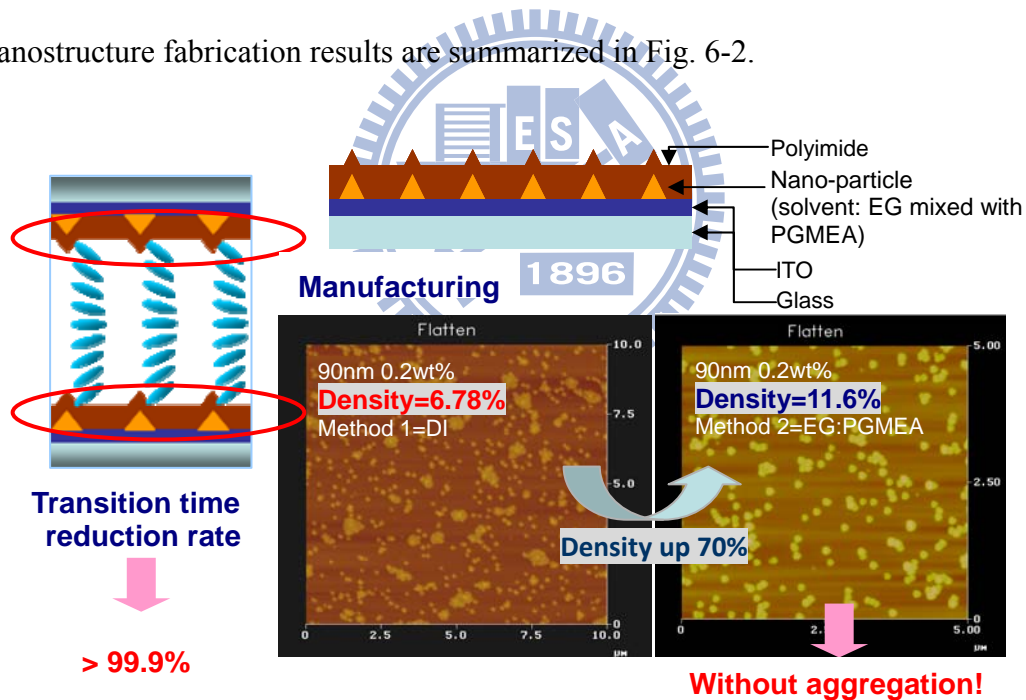
Fig. 6-2 The designed nano-particle treated cell structure and the density increase of nano-particles without aggregation.

The proposed method was successful to reduce transition time to almost 0 (reduction rate is over 99.9%). In addition, we also explored the fabrication method to

overcome nano-particle aggregations with high nano-particle density. The nano-particle density is increased from 6.78% to 11.6% (improvement rate is over 70%).

The photographs of the nucleation processes proved the transition speed of a *NE-Pi-cell* was faster than the conventional one with same driving voltage, investigated in Fig.6-3. Figs. 6-3 (a) and (c) are the transition processes of a *NE-Pi-cell*; Figs. 6-3 (b) and (d) are the transition processes of a conventional Pi-cell. Comparing Figs. 6-3 (a) with (b), the spherical cluster radius of *NE-Pi-cell* is larger than conventional ones. In other words, the nucleation proceeded and clusters grew faster in a *NE-Pi-cell*. The photographs (c) and (d) also show the same results. According to our investigation, the transition rate is very positive in relation with the protrusion density, which determines the quantities of potential nucleation sites and limited by response time degradation. The results match with the transition rate equation in the nucleation theory.
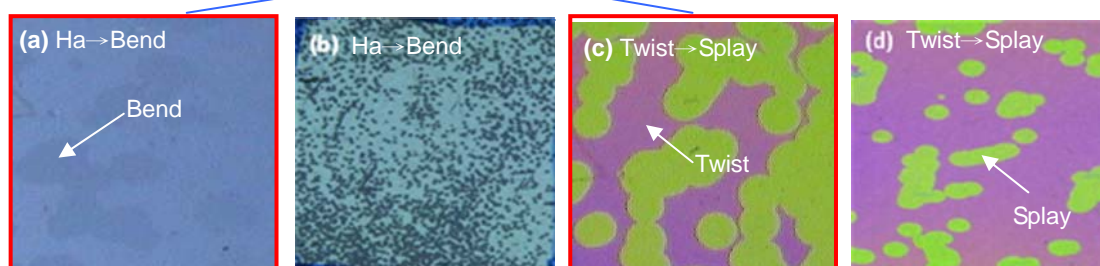
Fig. 6-3 The photographs show the transition processes of (a) a NE-Pi-cell, and (b) a conventional Pi-cell from Ha to bend state, respectively; moreover, the (c) and (d) are with respect to the transition from twist to splay state of a NE-Pi-cell and a conventional Pi-cell.

6.1.2 Splay-to-Bend Transition-Free *RMM-Pi-cell*

Even if proposed *NE-Pi-cell* can improve the transition speed to almost invisible and proceed to nucleation uniformly, the compromised transmittance of R, G and B caused by splay-to-bend transition still degrades the optical performance of a LCD. Moreover, the other drawback is the low *contrast ratio* (CR) caused by the light leakage in the dark state in which LC molecules cannot be vertically arranged under the strong boundary condition. The novel *RMM-Pi-cell* can achieve a transition-free Pi-cell. The design concept and the V-T curves of the *RMM-Pi-cell* are shown in Fig. 6-4. As the V-T curves of R, G, and B, we successfully eliminate the critical voltage and the maximum transmittance is driven at 0V. In other words, the transmittance of R and G are no longer compromised by critical voltage blue (~2V) and increased by 25%. Moreover, the contrast ratio can also be improved by a factor of 11.
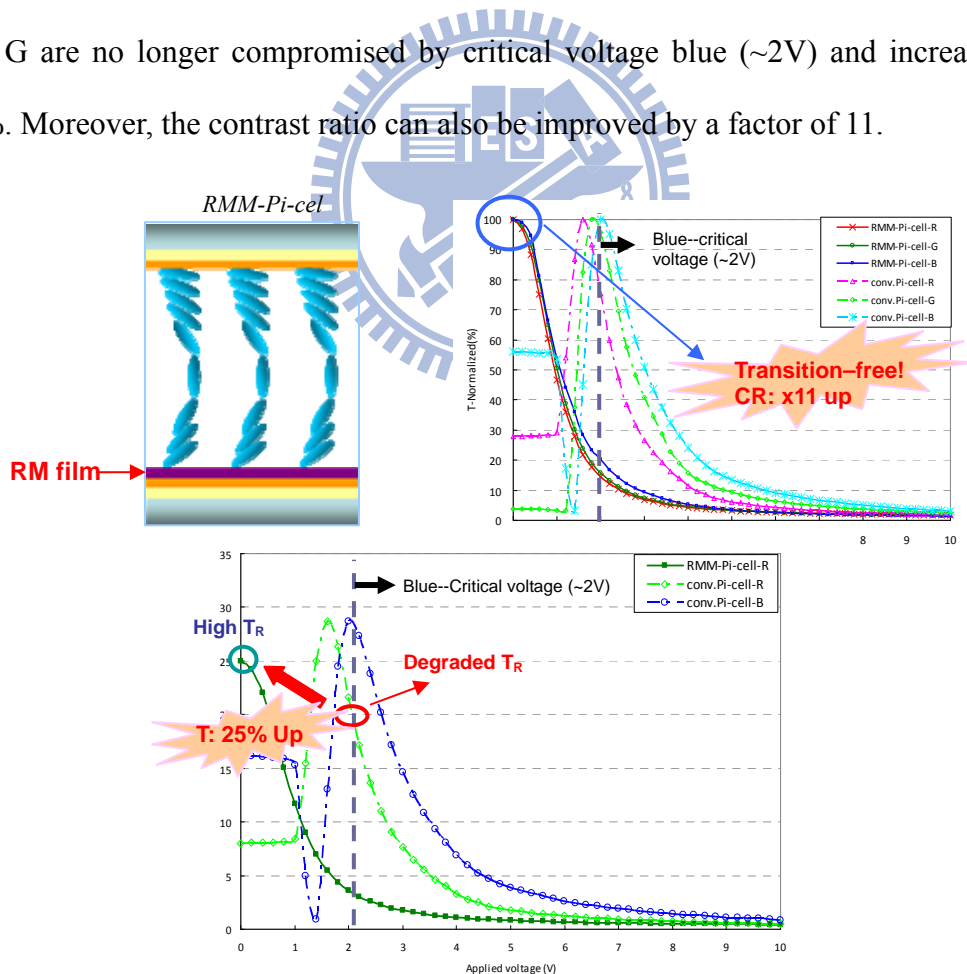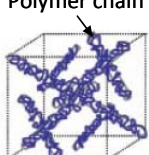
Fig. 6-4 The improvements of the transmittance and the contrast ratio in a novel transition-free RMM-Pi-cell.

The comparison of various transition-free Pi-cells and RMM-Pi-cell is shown in Tab. 6-1. The *RMM-Pi-cell* is certainly a better solution for a transition-free request. However, the suspected response time degradation should be further investigated in future works. The blue phase is also an interesting topic for us recently. We also compare it with the proposed *RMM-Pi-cell* in Tab. 6-1. The blue phase possesses wide viewing angles, high optical performance, fast response (~1ms) and easy fabrication. However, the LC material of blue phase needs to face many issues, such as narrow temperature range (~60°K), lower induced optical birefringence and very high driving voltage (60~100V) [74]. Maybe, the blue phase will be a better choice in future display applications, but the issues lead to many difficulties in display applications. Now we still want to propose the fast response, transition-free and easy commercialized Pi-cells for LCD image quality improvement and the realization of non-CBU FSC-LCDs.

Tab. 6-1 Comparison of different fast response LC-cells.

Pi-cells	Conventional	Polymer-Stabilized	Initially Twist	RM modified	PS-Blue Phase
LC Profile					Polymer chain
Inventor	P. J. Bos & T. Uchida	L. C. Chien	J. C. Kim	NCTU	H. Kikuchi
State Transition	With	Without	Without	Without	Without
Response	◎	○	X	△(?)	◎
Contrast Ratio	○	X	○	◎	◎
Transmittance	○	○	○	◎	○
Material	◎	◎	◎	◎	X
Fabrication	◎	△	○	○	◎

◎: Excellent ○: Good △: Acceptable X: Poor

6.2 Future Works

The proposed future works focus on three aspects — the investigation of the suspected response degradation in *RMM-Pi-cell*, the fabrication optimization of RM film for anchoring force enhancement and film uniformity, and the implementation of the *RMM-Pi-cell*. Due to suspected response degradation, one possibility is that anchoring energy between LC molecules and RM film becomes weaker. If the fabrication condition of RM film can be optimized and investigated more thoroughly, the response time issue can be clarified and resolved.

6.2.1 Anchoring Effect Investigation between RM Film and LC

In chapter 5, we proposed *RMM-Pi-cell* to resolve the transition and recovery issues in conventional Pi-cell. Even though the *RMM-Pi-cell* is transition-free with better optical properties compared with prior arts, the response time degradation is still suspected. The response time of an LC cell is influenced by the LC cell structure and the interaction between alignment layers and LC molecules, well-known as the anchoring effect. Due to the novel cell structure of *RMM-Pi-cell*, extra RM film was treated on the alignment layer (PI), thus, the anchoring force would be changed by RM film. Based on the anchoring effect, the anchoring force leads the LC directors to return to the easy axes which determined by the rubbing directions and pretilt angles of alignment layers at the both cell boundaries. If the anchoring force between LC molecules and alignment layers is not strong enough, the LC directors can not return rapidly when the driving voltage is released. In other words, the response time of an LC cell will become slower.

Therefore, the anchoring force between RM film and LC molecules needs to be investigated. How to precisely measure the anchoring energy of the cell boundaries is

important for clarifying the cause of response degradation in proposed *RMM-Pi-cell*. Previous research has exposed the anchoring energy measurement, such as electrical field method [75-76]. However, these methods were proposed for general homogeneous or vertical alignment cells, not for asymmetric Pi-cells. To find a method for asymmetric Pi-cell and improve the measuring accuracy are essential. In the future, the anchoring effect of a *RMM-Pi-cell* should be studied in detail to find out the solution for the response time degradation.

6.2.2 Fabrication Conditions Optimization of RM Films

Based on aforementioned inference, the anchoring effect may be the key factor which results in the increase of response time. In addition to the anchoring energy investigation of a RMM-Pi-cell, the fabrication optimization of RM films also affects the interaction between LCs and RM film. Moreover, the RM film is very thin and easy to be broken during fabrication. It is necessary to find the optimized formula of RM and solvent for improving the coating uniformity and ductility. Simultaneously, the UV dose of RM films also need to be concerned for the anchoring force with LCs.

Besides, we hope that the pretilt angles of the RM films can be controlled by process conditions. The optimized pretilt angle should be controlled just higher than critical pretilt angle to prevent the transmittance degradation. The RM film's quality evaluation is suggested by using the anchoring energy of the cell to be the index factor. Accordingly, we can further illustrate the response mechanism and prevent the degradation of response time in *RMM-Pi-cell*.

6.2.3 Manufacturing Implementation of *RMM-Pi-cell* into a real LCD

Since the *RMM-Pi-cell* needs RM film treatment after PI printing process, the standard fabrication process of the LC cell has to add extra coating and baking steps. The inject-printing method is suggested to build in the available process for RM film coating, shown as Fig. 6-5.

Reactive monomer (RM) solution should be prepared in advance. The RM solution can be coated on PI buffed substrates by the ink-jet printing method; RM film can be also deposited by a spin coater. Since the RM film is very thin and broken easily, the RM treated substrates should be exposed under the UV light with a simultaneous baking process. In other words, the reactive monomers are reacted by UV light as the solvent is evaporated in RM film to prevent the fast shrinking and breaking of RM films. Then, the following processes are the same with standard LC cell fabrications. With the extra steps, the *RMM-Pi-cell* can be adopted into mass-production line.
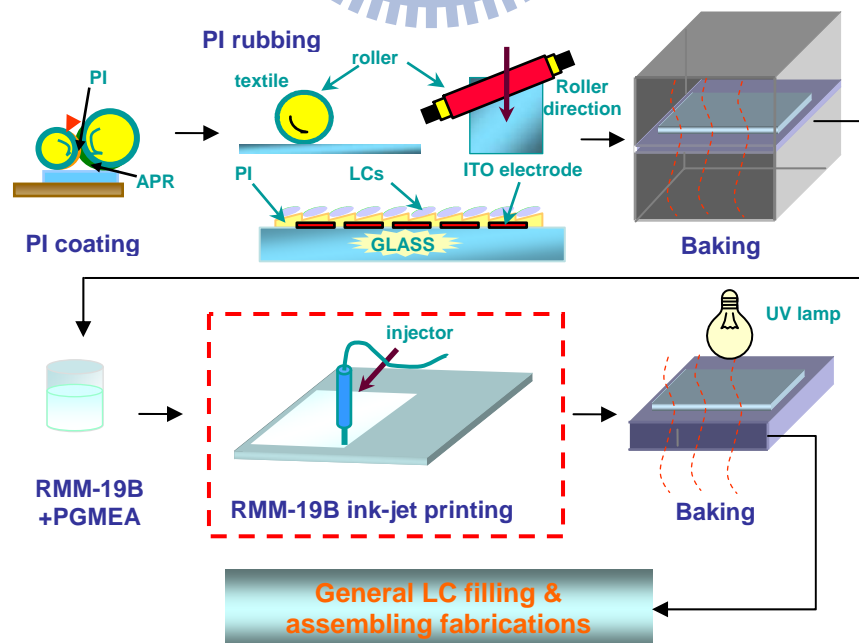
Fig.6-5 Manufacturing Implementation of RMM-Pi-cell into an actual LCD.

6.2.4 Summary

People not only pursue multimedia entertainments, but also concern power saving of these multimedia devices. Therefore, how to increase optical throughput of display device is an essential subject in advanced TFT-LCD technologies. Among the technologies, the FSC-LCD is a potential candidate with high optical throughput. However, the sequential colored FSC-LCD still needs a fast response LCD for resolving the color-breakup issue. We studied the fast response LC-cell for improving motion blur issue in conventional TFT-LCD TVs and realizing the non-CBU FSC-LCD. Even blue phase may be a better choice in fast response time and easy fabrication; many efforts are needed on material developments for resolving narrow temperature range and high driving voltage issues compared with commercialized LC modes. Our future works are focused on the *RMM-Pi-cell*, because the novel transition *RMM-Pi-cell* with strong potential for resolving the motion blur issue and realizing Eco display — FSC-LCDs. Although the *RMM-Pi-cell* has remaining issues, a transition-free, high contrast ratio, high transmittance and fast response *RMM-Pi-cell* can still be expected to apply for advanced TFT-LCDs.

Reference

[1] LCD Optics 101, Retrieved August 28, 2008, from the :
http://solutions.3m.com/wps/portal/3M/en_US/Vikuiti1/BrandProducts/secondary
/optics101

[2] Norio Koma, Tetsuya Miyashita,Tatsuo Uchida, and Nobuhiro Mitani, "Color Field Sequential LCD Using an OCB-TFT-LCD," *in Proceedings of SID Symposium Digest*, pp. 632-635 (2000).

[3] Szu-Fen F. Chen, Chien-Lin Pan, Shen-Jiang Jeng, Chih-Liang Wu, and Peter Hsu, "Improving the Motion-Image Quality of LCD TVs," *Novel Display Technology Issue of Information Display*, **22**, pp. 2-6 (2006).

[4] R. S. West, "High Brightness Direct LED Backlight for LCD-TV," *in Proceedings of SID Symposium Digest* **34**, pp. 1262-1265 (2003).

[5] S. Sakai, "A Thin LED Backlight System with High Efficiency for Backlighting 22- in. TFT-LCDs," *in Proceedings of SID Symposium Digest* **35**, pp. 1218-1221 (2004).

[6] Lumileds Lighting, "Luxeon Emitter Technical Data DS25 (02/13/04)".

[7] H. Seetzen, W. Heidrich, W. Stuerzlinger, G. Ward, L. Whitehead M. Trentacoste, A. Ghosh, and A. Vorozcovs, "High Dynamic Range Display Systems," *SIGGRAPH 2004, ACM Transactions on Graphics* **23** (3), pp. 760-768 (2004).

[8] T. Shirai, S. Shimizukawa, T. Shiga, S. Mikoshiba, and K. Käläntär, "RGB-LED Backlights for LCD-TVs with 0D, 1D, and 2D Adaptive Dimming," *in Proceedings of SID Symposium Digest* **37**, pp. 1520-1523 (2006).

[9] C.-H. Lin, "Extraordinarily wide-view and high-transmittance vertically aligned liquid crystal displays," *Appl. Phys. Letters* **90**, 151112 (2007).

[10] S. Tahata, A. Tsumura, M. Mizunuma, A. Tamatani, Y. Morii, M. Fujii, and F.Matsukawa, "Wide-viewing-angle LCD controlled by a lateral electric field," *Proc. SPIE* **3015**, pp. 134-140 (1997).

[11] T. Ishinabe, T. Miyashita, and T. Uchida, "Optical design of R-OCB mode full-color reflective LCD with wide viewing angle and high contrast," *J. Soc. Inf. Display* **6**, pp. 243-246 (1998).

[12] Tien-Chu P. Hsu, Jung-Chieh L. Cheng, Ming-Tan T. Hsu, Szu-Fen F. Chen, " High Video Image Quality Technology: Dynamic Scanning Backlight with Black Insertion (DSBBI) implemented in a 32" OCB-LCD TV," *in Proceedings of SID Symposium Digest*, pp. 353 -355 (2007)

[13] Fion Sze-Yan Yeung and Hoi-Sing Kwok, "Fast-response no-bias-bend liquid crystal displays using nanostructured surfaces," *App. Phys. Letters*, **88**, 063505 (2006).

[14] Y. ITO, R. Matsubara, R. Nakamura, M. Nagai, S. Nakamura, H. Mori, and K. Mihayashi, "OCB-WV film for fast- response-time and wide-viewing-angle LCD-TVs,"*in Proceedings of SID Symposium Digest*, pp. 986-989 (2005).

[15] C. W. Oseen, "The theory of liquid crystals," *Trans. Faraday Soc.* **29**, pp. 883-899 (1933).

[16] F. C. Frank, "Liquid crystals. On the theory of liquid crystals," *Discuss. Faraday Soc.* **25**, pp. 19-28 (1958).

[17] H. C. Tseng, Dayton L. Silver, and Bruce A. Finlayson, "Application of the Continuum Theory to Nematic Liquid Crystals," *Phys. Fluids* **15**, pp. 1213-1222 (1972).

[18] D. W. Berreman, "Elastic continuum theory cutoffs and order in nematics and solids," *J. Chem. Phys*. **62**, pp. 776-778 (1975).

[19] E. Lueder, "Liquid Crystal Displays", published by Wiley LTD (2001).

[20] Pochi Yeh and Claire Gu, "Optics of Liquid Crystal Displays", published by Wiley LTD (1999).

[21] A. Muravsky, A. Murauski, V. Mazaeva, and V. Belyaev, "Parameters on the LC alignment of organosilicon compound films," *J. Soc. Infor. Display* **13**, pp. 349-356 (2005).

[22] H. Gruler and L. Cheung, "Dielectric alignment in an electrically conducting nematic liquid crystal," *J. Appl. Phys.* **46**, pp. 5097-5100 (1975).

[23] J. Nehring, A. R. Kmetz, and T. J. Scheffer, "Analysis of weak-boundary-coupling effects in liquid-crystal display," *J. Appl. Phys.* **47**, pp. 850-857 (1976).

[24] N. Nagae, T. Miyashita, "T. Uchida, A novel method for high speed transition from splay to bend alignment in the OCB-mode LCD with fast response," *in*

Proceedings of SID Symposium Digest **31**, 26-29 (2000).

[25] X. D. Mi, M. Xu, D.-K. Yang, and P. J. Bos, "Effects of Pretilt Angle on Electro-Optical Properties of π-Cell LCDs," *in Proceedings of SID Symposium Digest* **30**, pp. 24-27 (1999).

[26] H. Kikuchi, H. Yamamoto, H. Sato, M. Kawakita, K. Takizawa, and H.Fujikake, "Bend-Mode Liquid Crystal Cells Stabilized by Aligned Polymer Walls," *Jpn. J. Appl. Phys.* **44**, pp. 981-989 (2005).

[27] T. Uchida and T. Ishinabe, "Progress in viewing-angle properties of liquid-crystal displays," *J. Soc. Inf. Display* **12**, pp. 309-313 (2004).

[28] T. Ishinabe, T. Miyashita, and T. Uchida, "Novel Wide Viewing Angle Polarizer with High Achromaticity," *in Proceedings of SID Symposium Digest 31*, pp.1094-1097 (2000).

[29] P. van de Witte, S. Stallinga and J. A. M. M. van Haaren, "Viewing Angle Compensators for Liquid Crystal Displays based on Layers with a Positive Birefringence," *Jpn. J. Appl. Phys.* **39**, pp. 101-108 (2000).

[30] T. Ishinabe, T. Miyashita, and T. Uchida, "Optical Design of R-OCB Mode Full-Color Reflective LCD with Wide Viewing Angle and High Contrast," *in Proceedings of SID Symposium Digest* **29**, pp. 774 (1998).

[31] P. J. Bos, and K. R. Koehler/Beran, "The Pi-cell: A Fast Liquid-Crystal Optical Switching Device," *Mol. Cryst. Liq. Cryst.* **113**, pp. 329-339 (1984).

[32] H. Mori, and P. J. Bos, "Design Concepts of the Discotic Negative Birefringence Compensation films," *in Proceedings of SID Symposium Digest*, pp. 830-833 (1998).

[33] H. G. Walton, and M. J. Towler, "On the response speed of pi-cells," *Liq. Cryst.* **27**, pp. 1329-1335 (2000).

[34] S. T. Wu, and A. M. Lackner, "Mylar-film-compensated πand parallel-aligned liquid crystal cells for direct-view and projection displays," *Appl. Phys. Letters* **64**, pp. 2047-2049 (1994).

[35] J. E. Anderson, C. Chen, and A. Lien, U.S. Patent No. 6,067,142, May. 23, 2000.

[36] Y. Yamaguchi, T. Miyashita, and T. Uchida, "Wide-Viewing-Angle Display Mode for the Active-Matrix LCD Using Bend-Alignment Liquid-Crystal Cell," *in Proceedings of SID Symposium Digest*, pp. 277-280 (1993).

[37] E. J. Acosta, M. J. Towler, and H. G. Walton, "The role of surface tilt in the operation of pi-cell liquid crystal device," *Liq. Cryst.* **27**, pp. 977-984 (2000).

[38] P. D. Brimicombe, and E. P. Raynes, "The influence of flow on symmetric and asymmetric splay state relaxations," *Liq. Cryst*. **32**, pp. 1273-1283 (2005).

[39] P. D. Brimicombe, and E. P. Raynes, "Symmetric *H* state lifetime in splayed nematic liquid crystal devices," *Appl. Phys. Letters* **89**, 031121 (2006).

[40] E. J. Acosta, M. J. Towler, and M. D. Tillin, "Route towards optimization of the response times of a pi-cell liquid-crystal mode," *J. Appl. Phys.* **97**, 093106 (2005).

[41] Chia-Tien Lee, Szu-Fen Chen, and Huang-Ming Philip Chen,"Nanostructure Structure Effect on Transition in Pi-cells," *IDMC'07*, pp.78-80 (2007).

[42] F. F. Abraham, "Homogeneous nucleation theory", Academic Press, NY (1974).

[43] Frank S. Ham, "Diffusion-Limited Growth of Precipitate Particles," *J. Appl. Phys.* **30**, pp. 1518-1525 (1959).

[44] Nucleation-Wikipedia, from the http://en.wikipedia.org/wiki/Nucleation.

[45] G. D. Lee, J. W. Lee, K. H. Park and J. C. Kim *et al*., "Defects Nucleation and Dynamical Behavior from Surface Inhomogeneity," *Mol. Cryst. Liq. Cryst.* **433**, pp. 199–206 (2005).

[46] Schmelzer, J (Ed.), Fokin, Yuritsyn, Zanotto. Nucleation Theory and Applications. Nucleation and Crystallization Kinetics in Silicate Glasses: Theory and Experiment. pp. 76-83, published by Wiley-VCH Verlag GmbH & Co. (2005).

[47] Prof. Y. P. Huang's lecture note in Display Institute, National Chiao Tung University, Taiwan.

[48] M. E. Becker, **"**Measurement of tilt-bias angle: performance evaluation of the crystal rotation method ," *J. Soc. Inf. Display* **5**, pp. 283-287 (1997).

[49] M. E. Becker, "LCD visual performance: characterization and evaluation," *Proc. SPIE* **3636**, pp. 170-183 (1999).

[50] M. E. Becker, J. Laur, and J. Neumeier, "Electro-optical Characterization of Reflective LCDs ," *in Proceedings of SID Symposium Digest* **32**, pp. 322-325 (2001).

[51] H. Woehler and M. E. Becker, "Numerical modeling of LCD electro-optical performance," *Proc. SPIE* **4759**, pp. 359-367 (2002).

[52] F. Bruyneel, H. D. Smet, J. Vanfleteren, and A. V. Calster, "Method for measuring the cell gap in liquid-crystal displays ," *Opt. Eng.*, **40**, p. 259 (2001).

[53] C. L. Kuo, T. Miyashita, M. Suzuki, and T. Uchida, "Crucial influences of K_{33}/K_{11} ratio on viewing angle of display mode using a bend-alignment liquid-crystal cell with a compensator," *Appl. Phys. Letters* **68**, pp.1461-1463 (1996).

[54] T. Uchida, Y. Kimura, S. Kuniaki, H. Nakamura and Y. Taira, patent JP 9 185 037, 1995.

[55] C. Lee, H. Chang, J. Lyu, K. Kim, and J. Souk, **"**High Performance 17.0" SVGA OCB Panel with Fast Initial Bend Transition," *in Proceedings of SID Symposium Digest*, pp. 570-573 (2002).

[56] S.H. Lee, S.H. Homg, J.D. Noh, H.Y. Kim, and D.S. Seo, "Chiral-Doped Optically Compensated Bend Nematic Liquid Crystal Cell with Continuous Deformation from Twist to Twisted Bend State," *Jpn. J. Appl. Phys.* **40**, pp. L389-L392 (2001).

[57] I. Inoue, T. Miyashita, T. Uchida, Y. Yamada, and Y. Ishii, "A new solution for splay-to-bend transition in OCB mode with a twisted area," *J. Soc. Inf. Display* **11**, pp. 571-576 (2003).

[58] T. Satake, and T. Kurata, "A Novel Fast-Switching LCD with Dual-Domain Bend Mode ,"*Asia Display Digest,* 12-6 (2004).

[59] H. Nakamura, and M. Noguchi, "Bend Transition in Pi-cell," *Jpn. J. Appl. Phys.* **39**, pp. 6368-6375 (2000).

[60] Y. Zhang, B. Wang, D. B. Chung, J. Colegrove and P. J. Bos, **"**Two-Dimensional Dynamic Modeling of Splay to Bend Transition in Pi Cell or BTN Device at High Voltage," *in Proceedings of SID Symposium Digest*, pp. 1782-1785 (2005).

[61] N. Koma, T. Miyashita, K. Yoneda, and T. Uchida, **"**Using an OCB-Mode TFT-LCD for High-speed Transition from Splay to Bend Alignment," *in Proceedings of SID Symposium Digest*, pp. 28-31 (1999).

[62] M. D. Tillin, E. P. Raynes, and M. J. Towler, US Patent, US 6222605, 2001.

[63] S. H. Lee, T. J. Kim, G.D. Lee, T.H. Yoon, J.C. Kim, "Geometric Structure for

the Uniform Splay-to-Bend Transition in a π-Cell," *Jpn. J. Appl. Phys.* **42**, pp. L1148-L1151 (2001).

[64] E. Acosta, B. Henley, D. Kean, M. Tillin, C. Tombling, M. Towler, E. Walton, H. Walton and R. Winlow, *"*Nucleation of the pi-cell operating state: a comparison of techniques," *Liq. Cryst.* **31**, pp.1619-1625 (2004).

[65] Szu-Fen F. Chen, Yu-Yun Chang, Huang-Ming P. Chen, and Han-Ping D. Hsieh, "A Novel Nanostructure Enhanced Pi-cell for Transition Rate Improvement," *in Proceedings of SID Symposium Digest* (2010)-Accept.

[66] K. Nakao, D. Suzuki, T. Kojima, M. Tsukane, and H. Wakemoto, "High-Speed Bend Transition Method using Electrical Twist Field in OCB Mode TFT-LCDs," *in Proceedings of SID Symposium Digest* **35**, 1416-1419 (2004).

[67] S. H. Kim and L. C. Chien, "Electro-Optical Characteristics and Morphology of a Bend Nematic Liquid Crystal Device Having Templated Polymer Fibrils," *Jpn. J. Appl. Phys.* **43**, 7643-7647 (2004).

[68] B.-R. Yang, S. J. Elston, P. Raynes, and H.-P. D. Shieh, "High-Brightness relaxed-bend state in a pi cell stabilized by synchronized polymerization," *Appl. Phys. Letters* **92**, 221109 (2008).

[69] Szu-Fen F. Chen, Huang-Ming P. Chen, Liansing Chow, Yu-Yun Chang, and Han-Ping D. Shieh, "Splay-to-Bend Transition-Free Reactive Monomer Modified Pi-Cell," *IEEE Photonics Technology Letters*, Vol. 21, No. 10, MAY 15, pp. 636-638 (2009).

[70] Szu-Fen F. Chen, Yu-yun Chang, Liansing Culp Chow, Huang-Ming Philip Chen, and Han-Ping D. Shieh, "Transition-free, High Contrast Reactive Monomer Modified Pi-Cell," *in Proceedings of SID Symposium Digest*, pp.1592-1594 (2009).

[71] X. J. Yu and H. S. Kwok, "Bistable bend-splay liquid crystal display," *Appl. Phys. Letters* **85**, 3711 (2004).

[72] Y. Sun, H. Ma, Z. Li and Z. Zhang, "Pretilt angle effects on critical voltage and dynamic response of pi cell," *Appl. Phys. Letters* **90**, 091103 (2007).

[73] C.-H. Chiu, H.-L. Kuo, P.-C. Chen, C.-H. Wen, Y.-C. Liu, and H. M. P. Chen, "Nanoimprinting-lithography-induced self-aligned liquid crystals for novel multifunctional optical films," *Appl. Phys. Letters* **88**, 073509 (2006).

[74] H. Kikuchi, M. Yokota, Y. Hisakado, H. Yang and T. Kajyama, "Polymer

-stabilized liquid crystal blue phases," *Nature Materials* **1**, pp.64-68 (2002).

[75] Anatoli Murauski, Vladimir Chigrinov, Alexander Muravsky, Fion Sze-Yan Yeung, Jacob Ho, and Hoi-Sing Kwok, "Determination of liquid-crystal polar anchoring energy by electrical measurements," *Physical Review E* **71**, 061707 (2005).

[76] Xiangyi Nie, Yi-Hsin Lin, Thomas X. Wu, Haiying Wang, Zhibing Ge, and Shin-Tson Wu, "Polar anchoring energy measurement of vertically aligned liquid-crystal cells," *J. Appl. Phys.* **98**, 013516 (2005).

Appendix A

Nano-particle's Distribution in Different Concentrations

The following photographs show the distribution of different diameter nano-particles in different concentrations. The treatment method is method 2 proposed for high density distribution without aggregation.
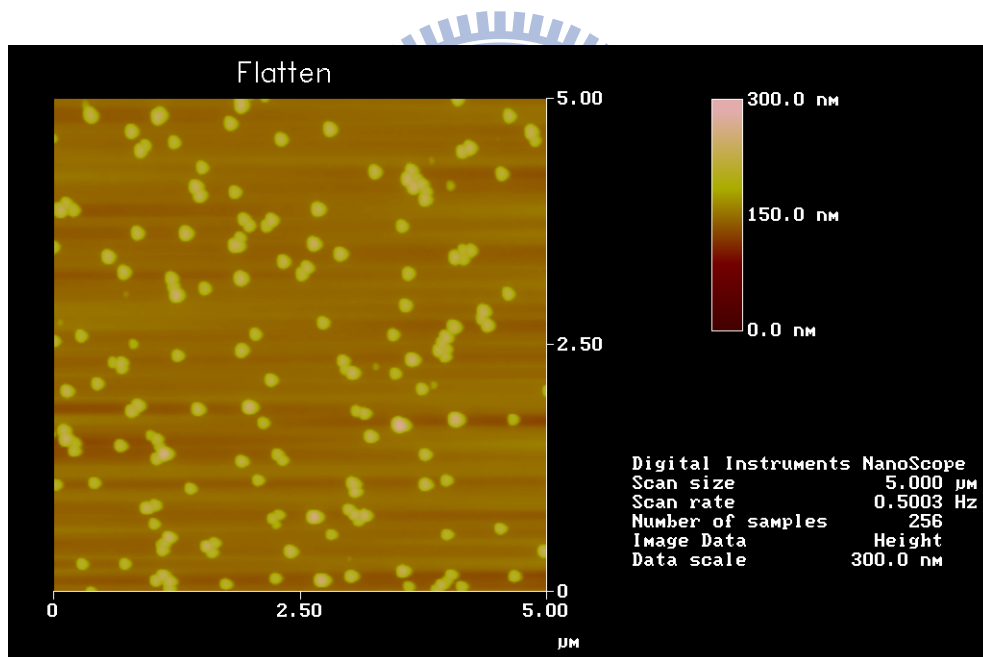

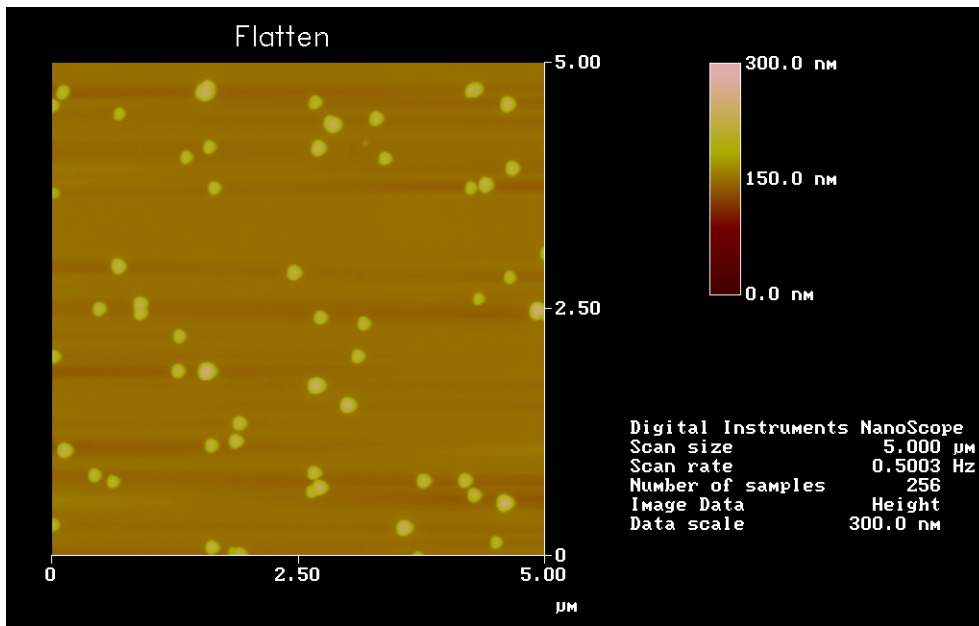*Fig. A-1 0.1wt% 90nm nano-particles distribution.*

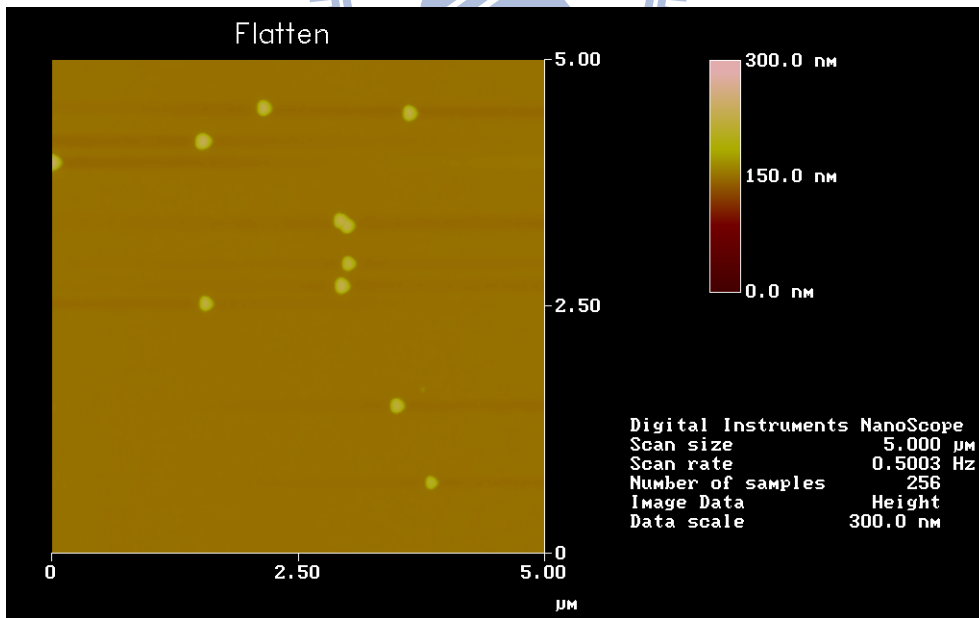*Fig. A-2 0.05wt% 90nm nano-particles distribution.*

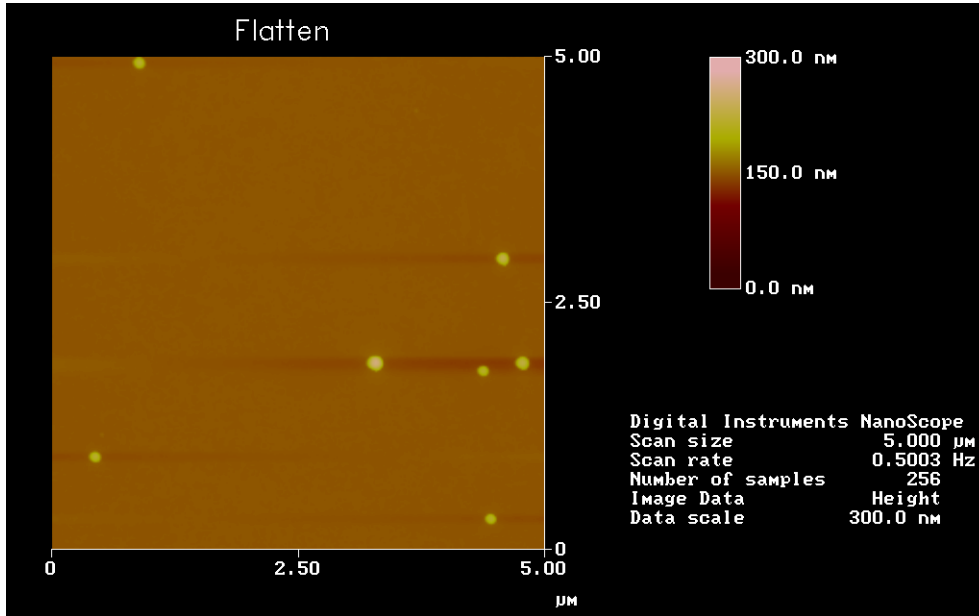*Fig. A-3 0.0125wt% 90nm nano-particles distribution.*

Fig. A-4 0.004wt% 90nm nano-particles distribution.
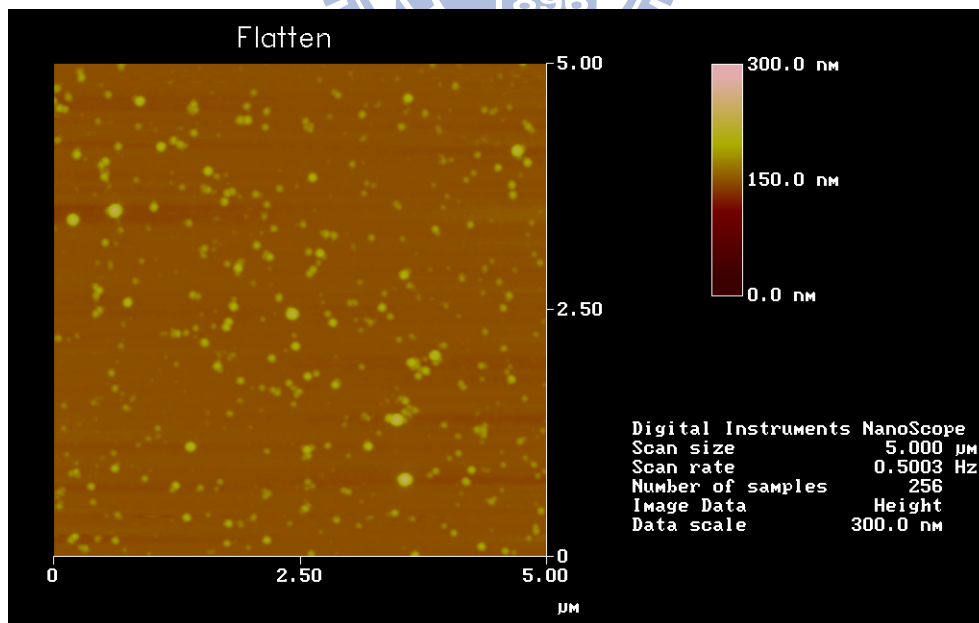

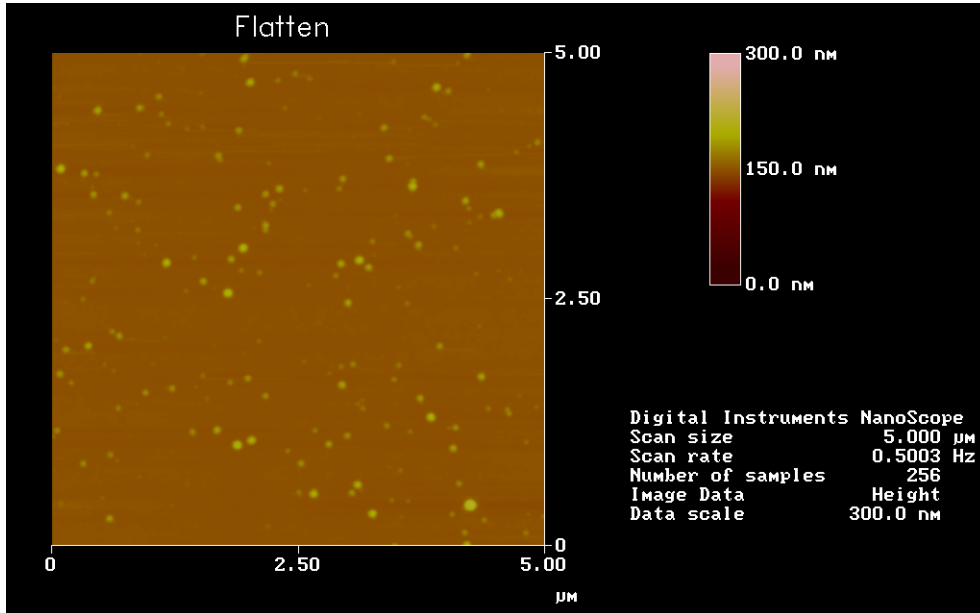*Fig. A-5 0.1wt% 50nm nano-particles distribution.*

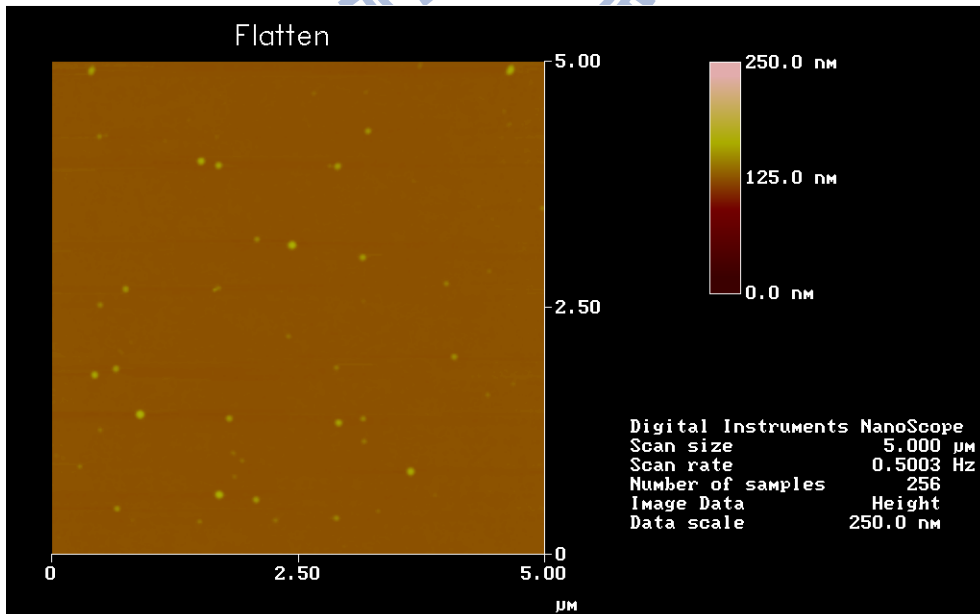*Fig. A-6 0.05wt% 50nm nano-particles distribution.*

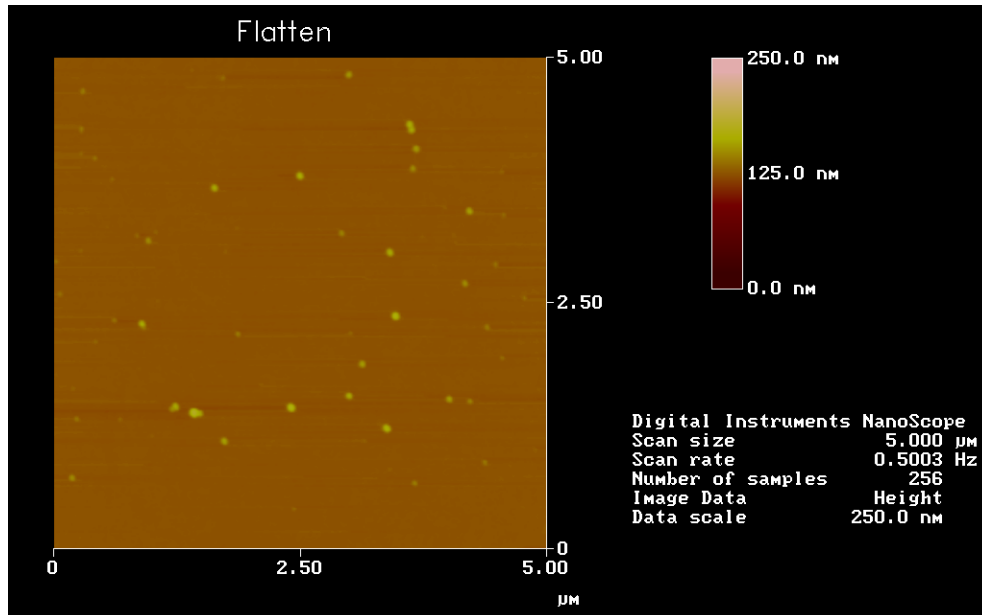*Fig. A-7 0.0125wt% 50nm nano-particles distribution.*

Fig. A-8 0.004wt% 50nm nano-particles distribution.

Appendix B

LC Data Sheet: ZCE-5096XX

(Ref.: Data sheet from Chisso Co.)

Sample (Properties)		UNIT	ZCE-5096XX
$T_{N\to C(S)}$		$^\circ$C	< -20
$T_{N\to I}$			95.5
Viscosity (at 20°C)	η	mPa.s	46.7
	$\gamma1$	mPa.s	178.0
Optical anisotropy (at 25°C 589nm)	Δn		**0.158**
	n_e		1.662
	n_o		1.504
Dielectric anisotropy (at 25°C 1KHz)	$\Delta\varepsilon$		**10.0**
	$\varepsilon_{//}$		14.1
	$\varepsilon_\perp$		4.1
Specific anisotropy (at 25°C)	ρ	Ω.cm	> 5 ×10^{14}
Cell gap	d	μm	5.2
Twist angle	degree	$^\circ$(deg)	80
Threshold Voltage	$V_{10,0,25}$	V	1.53
	$V_{50,0,25}$		1.75
Saturation Voltage	$V_{90,0,25}$		2.13
K11 (at 20°C)		pN	9.8
K22 (at 20°C)		pN	5.8
K33 (at 20°C)		pN	11.8
Density (at 20°C)			1.1410
Density (at 25°C)			1.1371

Appendix C

Polymerisable Nematic Mixture RMM19B

(Ref.: Instructions for use from Merck KGaA, Darmsdate, Germany)

Instructions for Use   MERCK

Polymerisable Nematic Mixture RMM19B

Introduction

RMM19B is a nematic acrylate mixture that can be polymerised by exposure to UV radiation to produce an aligned polymer film. The mixture is designed to give splayed alignment when coated onto a suitable substrate, and is therefore ideal for preparing optical retardation layers. Typically, films of <2 micron (dry thickness) are required – this is most conveniently achieved by coating the material dissolved in a solvent. RMM19B contains a photoinitiator, and is intended to be polymerised by UV radiation.

Storage

Store the bottles at room temperature in a dark place with the top screwed on. Do not backfill the bottles with inert gas.

**Preparation of aligned films by solvent coating**

1. RMM19B is supplied as a non-homogeneous mixture of components. Homogeneity is best achieved by addition of the required amount of solvent to the bottle. RMM19B is soluble in toluene, xylene, or 1,2-propanediol monomethyl ether acetate (PGMEA) or alternatively a blend of solvents including such as butanone, isopropyl alcohol or cyclohexanone can also be used to aid wetting or control solvent evaporation. The choice of solvent will depend on the method of application. The concentration of solids in the solution should typically be in the order of 20-30%, depending on the desired coating thickness.

2. Weigh the required amount of solvent into the bottle. Solution may be achieved by agitation, however, gentle heating on a water bath at 40°C may be helpful. Filter the solution before use through a 0.2μm PTFE membrane filter. The use of plastic syringes must be avoided.

3. The coating substrate (e.g. glass or plastic) should have an appropriate liquid crystal aligning layer on the surface (e.g. rubbed polyimide) in order to obtain the correct alignment of the reactive liquid crystal film before polymerisation.

4. Coat the solution on to the substrate by a suitable coating technique, such as spin-coating or with a wire-wound bar, in a clean area. Allow the solvent to evaporate at ambient temperature to leave a reactive liquid crystal film of the desired thickness.

5. All of the above operations involving solvent should be carried out in a suitably ventilated area.

Polymerisation

RMM19B is designed to be polymerised in the presence of oxygen, using a suitable UV lamp, e.g. a medium or high pressure mercury lamp.

Example

0.3g RMM19B was dissolved in 0.7g toluene to give a 30% /w solution, which was filtered through a 0.2 μm PTFE membrane filter. The solution was bar-coated on to a rubbed, TAC film substrate to produce a 4μm (wet thickness) film. The coated film was dried at room temperature for 60s and subsequently polymerised (20mWcm^{-2} UV-A radiation, 60s). The polymerised film exhibited good splayed (O-plate) alignment and had the following retardation profile.
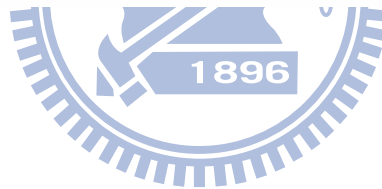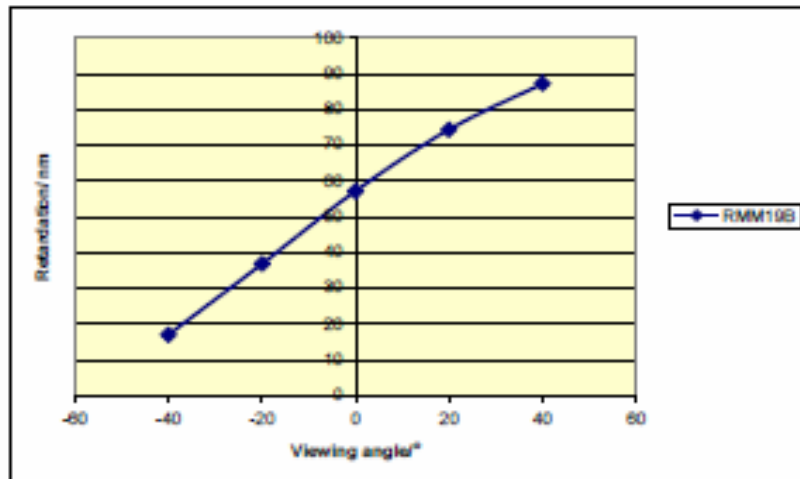
Publication List

Journal Papers

1. **Szu-Fen Chen**, Chao-Heng Huang, Jhih-Ping Lu, Meng-Xi Chan; and Han-Ping D. Shieh, "IER film and inkjet printing method for full-color transflective cholesteric LCD," *IEEE/OSA Journal of Display Technology*, Vol.1 Issue 2, pp.225-229 (2005).

2. **Szu-Fen F. Chen**, Wei-Chung W. Cheng, and Han-Ping D. Shieh, "CSD: A New Unified Threshold Metric of Evaluating LCD Viewing Angle by Color Saturation Degradation," *IEEE/OSA Journal of Display Technology*, Vol.2, Issue.2, pp. 106 (2006).

3. **Szu-Fen F. Chen**, Huang-Ming P. Chen, Liansing Chow, Yu-Yun Chang, and Han-Ping D. Shieh, "Splay-to-Bend Transition-Free Reactive Monomer Modified Pi-Cell," *IEEE Photonics Technology Letters*, Vol. 21, No. 10, MAY 15, pp.636-638 (2009).

Conference Papers

1. **Szu-Fen F. Chen**, Shih-Tsung Yang, "The Implementation of Product Lifecycle Management (PLM) System", *IDMC'05*, pp.650-652 (2005).

2. **Szu-Fen F. Chen,** Wayne Cheng, Han-Ping D. Shieh, "Evaluate LCD viewing angle by color saturation degradation," *LEOS'05, The 18th Annual Meeting of the IEEE*, pp. 519 – 520 (2005).

3. Tien-Chu P. Hsu, Jung-Chieh L. Cheng, Ming-Tan T. Hsu, **Szu-Fen F. Chen**, " High Video Image Quality Technology: Dynamic Scanning Backlight with Black Insertion (DSBBI) implemented in a 32" OCB-LCD TV," *SID'07 Digest*, pp. 353 -355 (2007).

4. Tien-Chu Hsu, Chien-Lin Pan, Chih-Liang Wu, Jung-Chieh Cheng,Ming-Tan Hsu and **Szu-Fen Chen**,"A 32-in. High Video Image Quality OCB (Optical Compensation Bend) LCD TV," *IDW'07*, pp.25-27 (2007).

5. Chia-Tien Lee, **Szu-Fen Chen**, and Huang-Ming Philip Chen,"Nanostructure Structure Effect on Transition in Pi-cells," *IDMC'07*, pp.78-80 (2007).

6. Wei-Ching Wu, Yi-Fan Chen, **Szu-Fen Chen,** and Huang-Ming Philip Chen, "Critical Voltage Reduction by Alignment Layer Modification in Pi-Cells," *IDMC'07*, pp.692-694 (2007).

7. **Szu-Fen F. Chen**, Yu-yun Chang, Liansing Culp Chow, Huang-Ming Philip Chen, and Han-Ping D. Shieh, "Transition-free, High Contrast Reactive Monomer Modified Pi-Cell," *SID'09 Digest*, pp.1592-1594 (2009).

8. **Szu-Fen F. Chen**, Yu-Yun Chang, Huang-Ming P. Chen, and Han-Ping D. Hsieh, "A Novel Nanostructure Enhanced Pi-cell for Transition Rate Improvement," *SID'10 Digest* (2010)-Accept.

Patents

1. 徐名潭、鄭戎傑、徐天助、<u>陳司芬</u>, 顯示器之驅動裝置與其驅動方法--Driving Apparatus and Method thereof for Display (5/31/2007 提出申請，文件申請案號:96119572)

2. 簡耀�、王智杰、<u>陳司芬</u>、鄭戎傑、陳麗珊, OCB 提升穿透率驅動電路設計--Transmittance improvement of OCB mode TFT-LCDs by driving circuit (申請號：96116272，申請日：5/8/2007)

3. 簡耀section、王智杰、<u>陳司芬</u>、鄭戎傑,電容耦合插黑技術--The method of black image insertion (申請號：96114215，申請日：4/23/2007)

4. <u>陳司芬</u>,陳皇銘,吳威慶,謝漢萍, 新型無轉態 OCB-Mode 液晶顯示器--A Novel No-bias Optically Compensated Bend (OCB) Mode Liquid Crystal Display(台灣案申請號 97100340, 美國案申請號 12168,072

Others

1. **Szu-Fen F. Chen** et al., "Improving the Motion-Image Quality of LCD TVs", *Novel Display Technology Issue of Information Display*, **22**, pp. 20, (2006).

Award

1. 2006 平面顯示器元件產品技術獎-傑出產品獎， "1 ms 32" OCB TV", 經濟部工業局影像顯示辦公室主辦.

Vita

Name: Szu-Fen F. Chen 陳司芬

Day of birth: January 20, 1969

Address: 桃園縣楊梅鎮裕成路 166 之 1 號

E-mail: fenychen@so-net.net.tw

Education:

2004 – Present : Ph. D. in Institute of Electro-Optical Engineering.
National Chiao Tung University, Hsinchu, Taiwan.

1992 – 1994 : MS in Institute of Electro-Optical Engineering.
National Chiao Tung University, Hsinchu, Taiwan.

1988 – 1992 : BS in Department of Physics.
National Cheng Kung University, Tainan, Taiwan.

Experience:

2007/04 – Present: Senior Manager, Panel Technology Div., Product Design General Dept., Small & Medium TFT Product BU, Chung-Hwa Picture Tube, LTD.

2004/04 – 2007/04: Director, New Panel Technology Dept. TFT Product BU, Chung-Hwa Picture Tube, LTD.

1995/04 – 2004/04: Engineer/ Manager, TFT Product BU, Chung-Hwa Picture Tube, LTD.

1994/06 – 1995/04: Engineer, Hsinchu Factory, Philips Taiwan.